2016 | Faculty of Engineering Technology

DOCTORAL DISSERTATION

Upscaling of Organic Light Emitting Devices: a focus on innovative materials, versatile printing techniques and state-of-the-art post-treatments

Doctoral dissertation submitted to obtain the degree of
Doctor of Engineering Technology, to be defended by

Koen Gilissen

Promoter: Prof. Dr Ir Wim Deferme
Co-promoter: Prof. Dr Jean Manca

D/2016/2451/15

IMO - IMOMEC
INSTITUUT VOOR MATERIAALONDERZOEK

Chairman	Prof. Dr Marc D'Olieslaeger Dean Faculty of Engineering Science *UHasselt, Belgium*
Promotor	Prof. Dr Ir W. Deferme *UHasselt, Belgium*
Copromotor	Prof. Dr J.V. Manca *UHasselt, Belgium*
Members of the jury	Prof. Dr W. De Ceuninck *UHasselt, Belgium*
	Prof. Dr Milos Nesladek *UHasselt, Belgium*
	Prof. Dr Ir Michael Daenen *UHasselt, Belgium*
	Prof. Dr Youri Meuret *KULeuven, Belgium*
	Prof. Dr Stefan C.J. Meskers *TU Eindhoven, Netherlands*

Acknowledgements

A lot of people should be acknowledged and thanked for the help and support with the work I present in my thesis. One thing is for certain; I could not have accomplished this without them.

While breaking the PhD thesis acknowledgement section convention, I would first like to thank my mother, who passed away very recently. It is sad you couldn't be here; you were and would have been so proud, thanks for all the support in so many ways.

Off course, nothing of this would have been possible without my promotor and co-promotor, Wim and Jean, the perfect duo ever so positive and resourceful. Although their roles switched during they both deserve equal and allot of my gratitude. Thank you for creating a positive and inspiring work atmosphere and for always being stand-by with new ideas and insights.

I also want to thank my colleagues in the lab who trained, helped or assisted me in my daily experimental work. Like Jeroen Stryckers who among many other things carried out the spray coating experiments together with me. We also made some interesting road trips, together with Tim Vangerven, to the campus of the TU/Eindhoven, which are at the least to be called memorable. Or Tim Vangerven, Ilaria Cardinaletti, Bert Conings and Jurgen Kesters who where always willing to help or have a discussion on daily experiments and results. I would also like to thank Michaël Daenen for his seemingly inexhaustible enthusiasm for solving or looking at problems big or small. And off course I would like to thank my fellow EMAP PhD students: Thijs Vandenryt, Jeroen Stryckers, Tim Cluckers, Glen Vandevenne, Inge Verboven and Steven Nagels for perfectly timed intermezzo's, break and so called meetings. I would also like to thank Jeroen Drijkoningen for his numerous AFM measurements and the many discussions about technology.

I would also like to thank Pieter Robaeys for the effortless collaboration on the BNCD:Au-grid electrodes. Furthermore I would like to thank the IMO chemistry department, Pieter Verstappen and Wouter Maes for help with and performing of the chemical analysis needed to support my result and for proof reading and contribution to publications.

Our laboratory would be a dangerous, chaotic and dysfunctional mess if it was not for our team of technicians, Hilde, Christel, Johnny, Jan, Lieven and Eric. Thank you for watching over our safety, designing, maintaining and repairing our equipment and measurement setups.

I would like to thank my family for the endless support. Karolien thanks for being there supporting me, giving advice and your ability to put things in perspective. I want to thank my son, Stan, for sleeping full nights from 20:00u until 8:00u and thus preventing a severe case of sleep deprivation.

Table of contents

List of publications and presentations

Journal Articles

K. Gilissen, J. Stryckers, W. Moons, J.V. Manca, W. Deferme, "Microwave Annealing, a Promising Step in The Roll-To-Roll Processing of Organic Electronics", FACTA UNIVERSITATIS Series: Electronics and Energetics, 28, 1, 143 - 151, 2014

K. Gilissen, J. Stryckers, P. Verstappen, J. Drijkoningen, G.H.L. Heintges, L. Lutsen, J.V. Manca, W. Maes, W. Deferme, "Ultrasonic spray coating as deposition technique for the light-emitting layer in polymer LEDs", Organic Electronics, 20, P31–35, 2015, doi:10.1016/j.orgel.2015.01.015

P. Robaeys and K. Gilissen, M. McDonnald, E. Bourgeois, J. D'Haen, Z. Remes, K. Haenen, J.V. Manca, W. Deferme and M. Nesladek, "Build-in metal grid structures in BNCD as transparent electrodes for organic electronic applications", Nature Communication, *in preparation.*

M. Van Gompel, B. Conings, K.L. Jime´nez Monroy, J. D'Haen, K. Gilissen, M. D'Olieslaeger, M.K. Van Bael, P. Wagner, "Preparation of epitaxial films of the transparent conductive oxide Al:ZnO by reactive high-pressure sputtering in Ar/O2 mixtures", physica status solidi, 2012

Conference Proceedings

K. Gilissen, J. Stryckers, W. Moons, J.V. Manca, W. Deferme, "Microwave Annealing as Fast Alternative for Hotplate Annealing of Poly(3,4-ethylenedioxythiophene):Poly(styrenesulfonate)", PROC. 29th INTERNATIONAL CONFERENCE ON MICROELECTRONICS (MIEL 2014), IEEE, 2014

K. Gilissen, J. Stryckers, J.V. Manca, W. Deferme, "Towards fully spray coated organic light emitting devices ", Proc. SPIE 9183, Organic Light Emitting Materials and Devices XVIII, 918311 (October 8, 2014), doi:10.1117/12.2060994

Conference Presentations

"Microwave Annealing as Fast Alternative for Hotplate Annealing of Poly(3,4-ethylenedioxythiophene):Poly(styrenesulfonate)"
29th International Conference On Microelectronics (MIEL 2014), Institute of Electrical and Electronics Engineers (IEEE), Belgrade, Serbia, 12-15 May, 2014

"Towards fully spray coated organic light emitting devices"
Organic Photonics + Electronics 2014, "Organic Light Emitting Materials and Devices XVIII", Society of Photo-Optical Instrumentation Engineers (SPIE), San Diego, California, USA, 17-20 August, 2014

"ITO-free organic light-emitting diodes using diamond/gold-grids as transparent electrode"

European Materials Research Society (E-MRS) Spring Meeting 2015, “Symposium I: Semiconductors nanostructures towards electronic & opto-electronic device applications V”, Lille, France, 11-17 May, 2015

Poster Presentations

“Microwave annealing of PEDOT:PSS as thin film transparent electrode for large area organic based optoelectronic applications” Belgian Physical Society (BPS), Namur, Belgium 2011

“Microwave annealing, a promising step in the roll-to-roll processing of organic electronics” Materials Research Society (MRS), Boston, USA, 2011

Samenvatting

Deze thesis richt zich op nieuwe materialen en processen die de kloof overbruggen tussen de productie van Organic Light Emitting Diodes (OLEDs) op laboratoriumschaal enerzijds en op industriële schaal anderzijds.

In het eerste experimentele hoofdstuk wordt een transparante anode onderzocht als alternatief voor Indium Tin Oxide (ITO), de meest gebruikte transparante anode voor OLEDs. Indium is een essentieel onderdeel voor de meeste opto-elektronische toepassingen, maar een schaarse grondstof. Het voortbestaan van organische opto-elektronische technologie is afhankelijk van de mogelijkheid tot een kostenefficiënte massaproductie. Dit lage kosten aspect kan alleen ten volle worden bereikt door het realiseren van een indium vrije OLED. Als alternatieve transparante anode wordt Boron-doped Nano Crystalline Diamond (BNCD) met een ingewerkt gouden (Au) grid structuur onderzocht. Er wordt een overzicht gegeven van het ontstaan van transparante geleiders samen met een discussie over ITO en andere alternatieve anodes voor OLEDs. De optische, de elektrische en de morfologische eigenschappen van de BNCD:Au-grid anode worden gekarakteriseerd. Om de toepasbaarheid te onderzoeken worden de BNCD:Au-grid gebaseerde OLEDs vergeleken met referentie OLEDs met een ITO anode. Uit de resultaten wordt geconcludeerd dat de BNCD:Au-grid anode een goed indium-vrij alternatief is voor ITO.

Het tweede onderwerp van deze thesis behandelt de microgolf verwerking als thermische nabehandeling van Poly (3,4-thylenedioxythiophene): Poly (styreensulfonaat) (PEDOT: PSS) films. De PEDOT:PSS laag is een essentieel onderdeel van de OLED. Na afzetting van de laag op het substraat is een thermische behandeling essentieel om de solventen en andere additieven te verwijderen. Deze thermische behandeling wordt typisch uitgevoerd met behulp van een conventionele kookplaat of oven. Evenals bij huishoudelijk koken en industriële microgolfverwerking b.v.: voeding, keramiek, mineralen, hout en rubbers, kan het gebruik van de microgolf in het OLED productieproces een snellere verwerkingstijd en een energiebesparing opleveren. Het ontwerp van het experimentele microgolf systeem wordt in detail toegelicht. De thermische microgolf behandelingen van de lagen worden telkens herhaald met een conventionele kookplaat om zo een duidelijke vergelijking te maken tussen beide technieken. Beide droogtechnieken worden beoordeeld op basis van droogtijd. De verkregen gedroogde stalen worden dan verder morfologisch en elektrisch gekarakteriseerd. De resultaten tonen aan dat de microgolf droogtechniek een snellere techniek is voor de nabehandeling van organische halfgeleidende PEDOT: PSS films.

Het derde en laatste onderwerp van deze thesis onderzoekt een nieuwe alternatieve techniek voor spin coaten. Spin coaten is de meest gebruikte techniek in laboratoria voor onderzoek naar organische elektronica. Echter, de techniek is niet compatibel met kostenefficiënte massaproductie. Ultrasoon spray coaten is een schaalbare techniek die compatibel is met massaproductie.

Deze techniek maakt het bovendien, in tegenstelling tot spin coaten, mogelijk om patronen af te zetten tijdens de depositie. Er wordt een gedetailleerd overzicht van andere alternatieve printing en coating technieken gegeven. De effecten van ultrasone trillingen op de polymeeroplossing worden in detail onderzocht. Bovendien worden de filmvormende eigenschappen onderzocht en geoptimaliseerd door aanpassing van de oplossingseigenschappen en spray coaten parameters. Tenslotte worden deze geoptimaliseerde ultrasoon gecoate organische lagen geïntegreerd in OLEDs, om zo op het applicatieniveau een beoordeling te kunnen maken. De resultaten tonen aan dat ultrasone spray coaten een veelbelovende en massaproductie compatibele techniek is voor het productieproces van OLEDs.

In het laatste hoofdstuk wordt een algemeen overzicht en een algemene conclusie van deze thesis gepresenteerd samen met een visie op toekomstig experimenteel werk.

Summary

This thesis addresses novel materials and processes that bridge the gap between laboratory scale and industrial scale processing of Organic Light Emitting Diodes (OLEDs).

The first topic investigates an alternative transparent anode to Indium Tin Oxide (ITO), the most widely used transparent anode in organic electronic applications. Indium is scarce resource and a vital component of most optoelectronic applications. The promise of these organic optoelectronic devices lies in their low cost, high throughput processability. This low cost aspect can only be fully achieved by realizing an indium free OLED stack. As alternative transparent anode Boron-doped Nano Crystalline Diamond (BNCD) with an infused gold (Au) grid is investigated. Firstly, an overview of transparent conductors is presented along with a discussion on ITO and other alternative anodes for OLEDs. Furthermore, the construction of the BNCD:Au-grid transparent anode is described in detail and its optical, electrical and morphological properties are characterized. To investigate its applicability, the BNCD:Au-grid is incorporated in an OLED stack and compared to reference devices with an ITO anode. From these results it is conclude that the BNCD:Au-grid anode is a viable alternative to ITO.

The second topic of this thesis assesses microwave processing as post-deposition thermal treatment of Poly(3,4-thylenedioxythiophene) : Poly (styrenesulfonate) (PEDOT:PSS) thin films. The PEDOT:PSS layer is an integral part of the OLED stack, after solution deposition, a thermal treatment is needed to remove solvents and other additives. This thermal treatment is typically performed by a conventional hotplate or oven. Just as in typical household cooking, industrial microwave processing e.g.: ceramics, minerals, wood and rubbers, the use of microwave thermal annealing in the OLED production process could yield faster processing times and energy savings. The design experimental microwave setup is outlined in detail. The performed experiments on the microwave system are always repeated on a conventional hotplate to obtain a side-by-side comparison. Both annealing techniques, a conventional hotplate and the microwave system, are assessed on there annealing time. The obtained annealed samples are characterised morphologically and electrically. The Obtained results show that microwave annealing is viable and fast annealing technique for PEDOT:PSS organic films.

In the third and final topic of this thesis an alternative solution processing technique to spin coating is investigated. Spin coating is the most commonly used solution processing technique in a laboratory environment for organic electronic devices. However, the spin coating technique is not compatible with cost effective high throughput roll-to-roll industry scale processes. Ultrasonic spray coating is a scalable roll-to-roll compatible technique that allows patterning during deposition. Thin films are obtained by the superposition of micrometre droplets. Firstly, a detailed overview of other alternative solution

processing techniques is outlined. In the experimental section, the effects of the ultrasonication of the polymer solution are investigated in detail. Furthermore, the film forming properties are investigated and optimized through adapting the solution properties and spray coating parameters. Finally, these optimized organic layers are incorporated in OLEDs to evaluate the ultrasonic spray coated layers on a device level. These results show that ultrasonic spray coating is a promising technique towards the upscaling and roll-to-roll processing of OLEDs.

In the final chapter, a general overview and an overall conclusion of this thesis is presented along with an outlook on future work.

List of figures and tables

Figures

Tables

Chapter 1 Printable Organic Light Emitting Diodes

In this chapter, an overview is given, addressing the key concepts related to organic light emitting diodes. Firstly, a historical overview of the origin of organic semiconducting electroluminescent devices is presented together with their current position in the consumer market. Following this short introduction, the emphasis is on the semiconducting properties of these interesting organic materials. Hereafter follows a discussion of the optoelectronic properties leading to the emission of photons by these organic semiconductors. In the section hereafter a brief introduction is presented on the working principle of an OLED. In the section last section the current state-of-art regarding the emissive organic-metal complexes is summarised. In the last section an overview of the structure of this thesis is presented.

1.1 History of organic electronics

The majority of polymers, commonly known as plastics, e.g.: polyethylene (PE), polyvinylchloride (PVC), polyethylene terephthalate (PET), have comparable morphologic, optical and electrical properties. They consist of long-chain carbon-based organic molecules, they possess no mobile charges (insulating) and the lowest electronic excitations are in the UV region (colourless). However, in 1977, Alan MacDiarmid, Hideki Shirakawa and Alan J. Heeger discovered that the conductivity of a thin film of polyacetylene increased over seven orders of magnitude after an oxidation step with iodine vapour [1]. This doping step, the term borrowed from semiconductor technology, turned an ordinary insulating plastic into an almost metal-like conductor. The doped form of polyacetylene reached a maximum room temperature conductivity of 38 Ω^{-1} cm^{-1} whereas the initial, undoped, room temperature conductivity was 3.2 10^{-6} Ω^{-1} cm^{-1} [1]. This pioneering work earned them the Nobel Prize in chemistry of the year 2000 and started a new branch of material science: organic electronics. Since then, the field of organic electronics has progressed rapidly and produced a multitude of new applications and devices e.g.: transparent electrodes, antistatic coatings, organic photovoltaic devices (OPVs), organic transistors, organic sensors [2][3]. Furthermore, the field has also produced the organic light-emitting diode (OLED). This electroluminescent device is of great interest for applications such as: (flexible) displays, organic lasers and large area solid-state lighting.

The electroluminescence (EL) of organic compounds was already demonstrated by Bernanose et. al., a few decades earlier in 1953. However, this was achieved by exciting the organic films by a very high alternating current (AC) voltage of 500V – 2000V [4]. In 1963 electroluminescence was observed from a single-crystal anthracene by applying a direct current (DC) voltage [5].

A real breakthrough development was established in 1987 when researchers from the Eastman Kodak company reported the first OLED [6]. These devices were based on the low molecular weight carbon-backboned molecule 8-

hydroxyquinoline aluminium (Alq_3), termed small molecule, and it demonstrated the first efficient, planar organic electroluminescent device. Interestingly, one year earlier, organic photovoltaic cells were realized with an efficiency of about 1%, also by the Eastman Kodak company[7]. The electroluminescence of, larger molecular weight, polymers was first reported by Burroughes et. al. of Cambridge University in 1990 using poly(p-phenylenevinylene) (PPV) [8]. Another key development in this work is provided by the solubility of these polymers enabling the use of solution-processing techniques for the fabrication of organic electronic devices. These discoveries stimulated an immense worldwide interest and triggered a vibrant multidisciplinary field of academic research and industrial development spanning chemistry, physics, materials science, and engineering.

Today, the OLED technology is challenging well-established mainstream display technologies and emerges in the lighting industry. White OLEDs (WOLEDs) are intensively studied for applications in displays and lighting. Displays based on WOLED pixels and OLED displays, based on red, green and blue emitters, are already available in end-user products such as smart-phones and televisions. The viability of all emerging lighting and display technologies is assessed by their luminous power efficiency and this parameter is notwithstanding of prime importance for the end-user applications. The luminous power efficacy is the ratio of the integral light emitted by the light source per electrical input power. The power of the light emitted by a light source, its luminous flux, is measured in lumen and corrected for the photometric response of the human eye [9]. Figure 1.1 shows the improvements of WOLEDs over the past 20 years as compared to the luminous power efficacy of the conventional white-light sources.

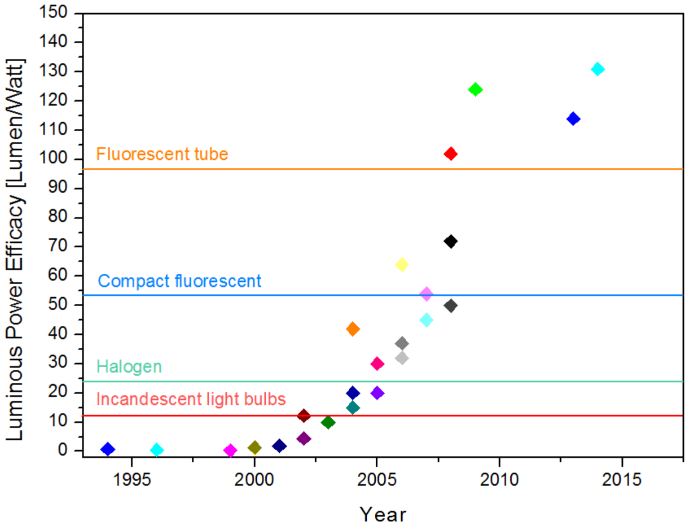

Figure 1.1: The luminous power efficacy, expressed in lumen per Watt, improvement of WOLEDs over the past 20 years (adapted from [10]).

An important milestone in the luminous power efficacy timeline is 2003. Here WOLEDs reached, under laboratory conditions, an efficacy of 15 lm/W surpassing the incandescent light bulb for the first time. However, currently, it's not yet clear if these values can be reached in mass production processes for commercial applications [10].

1.2 Organic semiconductors

Why do these organic materials possess such interesting properties? The essential feature that all organic semiconductors have in common is a π-conjugated carbon (C) backbone formed by a continuous series of alternating single and double bonds. These π-conjugated materials exists in many forms, small molecules, conjugated polymers and molecular crystals. A neutral C-atom has a total of six electrons, two of them can be found close to the nucleus in the 1s orbital, the remaining four are valence electrons and can be found in the 2s, $2p_x$ and $2p_y$ orbitals; or simplified $1s^2 2s^2 2p^2$. Each atomic orbital (AO) is differentiated by its energy level, shape and orientation as defined by the electron wave function Ψ. In a π-conjugated molecule the 2s, $2p_x$ and $2p_y$ atomic orbitals mix to form three sp^2 hybridized molecular orbitals and leaves the $2p_z$ orbital unchanged as shown in Figure 1.2.

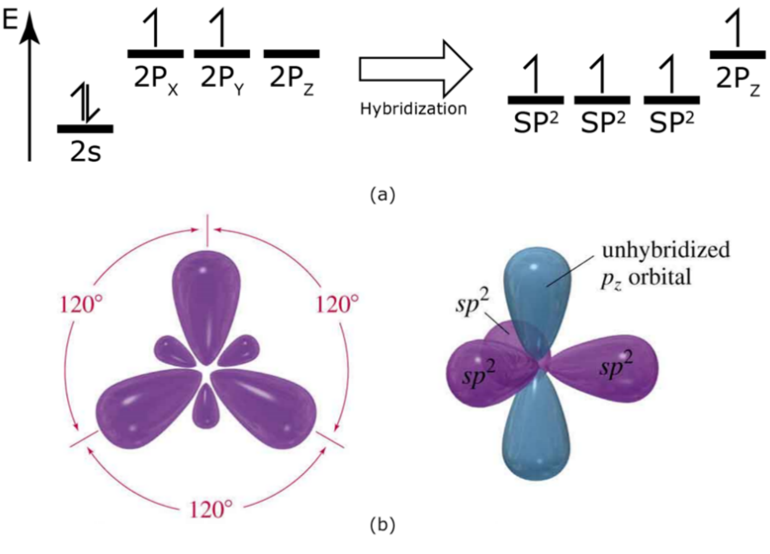

(a)

(b)

Figure 1.2: (a) Energy level representation of a neutral carbon atom and in sp^2 hybridization (b) Shape representation of carbon sp^2 hybrid orbitals [11].

The sp^2 hybrid orbitals form σ (sigma) bonds. Here the electrons are fully paired in their bonding state and have empty anti-bonding states resulting in a very strong covalently bound carbon backbone. Note that every C-atom has one sp^2

bond left over for attachment to other functional groups such as, in the simplest configuration, a hydrogen (H) atom. The possibility to add other functional groups makes π-conjugated molecules highly adjustable. Each p_z orbital contains one electron (π-electron) and each of these orbitals overlaps with the p_z orbital of its two neighbours forming π (pi) bonds. The π-electrons are relatively localized (weakly bound), give rise to delocalized electron states and are essential for the semiconducting properties of the material. Figure 1.3 shows a schematic representation of the molecular orbital energies of ethylene. When two p_z orbitals overlap and couple in phase (constructive interference), the two atomic orbitals form a π bonding molecular orbital. Each electron from their respective atomic orbitals spreads over the entire molecular orbital. When the two p_z atomic orbitals overlap and couple out of phase (destructive interference), a higher energy π* antibonding molecular orbital is formed. An electron wave function node is created, i.e. the probability of finding an electron at the internuclear region is reduced to zero. The amount of energy decrease by the formed π bonding molecular orbital is equal to the energy increase in the π* anti-bonding molecular orbital.

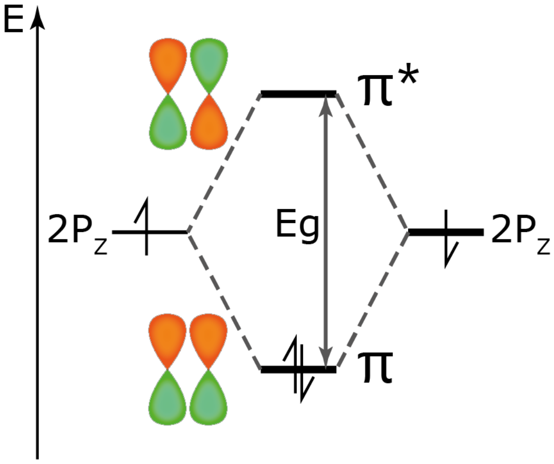

Figure 1.3: Illustration of bonding π (p_z orbitals having the same colour) and antibonding π* (p_z orbitals having opposite colours) orbital energies of two overlapping $2p_z$ orbitals.

Since it is energetically more favoured, the p_z electrons will only occupy the bonding state. In an analogous manner, overlapping sp^2 atomic orbitals, forming σ bonds, also form bonding σ and antibonding σ* states with a distinct energy gap (Eg). The energy gap between the σ and σ* states, in C-C bonds, is typically too large for perturbations in ambient conditions, e.g.: 5.5 eV in nanocrystalline diamond [12]. Trans-polyacetylene (Figure 1.4a) is the first discovered highly conductive π-conjugated polymer [1]. Each carbon atom in the backbone forms three σ bonds, one with hydrogen and two with other carbon atoms. Furthermore, each carbon atom introduces an unhybridized, half-filled p_z atomic orbital. From molecular orbital theory [11] we know that the formed molecular orbital is a linear combination of atomic orbitals. Each such linear combination results in a bonding state (no node or anti-node Ψ_+) and an antibonding state (node Ψ_-) and can accommodate exactly two electrons (with opposite spins). This principle is illustrated in Figure 1.4b for trans-polyacetylene. Notice that there are four different linear combinations depicted, no nodes being the ground state of trans-polyacetylene; all nodes being the highest energy state of trans-polyacetylene; the highest occupied molecular orbital state (HOMO); the lowest unoccupied molecular orbital (LUMO) state. Due to the high symmetry of the molecule, in this approximation, a wavelike pattern emerges in the nodal structure. As the wavelength of this pattern decreases, the energy of the molecule increases. The wavelengths of the HOMO and LUMO states are nearly identical, the only difference is that in the LUMO state the nodes are localized on the double bonds and in the HOMO state the nodes are localized in the single bonds [13].

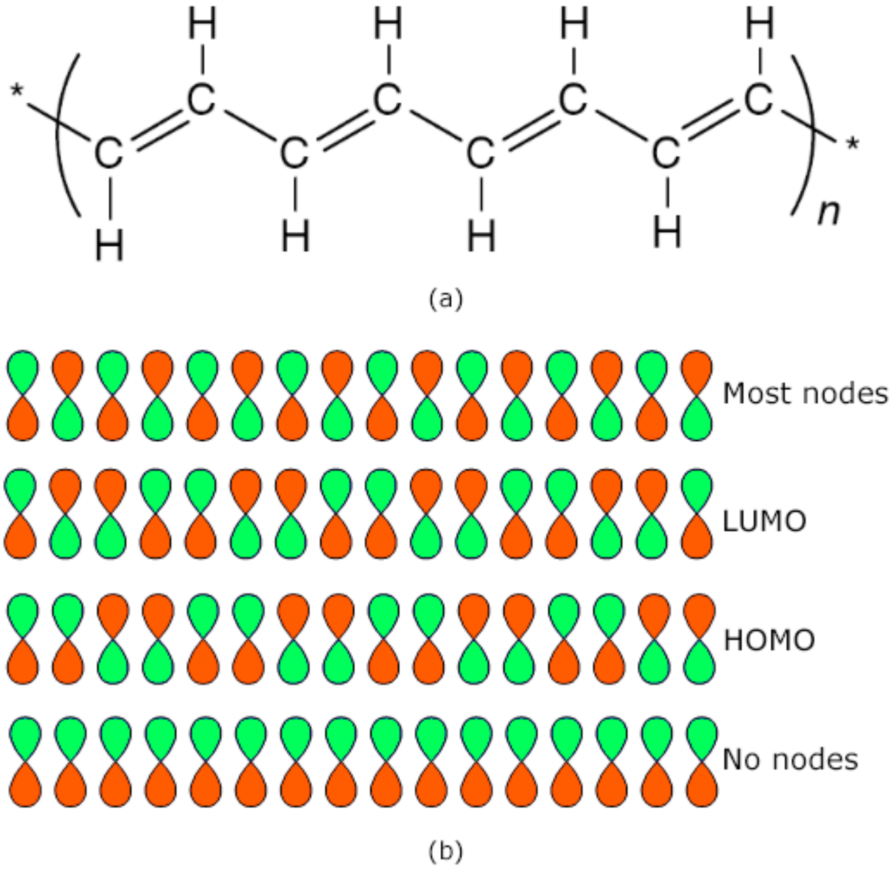

Figure 1.4: (a) Chemical structural representation of the π-conjugated trans-polyacetylene. (b) Node structure of trans-polyacetylene adapted from [13].

The number of linear combinations increase with inceasing polymer chain length, as illustrated in Figure 1.5. All bonding π lower energy states and all anti-bonding π* higher energy states are more closely spaced and form a energy band, analoge to the valence and conduction band of solid-state semiconductors. These HOMO and LUMO bands are separated by an energy gap (Eg). Note that the formed "energy band" is in principle not correct, in disordered organic semicoductors the HOMO and LUMO states do not form bands, they are comprized of manifold localized states characterized by a certain width of the density of states [14].

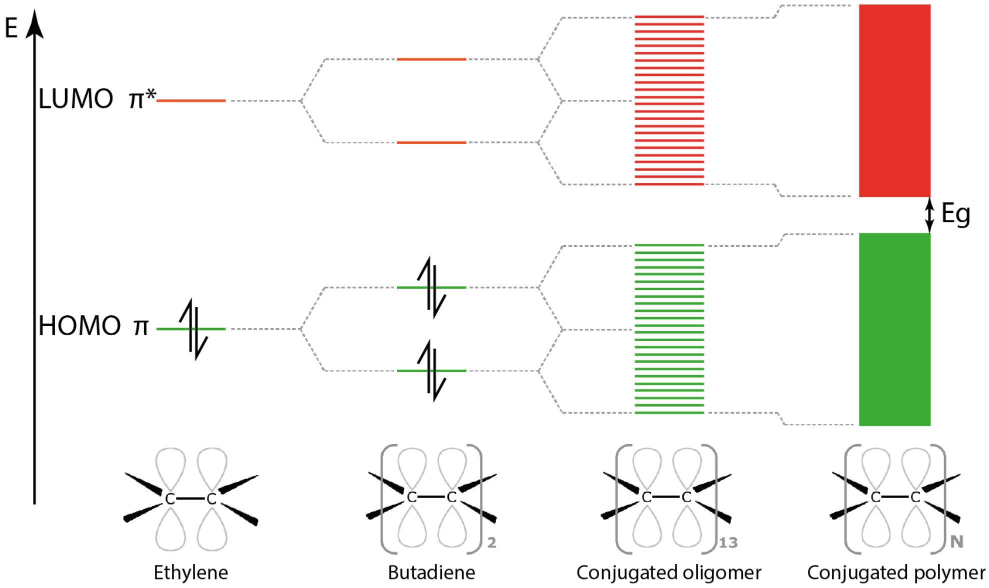

Figure 1.5: Schematic representation of the energy levels by increasing conjugation length adapted from [15].

Increasing the conjugation length will decrease the band gap, as suggested in Figure 1.5, for these polyenes. Ideally, creating a very long polyacetylene $(CH)_x$ chain will reduce it's band gap to nearly zero electron-volt (eV) and turns $(CH)_x$ into a one-dimensional (1D) metallic conductor. However, in the above approximation, the bond length alternation of single and double bonds was not taken into account. Experimental evidence [16]–[19] shows that the C-C bond length is not uniform, but there is an interatomic distance alternation in polyacetylene, i.e.: double-bonds are shorter (±1.37 Å) than the single bonds (±1.44 Å). This lattice distortion that breaks the resonant structure of the molecule is also known as the Peierls instability theory. Furthermore, the non-resonant states of the molecule are lower in energy than the resonant state, due to overall shorter bond lengths. The formation of single and double bonds lowers the energy and creates an energy gap i.e.: the HOMO-level decreases in energy and the LUMO-level increases in energy [13] [2]. Consequently, exciting an electron from the HOMO-level to the LUMO-level will shrink the single bonds and expand the double bonds (electron-lattice interactions). The band gap of these conjugated polymers, as illustrated in Figure 1.6, is remarkebly smaller as compared to saturated polymers, typically 0.8 eV – 4.0 eV [20].

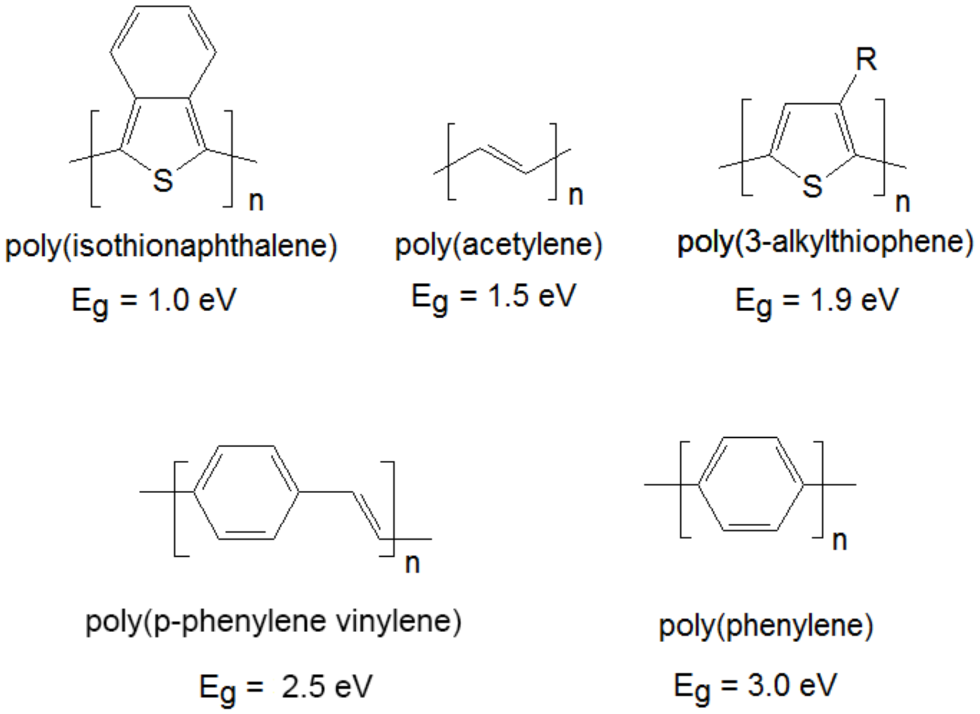

Figure 1.6: The chemical structure, name and band gap (E_g) of commonly used conjugated polymers [13].

In general conjugated polymers can be regarded as semiconductors. The conductivity of undoped conjugated polymers ranges from 10^{-6} Ω^{-1} cm^{-1} to 10^{-10} Ω^{-1} cm^{-1}, right across the insulator-semiconductor boundary [20]. This behaviour can be attributed to the presence of structure and morphological disorder, electron-lattice interaction and electron-electron interaction [13], [20]. Through the process of doping, the conductivity of specific conjugated polymers can cross the insulator-semiconductor boundary, exhibit metallic conductivities or some even keep conducting in the millikelvin range [20]. However, most conducting polymers turn into insulators at low temperatures and can therefore never truly be considered as metallic conductors. The doping process in organic semiconductors is interstitial, the dopants e.g.: iodine, potassium, sodium, intercalate between the conjugated polymer chains and donate or accept charge carriers to or from the polymer backbone. The dopants (ions), as listed in Table 1.1, are not covalently bound to the polymer chains but only attracted by the coulomb interacting forces. It is generally accepted that the doping process decreases the extent of disorder as the charge carrier density and inter-chain interactions increase [20].

Table 1.1: Effect of type of dopant ion and doping level on the conductivity of various conjugated polymers, data taken from [21].

Conjugated Polymer	Dopant ion	Doping level [mol%]	Conductivity [S/cm]
Poly(3-methylthiophene)	$CF_3SO_3^-$	0.3	30-50
		0.5	100
Polyacetylene	ClO_4^-	0.1	1000
		0.12	50
Polyacetylene	Li^+	0.1	10-100
		0.17	200
		0.2	200
Polyacetylene	K^+	0.16	50
		0.17	500

1.3 Optoelectronic properties

Apart from the remarkable semiconducting properties, organic polymer semiconductors also possess very interesting optoelectronic properties. For these conjugated polymers the onset of the absorption spectra is located in the visible and near-infrared range, corresponding to their band gap 0.8 eV – 4.0 eV [22]. As a result, these conjugated polymers exhibit the optical and electronic properties of inorganic semiconductors in combination with the mechanical properties of polymers, making them a very attractive technology for a wide variety of applications. Upon absorption of a photon, an electron (e^-) is promoted from the HOMO energy band to the LUMO energy band and leaves a hole (h^+) behind in the HOMO energy band. This excited state is very localized, it usually occurs on one molecule due to weak intermolecular van-der-Waals interaction. The formed quasi-particle, an exciton, is an electron-hole pair bound by their electrostatic interaction. The exciton is localized on one molecule and both charges are very strongly bound. The high exciton binding energy, typically 0.5 eV, is due to the short charge carrier distance, typically 1 nm, and the low dielectric constant, ε_r = 3-4, of these conjugated polymers [22]. The low dielectric constant of conjugated polymers is related to the relatively low, compared to inorganic semiconductors, total electron density. As a result, the electrostatic electron interactions cannot be neglected. Detailed quantum physical calculations predict the energies associated with electron-electron correlation to be in the order of 0.5 eV [22]. Furthermore, the thermal energy at room temperature is $k_B.T$ = 25 meV, the excitons are not separated into free holes and electrons upon light absorption. By disregarding the strong exciton binding energy and electron-electron interaction, the absorption of a photon results in the formation of a freely moving electron and hole. A small voltage should be sufficient to move these charges (photoconduction). However, as experimentally shown [23], the onset of photoconduction is observed at higher photon energies than the onset of photon absorption. These charge separation processes and the associated energies are of major concern for organic photovoltaics [24]. For organic light-emitting diodes, strong exciton energies are favourable, excitons are formed by injection of holes and electrons [25]. Since exciton diffusion lengths are typically 1 - 10 nm and its lifetime is limited to a few nanoseconds, the probability of non-radiatively exciton recombination due to defects and impurities in the organic film is small [26].

Upon the formation of an exciton, when an electron is excited form the HOMO orbital to the LUMO orbital, the electron no longer occupies the same spatial orbital. According to Pauli's exclusion principle, the restriction on the possible spin states is lifted. There are now four possible orientations of their spin states, as depicted in Figure 1.7.

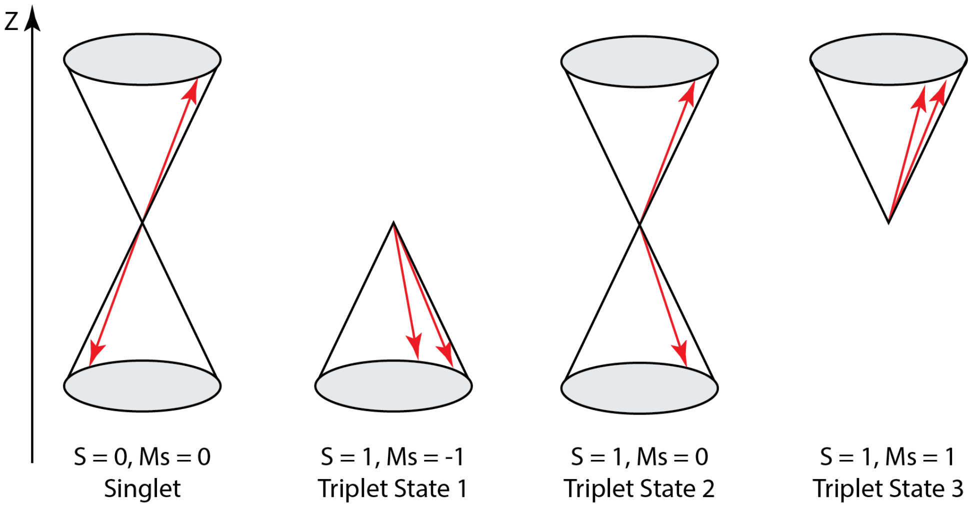

Figure 1.7: Singlet and triplet states depicted as vector diagrams. In the anti-parrallel spin arragment, the net spin angular momentum Ms = 0 and their total spin S = 0 and their state is called the singlet state. When the spins are parrallel, the spins do not cancel each other, their total spin is one (S = 1) and there are three possible configurations called the triplet states.

These four possible spin states give rise to the four lowest excited states, the lowest excited singlet state S_1 and the three lowest triplet states T_1. Due to the low dielectric of conjugated polymers and the high electron-electron interaction, the triplet states are the lowest excited states [22]. When the material absorbs light, an electron transition takes place from the ground state S_0 to a higher energy state S_n depending on the photon energy, as depicted in Figure 1.8. Electrons in state S_n relax to state S_1, this process is called internal conversion, by thermal dissipation. Alternatively, electrons occupying a high energy state S_n can relax to the excited triplet states T_1, by spin-inversion through spin-orbit interaction, termed intersystem crossing [26]. After these initial relaxation processes, the recombination of the electron with a hole will occur. There are three possible recombination routes [26] [27]: fluorescence from the singlet excited state S_1 to S_0, non-radiative recombination from the singlet excited state S_1 to S_0 and phosphorescence from the triplet excited state T_1 to S_0. Each fluorescent and phosphorescent recombination process yields a photon. The light-emission from an electron-hole recombination processes is more generally defined as photoluminescence (PL). The energy released during a non-radiative recombination is lost and produces heat. Note that optical transitions from the ground state S_0 to the lowest triplet states (T_1) are quantum mechanically forbidden, however the incorporation of heavy ions (e.g.: Pt, Ir) facilitates intersystem crossing and greatly increasing the phosphorescent emissions [22].

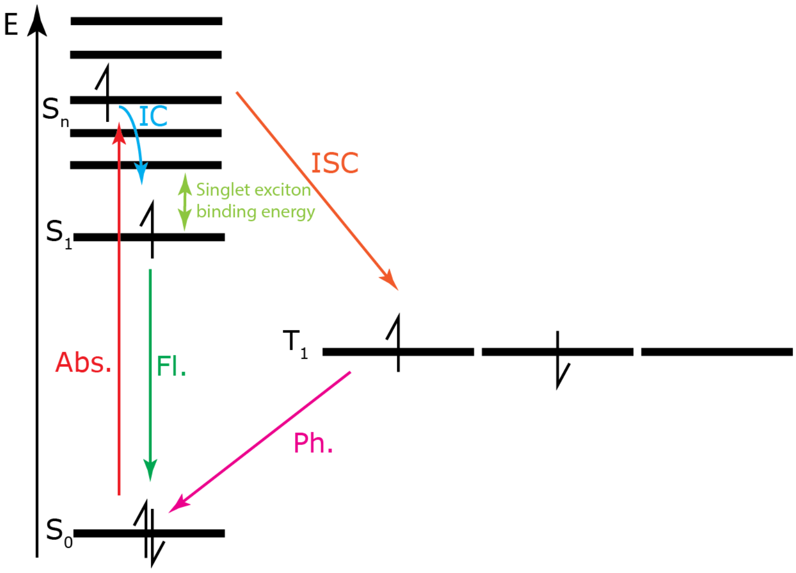

Figure 1.8: Jablonski diagram, exciton formation state diagram. (Abs.: Absorption; Fl.: Fluorescence; Ph.: Phosphorescence; S_0: Singlet ground state; S_1: Lowest singlet excited state; S_n: Higher singlet excited states) T_1: Lowest triplet excited states; IC: Internal Conversion; ISC: Intersystem Crossing)

1.4 Organic Light Emitting Diodes (OLEDS)

The interesting mechanical, semiconducting and optoelectronic properties of conjugated polymers can be exploited in a range of novel applications such as OLEDs [28], OPVs [29], organic transistors [30], organic sensors [31]. Within the scope of this thesis the device physics of OLEDs is summarized here. The most basic structure of an OLED is illustrated in Figure 1.9a, a single layer of conjugated polymer is sandwiched between two electrodes. The first electrode, the anode, on top of the transparent substrate is a transparent conductor to facilitate light extraction from the device. Since the first reported OLED, indium tin oxide (ITO) is the most commonly used transparent anode [6]. The solution processable polymer layer, also known as the emissive layer, determines the electrolumincent spectrum of the device. The top electrode, the cathode, is a metal deposited by thermal evaporation. When discussing devices, it is convenient to make use of the band diagram structure of the OLED, in forward bias as shown in Figure 1.9b. The indicated HOMO and LUMO level reflect the average energy levels of the entire film. The workfunction of the anode and cathode are denoted respectively χ_a and χ_c. The difference in workfunction between the anode and cathode give rise to a so called "built-in potential" (V_{bi}) [32], which must be overcome in order for current to flow and for the OLED to be in the forward bias regime ($V_{bias} > V_{bi}$). The forward bias regime is achieved by applying a positive direct current (DC) voltage, e.g.: 3V-10V from the anode to the cathode.

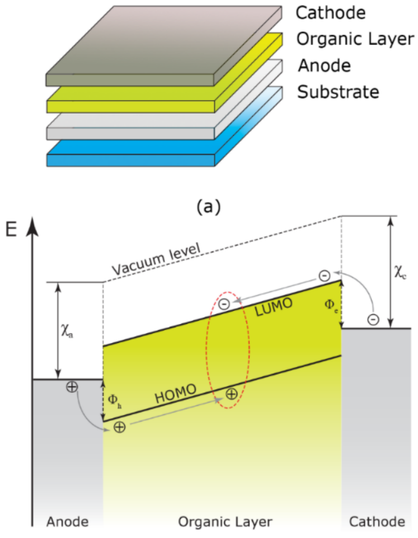

(a)

(b)

Figure 1.9: Structure (a) and band diagram (b) of prototypical OLED. (a) The OLED consists out of a single organic layer sandwiched between an anode and a cathode on top of a substrate. (b) The band diagram of the OLED under forward bias, adapted from [33].

Under forward bias, the electrodes facilitate charge injection, holes from the anode and electrons from the cathode. Under the local electric field, typically in order of 10^6 V/m, the charge carriers are transported through the polymer layer. Inside the organic layer the holes and electrons recombine to form excitons. These excitons can then decay radiative or non-radiative. Thus there are three fundamental processes underpinning the OLED device operation: charge injection, charge transport and recombination [34].

For both holes and electrons the charge injection process is dominated by a charge injection barrier, the transparent anode – organic layer interface barrier (Φ_h) and the organic layer – metal interface barrier (Φ_e), respectively. The vacuum level is defined as the minimum energy needed to remove and electron from a solid. The energy difference between the LUMO and vacuum level is the electron affinity (A_e). The energy separation between the HOMO and vacuum level is the ionization energy (I_E). According to the Mott-Schottky rule of molecular orbital interfaces, the interface barriers can be expressed as follows [26][35]:

$$\Phi_e = \chi_c - A_e - \Delta \tag{1.1}$$

$$\Phi_\mathrm{h} = \mathrm{I_E} - \chi_\mathrm{a} + \Delta \tag{1.2}$$

However at the electrode/organic interface vacuum level alignment is not achieved due to the formation of an interface dipole [36]. This interface dipole induces an abrupt change (Δ) that can be as high as 1 eV in the vacuum level at the interface. There are several possible theories on its origin and at the present there is no finale confirmed theory [37].

Over the past decades classical models like Fowler-Nordheim tunnelling and Thermionic emission have been applied to describe the injection of charge carriers into disordered organic-semiconductors [35]. However these models are not adequate as they describe delocalized charge carrier injection into solids, an overview can be found in [38]. Currently more advanced models are under investigation to describe the injection of electrical current into organic semiconductors like the Hopping injection: Arkhipov model and Emtage/O'Dwyer model [39].

The charge transport mechanism in disordered organic-semiconductors is currently not well understood [26]. The constituent molecules of the disordered organic solid are kept mainly together by weak van der Waal's interaction. This implies that adding, removing or moving a charge carrier (hole or electron) on a molecule will lead to a significant distortion of the molecule's geometry i.e.: changes in bond length of neighbouring bonds which in turn changes the energetic state. Upon acquiring a charge, the molecule tends to lower its total energy by reorganizing its internal structure. This energy is referred to as the reorganization energy (λ) [13]. The particular combination of a charge with its induced distortion is called a polaron. When an electron is added an electron-polaron is formed, removing an electron will create a hole-polaron. The mobility (μ) of these organic semiconducting materials is low ($\mu \approx 10^{-6}$ cm^2/Vs) compared to inorganic semiconductors like crystalline silicon ($\mu \approx 10^3$ cm^2/Vs). The charge carrier transport is viewed as a hopping transport where the electrons hop from one molecule to the next, in contrast to inorganic semiconductors where the transport is considered as ballistic. This hopping charge transport formalism is currently extensively studied e.g.: polaron hopping, hopping in a disordered density of state, variable range hopping and a more macroscopic approach the drift-diffusion framework, a detailed overview can be found [40].

As both charge carries, under influence of an externally applied electric field, are injected and transported in opposite directions through the organic semiconductor, electron-hole pairs, excitons, are formed. Recently it was shown that Langevin-type and Shockley-Read-Hall (SRH) recombination processes both occur in OLEDs [41]. The SRH recombination process assumes that free holes can only recombine with trapped electrons and vice versa. The charge carriers get trapped in film defects and impurities. The trap level is situated inside the energy gap, between the HOMO and LUMO energy levels. This trap-mediated recombination process is often non-radiative or weak radiative and predominant at low bias voltages [42]. In contrast to the SRH recombination process, the Langevin model describes the recombination of electrons and holes that are both free [32]. In essence the recombination of electrons and holes will occur when they are within each other's Coulomb attraction radius. More precisely when the associated Coulomb potential is equal or larger than the thermal energy kT. The radiative process in OLEDs is dominated by Langevin type recombination and is therefore essential to the improvement of these devices [41], [42].

It is evident that a single-layer OLED, anode/polymer/cathode, is not the most efficient design, as shown in Figure 1.9. As electrons and holes are injected and transported through the device it is essential that they form excitons and recombine radiative. However it is also possible that the electrons reach the anode and the holes reach the cathode without forming excitons, recombining and generating light. Furthermore, formed excitons near the cathode can also be quenched, the energy of the formed exciton is transferred to the metal non-radiative [41]. To ensure a respectable electroluminescent (EL) yield, multilayer device architectures are employed. This was already the case with Tang's first OLED, which was a two-layer OLED architecture consisting of a diamine layer and an Alq_3 layer [6]. In this device the diamine layer acts as a hole transporting layer (HTL) and the Alq3 layer acts as the emissive layer (EML). Due to the different HOMO and LUMO levels of both materials, the electrons are blocked at the interface increasing the probability of exciton formation.

To achieve high efficient OLEDs, multilayer architectures are used [10], aside from the emissive layer, a multitude of interlayers are employed. Each interlayer is specifically tailored for its function within the OLED. Such an OLED could encompass to following interlayers: a hole injection layer (HIL); a hole transport layer (HTL); an electron blocking layer; an electron injection layer (EIL); an electron transport layer (ETL) and a hole blocking layer (HBL), as shown in Figure 1.10. The purpose of these interlayers is to facilitate the injection and transport of both charge carriers towards the EML and confine the created excitons. The injection interlayers HIL and EIL reduce the injection barriers for the injection of holes and electrons (respectively). The blocking layers HBL and EBL lower the leakage current, electrons and holes that reach the opposite electrode and confine the generated excitons in the emissive layer.

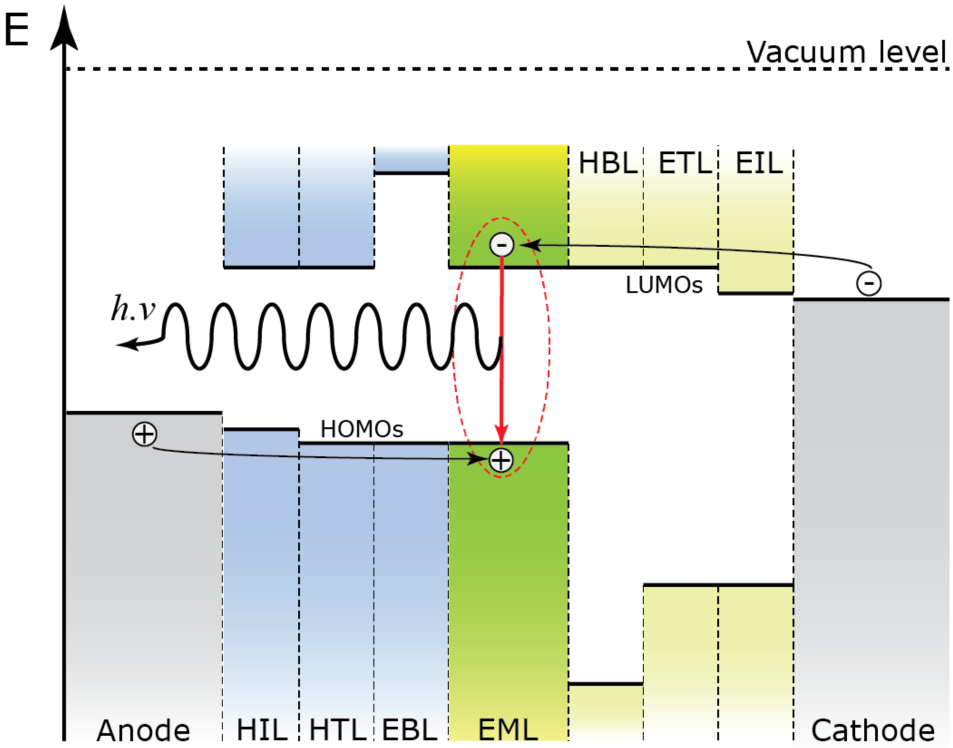

Figure 1.10: Energy Level diagram of a high efficient OLED stack. (HIL: hole injection layer; HTL: hole transport layer; EBL: electron blocking layer; EIL: electron injection layer; ETL: electron transport layer; HBL: hole blocking layer)

Towards obtaining a predefined emission spectrum from the OLED, the emissive layer can be modified or comprise out of a stack of emissive layers [10]. A single layer can be blend with lumiphores or an emissive layer stack can be used with several emitting layers on top of each other. Other techniques to obtain the desired emission spectrum encompass the use of multiple monochrome OLED stacks connected by charge generation layers or spatially multiplexing monochromic OLEDs [10]. These methods are commonly employed for the purpose of generating white light, to obtain so called WOLEDs.

1.5 State-of-the-art

The organic semiconductor materials used in OLEDs can be divided into two distinct classes based on their molecular structure, conjugated small molecules [6] and polymers [8], discovered only three years apart. Small molecule OLEDs are most commonly prepared by consecutive thermal evaporation steps of organic layers. On the other hand polymer based OLEDs are prepared by solution processing techniques e.g.: spin-coating, ink-jet printing. Currently, driven by an intense research effort of academia and industry, OLEDs from both material classes, small molecules and conjugated polymers, have reached internal quantum efficiencies (IQE) of ~100 % [43][44]. However, early emissive materials used in OLEDs were bound to a theoretic maximum IQE of 25 %. The emissive materials of these OLEDs were exclusively fluorescent emitters by radiative decay of singlet excitons. Depending on the relative orientation of the electron spin momenta, its excited state can either be the singlet excited state or the triplet excited state. From spin-statistics it is known that the ratio of singlet excitons to triplet excitons is 1:3 [45]. Radiative transitions from the triplet excited state to the singlet ground state is kinetically unfavourable [46]. By the use of phosphorescent emitters, exploiting triplet exciton radiative decay, the theoretic limited IQE of 25 % is raised to 100 %. By the incorporation of transition metal complexes the singlet excited states undergo rapid intersystem-crossing to the phosphorescent triplet states due to spin-orbit coupling, i.e. interaction between an electron’s spin and orbital magnetic moments [47]. The phosphorescent radiative decay from the triplet states involves an internal charge transfer reaction in the transition metal complex between the centrally located metal and its surround ligands. The emission spectrum can easily be tuned by adapting the chemical structure of the ligands surrounding the metal complex [46]. A commonly employed method to incorporate these phosphorescent emitters is to introduce them as a guest dye into a host small molecule or polymer emissive layer, thus obtaining a hybrid fluorescence-phosphorescence system [47]. The most commonly used transition metal complex, as shown in Figure 1.11, to utilize phosphorescent emission is the cyclometalated iridium (III) complex Ir(ppy)_3, owing its popularity to its high phosphorescent yield, its high thermal stability and the ease of making structural modifications to tune the excited states [48]. Its high versatility allows colours over the whole visible spectrum, from blue to red. A promising alternative for the iridium (III) complex is the platinum (II) complex, also shown in Figure 1.11, due to its unique square planar geometry [48]. Due to the high cost and toxicity of iridium and platinum other alternative transition metal complexes are being introduced, such as gold.

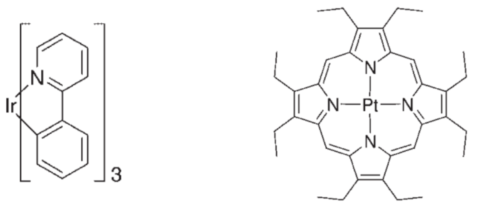

tris(2-phenylpyridine)-iridium(III) (Ir(ppy)_3)

2,3,7,8,12,13,17,18 - octaethyl - 21H,23H - porphine platinum(II) (PtOEP)

Figure 1.11: Chemical structure, name and abbreviation of most commonly used transition metal complexes, adapted from [46].

A very extensive review of state-of-the-art materials and OLED device architectures can be found in [43], [48][49]. Recently, a large ongoing research effort has focussed on the development of solution processable fluorescent-phosphorescent small molecules combining the high efficiency of small molecules and the ease of deposition by solution processing [49]–[51]. However, small molecules, deposited by vacuum evaporation, are currently still the organic material and deposition method of choice for commercial applications such as smart-phone displays and TV screens.

1.6 Structure & Aims of this thesis

The *ideal process* for the fabrication of organic optoelectronic devices, as formulated by Frederik C. Krebs [52], should exhibit the following characteristics. A transparent electrode free from costly indium and compatible with flexible substrates. The consecutive organic and metallic layers should be processed from solution by as few coating or printing techniques as possible. Furthermore, the entire production process should have as low environmental impact as possible by avoiding toxic solvents and taking into account the recyclability of the final device. The aim of this thesis is to contribute towards this ideal process and is organized as described below.

In this chapter, **chapter 1**, an overview of the key concepts regarding organic light emitting diodes is presented. Along with an historical overview the semiconducting and optoelectronic properties are discussed. Hereafter, the working principle of OLEDs is introduced and the current state-of-art of organic emissive materials is summarised. In **chapter 2**, the experimental and theoretical details of the main characterisation techniques to study organic thin films and OLEDs are treated. Firstly an overview of the perception of light and the corresponding photo-physical units are presented. Hereafter, characterisation methods to study the light-emission and electrical behaviour of OLEDs are described. In the following sections, thin-film characterisation techniques to study their electrical properties and nano-scale morphology are highlighted. In the last section a detailed description is given related to the OLED device preparation and materials used.

As a first step towards the *ideal process* described by Krebs, in **chapter 3**, a novel alternative indium free transparent electrode is explored. First an overview of transparent electrodes is presented. Hereafter, the preparation of our novel carbon-gold based electrode is outlined. Further on, our electrode is characterized and optimized towards high transparency in combination with high conductivity. Hereafter its performance is assessed by comparison to the standard ITO transparent electrode applied in OLED devices.

Most solution processed organic layers need a consecutive thermal treatment for solvent and additive removal from the layer. In **chapter 4** we explore the use of microwave heating as faster alternative post-deposition treatment of the organic hole blocking layer poly(3,4-thylenedioxythiophene) : poly(styrenesulfonate) (PEDOT:PSS).

In the *ideal process* the deposition technique used should be a fast printing technique compatible with all the layers of the organic optoelectronic devices. To meet these requirements we explore ultrasonic spray coating as deposition technique for the emissive layer of OLEDs, in **chapter 5**. After an overview of coating and printing techniques we investigate the effects of the ultrasonication and characterise its thin-film forming properties as function of ultrasonic spray coating parameters. Hereafter, the OLED device efficacies of devices with ultrasonically spray coated emissive layers is compared to reference spin-coated devices.

Chapter 6 outlines the general conclusions of this work and looks ahead towards future possibilities and improvements based on these findings.

1.7 References

[1] H. Shirakawa, E. J. Louis, A. G. MacDiarmid, C. K. Chiang, and A. J. Heeger, "Synthesis of Electrically Conducting Organic Polymers : Halogene Derivatives of Polyacetylene, (CH)x," *J. C. S. Chem. Comm*, no. 578, pp. 578–580, 1977.

[2] A. J. Heeger, "Nobel Lecture : Semiconducting and metallic polymers : generation of polymeric materials," *Rev. Mod. Phys.*, vol. 73, no. July, pp. 681–700, 2001.

[3] C. N. Hoth, P. Schilinsky, S. a Choulis, S. Balasubramanian, and C. J. Brabec, "Applications of Organic and Printed Electronics," in *Applications of Organic and Printed Electronics: A Technology-Enabled Revolution*, 2013, pp. 27–56.

[4] A. Bernanose, M. Comte, and P. Vouaux, "A new method of emission of light by certain organic compounds," *J. Chim. Phys. Physico-Chimie Biol.*, vol. 50, pp. 64–68, 1953.

[5] M. Pope, H. P. Kallmann, and P. Magnante, "Electroluminescence in Organic Crystals," *J. Chem. Phys.*, vol. 38, no. 8, p. 2042, 1963.

[6] C. W. Tang and S. A. VanSlyke, "Organic electroluminescent diodes," *Appl. Phys. Lett.*, vol. 51, no. 12, pp. 913 – 915, 1987.

[7] C. W. Tang, "Two-layer organic photovoltaic cell," *Appl. Phys. Lett.*, vol. 48, no. 2, pp. 183–185, 1986.

[8] J. H. Burroughes, D. D. C. Bradley, A. R. Brown, R. N. Marks, K. Mackay, R. H. Friend, P. L. Burns, and A. B. Holmes, "Light-emitting diodes based on conjugated polymers," *Nature*, vol. 347, no. 6293, pp. 539–541, 1990.

[9] S. R. Forrest, D. D. C. Bradley, and M. E. Thompson, "Measuring the Efficiency of Organic Light-Emitting Devices**," *Adv. Mater.*, vol. 15, no. 13, pp. 1043–1048, Jul. 2003.

[10] M. C. Gather, A. Köhnen, and K. Meerholz, "White organic light-emitting diodes," *Adv. Mater.*, vol. 23, no. 2, pp. 233–248, 2011.

[11] P. Atkins and J. de Paula, *Atkins' Physical Chemistry*, 7th ed. Oxford University Press, 2002.

[12] M. Daenen, O. A. Williams, J. D'Haen, K. Haenen, and M. Nesládek, "Seeding, growth and characterization of nanocrystalline diamond films

on various substrates," *Phys. status solidi*, vol. 203, no. 12, pp. 3005–3010, Sep. 2006.

[13] S. C. J. Meskers, "Organic electronics lecture 1a: pi-conjugated molecules (lecture notes)." TU Eindhoven, 2012.

[14] R. Coehoorn, "Organic electronics lecture 7: OLED device models (lecture notes)." TU Eindhoven, Einhoven, 2012.

[15] M. Rehahn, "Elektrisch leitfähige Kunststoffe: Der Weg zu einer neuen Materialklasse," *Chemie unserer Zeit*, vol. 37, no. 1, pp. 18–30, 2003.

[16] C. Fincher, C. Chen, a. Heeger, a. MacDiarmid, and J. Hastings, "Structural Determination of the Symmetry-Breaking Parameter in trans-(CH)_{x}," *Phys. Rev. Lett.*, vol. 48, no. 2, pp. 100–104, 1982.

[17] H. Kahlert, O. Leitner, and G. Leising, "Structural properties of trans- and cis-(CH)x," *Synth. Met.*, vol. 17, no. 1–3, pp. 467–472, 1987.

[18] Q. Zhu, J. E. Fischer, R. Zusok, and S. Roth, "Crystal structure of polyacetylene revisited: An x-ray study," *Solid State Commun.*, vol. 83, no. 3, pp. 179–183, 1992.

[19] C. S. YANNONI and T. C. CLARKE, "MOLECULAR-GEOMETRY OF CIS-POLYACETYLENE AND TRANS-POLYACETYLENE BY NUTATION NMR-SPECTROSCOPY," *Phys. Rev. Lett.*, vol. 51, no. 13, pp. 1191–1193, 1983.

[20] R. Kiebooms, R. Menon, and K. Lee, "Synthesis, electrical and optical properties of conjugated polymers," in *Handbook of advanced electronic and photonic materials and devices*, 1st ed., H. S. Nalwa, Ed. Adacdemic Press, 2001, pp. 1–86.

[21] P. Kar, *Doping in conjugated polymers*, 1st ed. Scivener Publishing - Wiley, 2013.

[22] S. C. J. Meskers, "Organic electronics lecture 2: Opto-electronic properties of conjugated polymers (lecture notes)." TU Eindhoven, 2012.

[23] S. Barth and H. Bässler, "Intrinsic Photoconduction in PPV-Type Conjugated Polymers," *Phys. Rev. Lett.*, vol. 79, no. 22, pp. 4445–4448, 1997.

[24] P. W. M. Blom, V. D. Mihailetchi, L. J. a. Koster, and D. E. Markov, "Device Physics of Polymer:Fullerene Bulk Heterojunction Solar Cells," *Adv. Mater.*, vol. 19, no. 12, pp. 1551–1566, Jun. 2007.

[25] P. W. M. Blom, M. J. M. De Jong, and C. T. H. F. Liedenbaum, "Device Physics of Polymer Light-emitting Diodes," *Polym. Adv. Technol.*, vol. 9, pp. 390–401, 1998.

[26] F. So, *Organic Electronics: Materials, Processing, Devices and Applications*. CRC Press, 2010.

[27] L. Pereira, *Organic Light-Emitting Diodes: the use of rare-earth and transition metals*. CRC Press, 2012.

[28] M. S. Alsalhi, J. Alam, L. A. Dass, and M. Raja, "Recent advances in conjugated polymers for light emitting devices.," *Int. J. Mol. Sci.*, vol. 12, no. 3, pp. 2036–54, Jan. 2011.

[29] Y. Galagan, R. Andriessen, E. Rubingh, N. Grossiord, P. Blom, S. Veenstra, W. Verhees, and J. Kroon, "Toward fully printed Organic Photovoltaics : Processing and Stability," no. Dmp 2831, pp. 5–8, 2010.

[30] B. Crone, a Dodabalapur, Y. Lin, R. Filas, Z. Bao, a LaDuca, R. Sarpeshkar, H. Katz, and W. Li, "Large-scale complementary integrated circuits based on organic transistors," *Nature*, vol. 403, no. 6769, pp. 521–3, 2000.

[31] D. Tyler McQuade, A. E. Pullen, and T. M. Swager, "Conjugated polymer-based chemical sensors," *Chem. Rev.*, vol. 100, no. 7, pp. 2537–2574, 2000.

[32] M. Kemerink, "Organic electronics lecture 5: Simple device models (lecture notes)." TU Eindhoven, 2012.

[33] I. D. Parker, "Carrier tunneling and device characteristics in polymer light-emitting diodes," *J. Appl. Phys.*, vol. 75, no. 3, pp. 1656–1666, 1994.

[34] P. W. M. Blom and M. C. J. M. Vissenberg, "Charge transport in poly (p-phenylene vinylene) light-emitting diodes," *Mater. Sci. Eng.*, vol. 27, pp. 53–94, 2000.

[35] M. Kemerink, "Organic electronics lecture 6: Contacts and injection (lecture notes)." TU Eindhoven, Einhoven, 2012.

[36] S. Braun, W. R. Salaneck, and M. Fahlman, "Energy-level alignment at organic/metal and organic/organic interfaces," *Adv. Mater.*, vol. 21, no. 14–15, pp. 1450–1472, 2009.

[37] R. Coehoorn, "Organic Electronics lecture 8: Interfaces (lecture notes)." TU Eindhoven, 2012.

[38] J. C. Scott, "Metal–organic interface and charge injection in organic electronic devices," *J. Vac. Sci. Technol. A Vacuum, Surfaces, Film.*, vol. 21, no. 3, p. 521, 2003.

[39] T. Van Woudenbergh, "Charge Injection Into Organic Semiconductors," 2005.

[40] S. D. Baranovskii, O. Rubel, F. Jansson, and R. Osterbacka, "Description of Charge Transport in Disordered Organic Materials," *Adv. Polym. Sci.*, vol. 223, no. June 2009, pp. 45–71, 2010.

[41] M. Kuik, L. J. a. Koster, a. G. Dijkstra, G. a. H. Wetzelaer, and P. W. M. Blom, "Non-radiative recombination losses in polymer light-emitting diodes," *Org. Electron.*, vol. 13, no. 6, pp. 969–974, Jun. 2012.

[42] G. A. H. Wetzelaer, M. Kuik, H. T. Nicolai, and P. W. M. Blom, "Trap-assisted and Langevin-type recombination in organic light-emitting diodes," *Phys. Rev. B*, vol. 83, no. 165204, pp. 1–5, 2011.

[43] H. Jeong, H. Shin, J. Lee, B. Kim, Y.-I. Park, K. S. Yook, B.-K. An, and J. Park, "Recent progress in the use of fluorescent and phosphorescent organic compounds for organic light-emitting diode lighting," *J. Photonics Energy*, vol. 5, no. 1, p. 057608, 2015.

[44] X. Yang, D. C. Müller, D. Neher, and K. Meerholz, "Highly efficient polymeric electrophosphorescent diodes," *Adv. Mater.*, vol. 18, no. 7, pp. 948–954, 2006.

[45] M. Baldo, D. O'Brien, Y. You, A. Shoustikov, S. Sibley, M. E. Thompson, and S. R. Forrest, "Highly efficient phosphorescent emission from organic electroluminescent devices," *Nature*, vol. 395, no. 6698, pp. 151–154, 1998.

[46] A. Van Dijken, K. Brunner, H. Börner, and B. M. W. Langeveld, "9 High-Efficiency Phosphorescent Polymer LEDs," in *Highly Efficient OLEDs with Phosphorescent Materials*, 2008, pp. 311–328.

[47] S. Reineke and M. a. Baldo, "Recent progress in the understanding of exciton dynamics within phosphorescent OLEDs," *Phys. Status Solidi Appl. Mater. Sci.*, vol. 209, no. 12, pp. 2341–2353, 2012.

[48] W. C. H. Choy, W. K. Chan, and Y. Yuan, "Recent advances in transition metal complexes and light-management engineering in organic optoelectronic devices," *Adv. Mater.*, pp. 1–32, 2014.

[49] K. S. Yook and J. Y. Lee, “Small molecule host materials for solution processed phosphorescent organic light-emitting diodes,” *Adv. Mater.*, vol. 26, no. 25, pp. 4218–4233, 2014.

[50] L. Hou, L. Duan, J. Qiao, D. Zhang, G. Dong, L. Wang, and Y. Qiu, “Efficient solution-processed small-molecule single emitting layer electrophosphorescent white light-emitting diodes,” *Org. Electron.*, vol. 11, no. 8, pp. 1344–1350, Aug. 2010.

[51] L. Xiao, Z. Chen, B. Qu, J. Luo, S. Kong, Q. Gong, and J. Kido, “Recent progresses on materials for electrophosphorescent organic light-emitting devices,” *Adv. Mater.*, vol. 23, no. 8, pp. 926–952, 2011.

[52] F. C. Krebs, “Fabrication and processing of polymer solar cells: A review of printing and coating techniques,” *Sol. Energy Mater. Sol. Cells*, vol. 93, no. 4, pp. 394–412, Apr. 2009.

Chapter 2 Experimental Methodology

In this chapter an overview of the measurement techniques and sample preparation details used in this thesis is given. In the first section, the photo-physical quantities and their corresponding units are highlighted followed by a detailed description treating the used characterisation method for OLEDs. In the next section the thin-film electrical property of sheet-resistance and its measurement technique by means of the Van Der Pauw method are outlined. Further on, microscopy techniques, atomic force microscopy (AFM) and scanning electron microscopy (SEM) will be described. In the last section, the details on the subject of solution and sample preparation will be presented.

2.1 Perception of light

OLEDs are self-emitting two-dimensional light sources, as shown in Figure 2.1. The efficacy is an important metric of OLED devices to gain insight in the physics of their operation and their performance towards end-user applications such as display and solid-state-lighting (SSL) technologies.

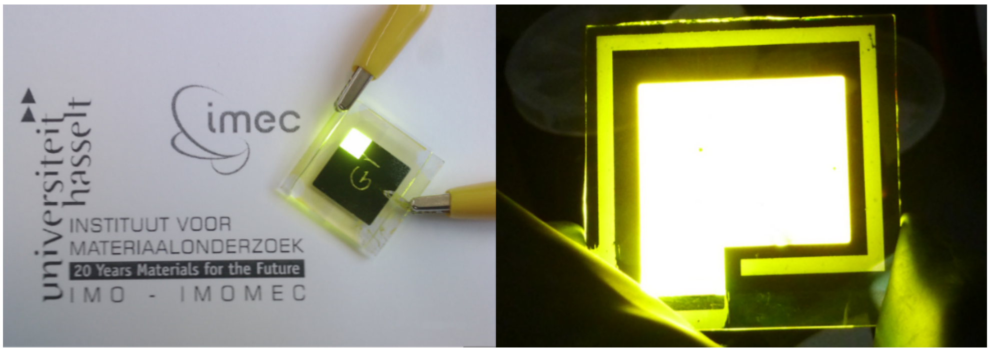

Figure 2.1: Photographs of OLEDs prepared at the Institute for Materials Research (IMO) of Hasselt University.

In general, there are two main categories for the photo-physical properties of light: radiometric units and photometric units. Radiometric units describe the properties of light in physical units in terms of energy and power, without reference to wavelength. Photometric units describe the parameters of light with respect to the perception of the human eye. A photometric Systeme International d'Unites (SI) base unit representing the intensity of a light source as perceived by the human eye is the luminous intensity, measured in candela (cd). One candela is defined as [1]: *The candela is the luminous intensity, in a given direction, of a source that emits monochromatic radiation of frequency* $540\ 10^{12}$ *Hz and that has a radiant intensity in that direction of 1/683 W* sr^{-1}*.* The SI unit for the flux of light, the luminous flux, is the amount of light emitted per second produced by a light source and is defined as [1]: *a monochromatic light source emitting an optical power of (1/683)W at 555 nm has a luminous* *flux of 1 lumen (lm)*. An isotropic emitter with a luminous intensity of 1 cd will therefore have a luminous flux of 4π lm. The illuminance, a supplementary quantity, describes the luminance flux falling on a surface having unit lux or lm/m^2. The conversion between the photometric and radiometric quantities is given by the spectral sensitivity function V(λ) CIE 1931 defined and tabulated by Commission Internationale de l'Eclairage (CIE), as shown in Figure 2.2. The function peaks at 555 nm. At this wavelength it has a maximum efficacy of 683 lm/W and corresponds to the maximum spectral responsivity of the human eye [1].

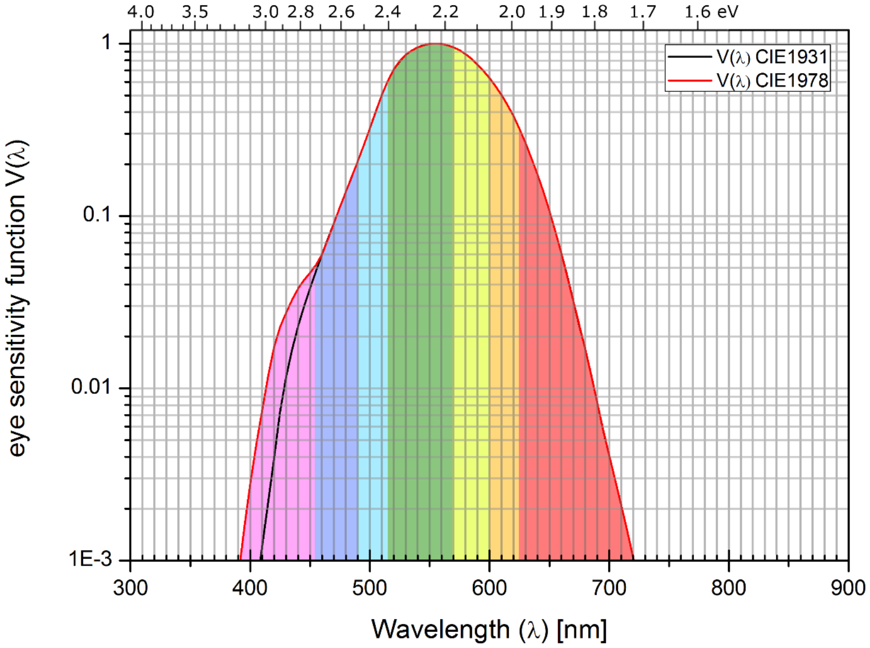

Figure 2.2: The spectral sensitivity functions V(λ) for the average responsiveness of human vision, CIE1931 and CIE1978 [1].

In 1978 the spectral sensitivity function, CIE 1978, was introduced to correct the underestimation of the human eye sensitivity below the spectral region of 460 nm. The CIE1931 spectral function is however still the standard today [2]. An overview of the radiometric quantities and corresponding photometric quantities is given in Table 2.1.

Table 2.1: Radiometric and photometric quantities and their dimensions.

Radiometric quantity	**Unit**	**Photometric quantity**	**Unit**
Radiant flux	W	Luminous flux	lm
Radiant intensity	$\frac{\mathrm{W}}{\mathrm{sr}}$	Luminous intensity	$\frac{\mathrm{lm}}{\mathrm{sr}} = \mathrm{cd}$
Irradiance	$\frac{\mathrm{W}}{\mathrm{m}^2}$	Illuminance	$\frac{\mathrm{lm}}{\mathrm{m}^2} = \mathrm{lux}$
Radiance	$\frac{\mathrm{W}}{\mathrm{sr.\,m}^2}$	Luminance	$\frac{\mathrm{lm}}{\mathrm{sr.\,m}^2} = \frac{\mathrm{cd}}{\mathrm{m}^2}$

For monochromatic light ($\Delta\lambda \rightarrow 0$) the conversion between radiometric and photometric quantities is fairly simple:

$$\text{Photometric unit} = \text{Radiometric unit} \cdot K_m \cdot V(\lambda) \qquad (2.1)$$

Where K_m: 683 lm/W is the maximum sensitivity and $V(\lambda)$ is the spectral sensitivity function.

Two laser pointers, A & B, with an equal beam diameter, an equal radiant flux (P) of 5 mW and a wavelength of λ_A=670 nm and λ_B=635 nm, respectively, will have a luminous flux (Φ):

Luminous flux Laser A: $\Phi_A = 0.005\,W \times 638\,\frac{lm}{W} \times 0.032 = 0.11\,lm$

Luminous flux Laser B: $\Phi_B = 0.005\,W \times 638\,\frac{lm}{W} \times 0.217 = 0.74\,lm$

Although having the same radiant flux, laser B will create a spot almost 7 times brighter than laser A [1].

For a non-monochromatic light source, such as the OLEDs in this thesis, the conversion from radiometric to photometric units becomes a bit more complicated, e.g.: the radiant flux to luminous flux conversion becomes:

$$\Phi = K_m \int_{\lambda} V(\lambda) \cdot P(\lambda) \cdot d\lambda \qquad (2.2)$$

Where Φ is the luminous flux (lm), K_m: 683 lm/W is the maximum sensitivity, $V(\lambda)$ is the spectral sensitivity function and $P(\lambda)$ is the radiant power (W).

The perception of colours arises from cone-like cells in the retina of the human eye. Colorimetry is standardised in a similar manner by the CIE. It is based on three standardised and equal weighted colour excitation functions, [X], [Y], [Z], of the CIE standard reference observer. Any colour can be represented by these functions. A more extensive treatment of light and its colour can be found in [1] but falls out of the scope of this thesis.

2.2 Characterization of OLEDs

OLEDs are complex optical cavities and their emission properties can strongly depend on the view angle [3]. As previously, discussed, in section 1.4, the typical OLED device architecture comprises of both organic and inorganic layers, each layer with its specific optical properties. Each layer has its own absorption and transmission coefficients and index of refraction, hereby forming weak microcavities [4]. Photons are emitted in random directions from the emissive layer of the OLED. Each layer introduces significant interference effects with a strong influence on the emission spectrum, shape and device efficacy. Therefore, the emission profile is severely modified and strongly deviates from the often assumed Lambertian profile [5]. The Lambertian emission profile has equal radiance into any solid angle within the forward viewing hemisphere and the intensity distribution follows a cosine fall-off [3]. For conventional OLEDs only 20% of the generated photons are emitted through the substrate as useful light [6]. A commonly used photometric efficacy to compare OLEDs performances is luminance efficiency, expressed in candela-per-ampere (cd/A) and defined as the ratio of the luminous intensity and the electrical current of the OLED. However this method implicitly assumes that the emission pattern of the OLED measured is Lambertian because the photon flux is only measured perpendicular to the emitting surface and considered equal everywhere else in the forward hemisphere. This measurement, however simple, is vulnerable to large inaccuracies and is therefore maybe only useful for the characterisation of OLEDs performance in display applications [3]. The most important photometric efficacy is the luminous power efficacy (η_p). It is defined as the ratio between the total luminous flux and the electric power of the OLED:

$$\eta_p = \frac{\Phi_{total}}{I \cdot V} \tag{2.3}$$

$$\text{where: } \Phi_{total} = \int_0^\infty K(\lambda) \cdot P_{OLED}(\lambda) \cdot d\lambda \tag{2.4}$$

$$\text{and: } \mathrm{K}(\lambda) = 683 \cdot V(\lambda) \tag{2.5}$$

The luminous power efficacy is expressed in lumen/Watt. The total luminous flux is measured using an integrating sphere coupled to a spectrometer with an optical fibre cable. The electrical characteristics of the OLED are commonly measured by a source-meter, which acts as voltage source and current meter.

Our measurement setup is, as illustrated in Figure 2.3, designed to assess the performance of OLEDs by measuring the luminous power efficacy, in accordance with S. R. Forrest, et. al. [3].

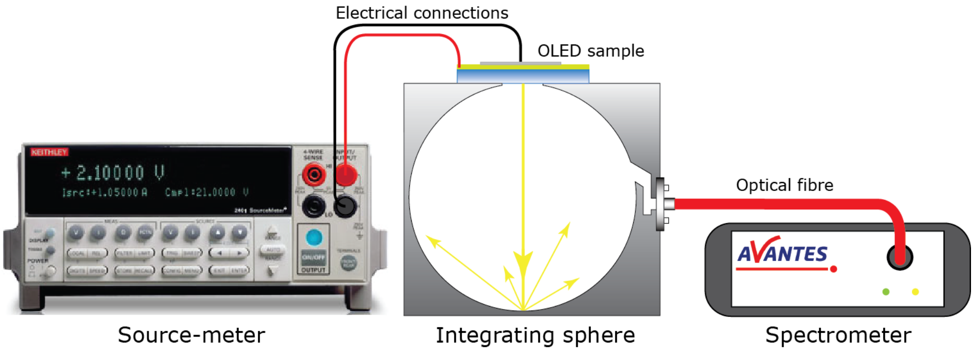

Figure 2.3: Measurement setup – including an integrating sphere connected to a spectrometer via an optical fibre cable – to determine OLED luminous efficacy.

The OLED is placed on top of the integrating sphere centred on the sample port. This is accomplished by using a purpose built sample holder and guiding system. Hereby, the photons emerging from the edge of the substrate due to substrate waveguiding are automatically excluded from the measurement. The measurement system, apart for the computer, is kept in a nitrogen (N_2) inert atmosphere glovebox. The integrating sphere, fibre optic cable and spectrometer are calibrated together as a whole to measure absolute values for radiometric, photometric and colorimetric parameters over all wavelengths from 200nm to 1100nm. The integrating sphere spatially integrates the radiant flux passing through its sample port and will capture all photons emitted by the OLED in the forward viewing hemisphere independent of the angle of emission. The captured radiant flux is measured in power per wavelength interval as function of wavelength by the spectrometer. The spectrometer software, driving the spectrometer, calculates the photometric and colorimetric values. The software driven source-meter performs a user-adjustable, bias-voltage sweep and reports the OLEDs current response. Furthermore, the total luminous flux (Φ_{total}) of the generated light by the OLED is recorded simultaneously. The corresponding measurement is called current – voltage – luminous flux (I-V-L) characteristic, as shown for a typical OLED in Figure 2.4.

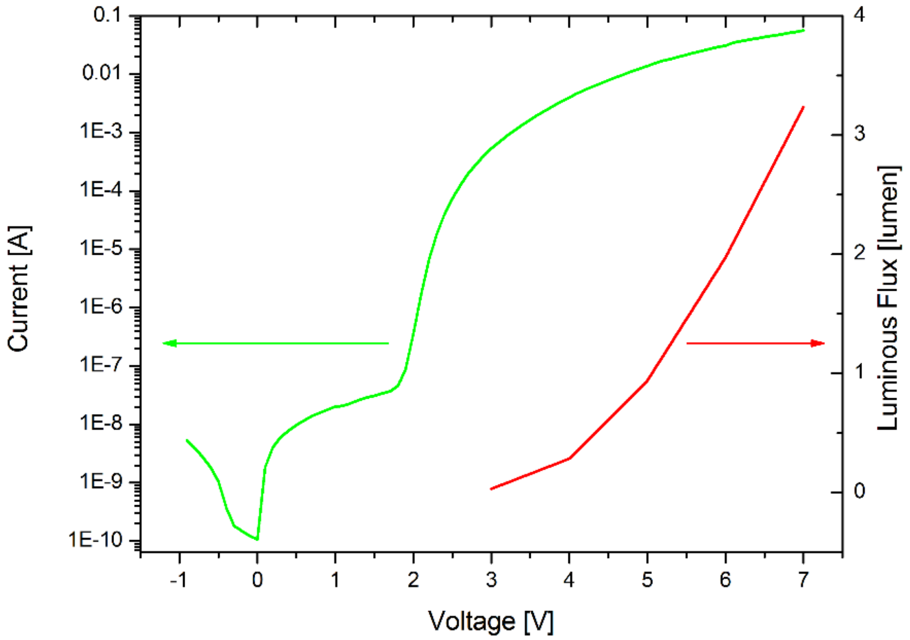

Figure 2.4: Current – Voltage – Luminous Flux (I – V – L) characteristic of a typical OLED.

Typically, the bias-voltage is varied from -1 V to 7 V in step sizes of 0.1 V. A delay of 250 ms is implemented between the voltage steps and subsequent current measurements to avoid incorrect current readings due to capacitive effects and joule heating. Synchronously during the bias-voltage sweep, the sweep is paused to measure the radiometric, photometric and colorimetric parameters of the light produced by the OLED. Typically, these measurements are started just beyond the built-in potential (V_{bi}), i.e. where the I-V characteristic has a sharp increase. From these measurements the luminous power efficacy of the OLED can easily be calculated by dividing the measured total luminous flux by the product of the corresponding bias-voltage and current.

2.3 Sheet-Resistance measurements

In organic electronic applications the materials are often used in a thin film configuration as part of the device architecture. Therefore, the sheet resistance (R_S) is often provided as a material property in contrast to the bulk resistivity (ρ) of the material. Although the sheet resistance is not an intrinsic material property, it is however a useful concept to assess the in-plane electrical properties of (organic) thin films. The reason is that the bulk resistance (R) of a material is dependent on the three dimensional shape of the sample. The sheet resistance however is independent of the samples dimensions. The sheet resistance of an Indium Tin Oxide (ITO) 1 inch by 1 inch layer is the same as an ITO 1 cm by 1cm layer. The resistance (R) of a conductor is given by:

$$R = \rho \frac{L}{W.t} = \frac{\rho}{t}\frac{L}{W}\ [\Omega] \tag{2.6}$$

With ρ the materials resistivity [Ω·m] and L, W, t, the dimensions of the sample as depicted in Figure 2.5.

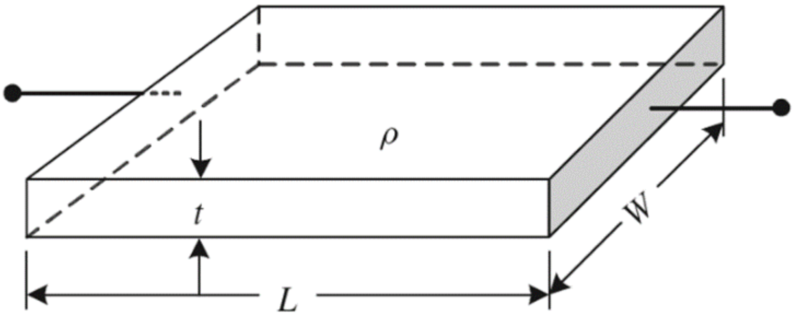

Figure 2.5: Sample shape.

The sheet resistance (R_S) is than given by:

$$R_S = \frac{\rho}{t}\ [\Omega/\ \mathrm{Square}] \tag{2.7}$$

The resistivity is normalized by the parameter t, the thickness of the layer. To be able to distinguish between R and R_S, the sheet resistance is given the unit ohms per square.

The Van Der Pauw measurement technique allows the determination of the sheet resistance of an arbitrary shaped uniform layer [7], as depicted in Figure 2.6. The contacts should be on the periphery of the sample and should be significant small.

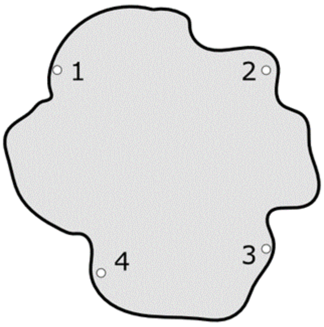

Figure 2.6: Arbitrary shaped thin film.

The thin film should have uniform thickness and should be one enclosed shape without isolated holes [8]. The Van Der Pauw method is based on the measurements of two resistances, R_A and R_B.

$$R_A = \frac{R_{12} + R_{21} + R_{34} + R_{43}}{4} \tag{2.8}$$

$$R_B = \frac{R_{23} + R_{32} + R_{41} + R_{14}}{4} \tag{2.9}$$

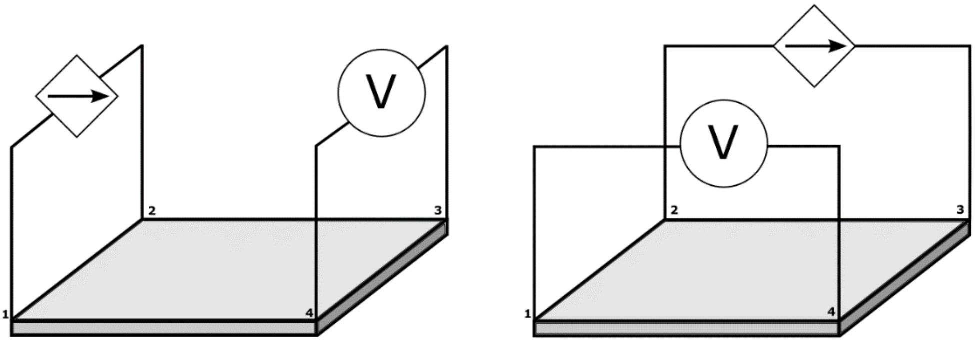

Figure 2.7: Principle of the Van Der Pauw measurement adapted from [8].

The values of the resistances R_{ij} are found by applying Ohms law. The resistance R_A is the average of the resistances R_{ij} along the vertical edge of the sample while R_B is obtained by calculating the average of the resistances R_{ij} along the horizontal edge of the sample as shown in Figure 2.7. The indexes i and j denote the current injecting contacts, such that e.g.:

$$\mathrm{R}_{21} = {}^{U_{34}}/_{I_{21}} \tag{2.10}$$

According to the Van Der Pauw theory [7], the sheet resistance (R_S) can be found by solving the following equation:

$$e^{\frac{-\pi R_A}{R_S}} + e^{\frac{-\pi R_B}{R_S}} = 1 \tag{2.11}$$

Rewriting this equation, leads to [7]:

$$\frac{1}{R_S} = \frac{\pi}{\ln(2)} \frac{R_A + R_B}{2} f\left(\frac{R_A}{R_B}\right) \tag{2.12}$$

Where f, as shown in Figure 2.8, is function of the ratio R_A/R_B:

$$\frac{R_A - R_B}{R_A + R_B} = farccos\left\{\frac{e^{\frac{\ln(2)}{f}}}{2}\right\} \tag{2.13}$$

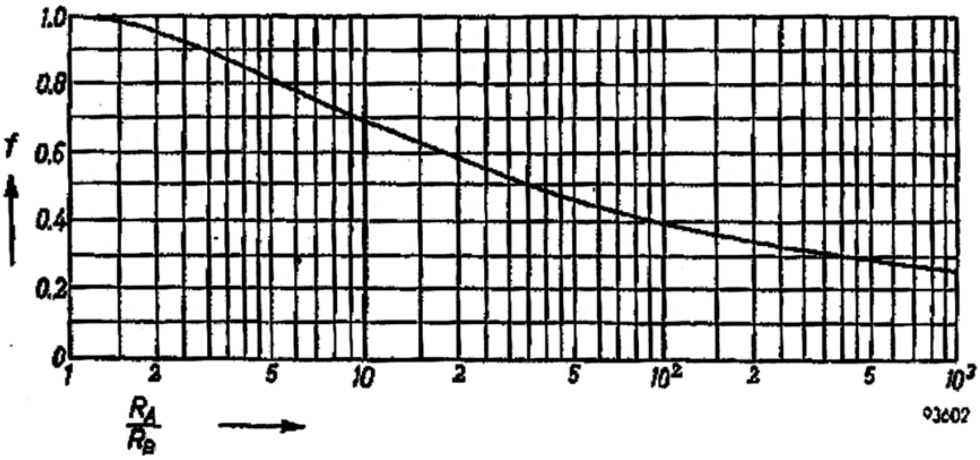

Figure 2.8: The correction factor f as function of R_A/R_B adapted from [7].

When R_A and R_B are almost equal, f can be approximated by 1 and the sheet resistance can be calculated according the following equation:

$$\frac{1}{R_S} = \frac{\pi}{\ln(2)}\frac{R_A + R_B}{2} \tag{2.14}$$

The practical implementation of the measurement setup, as depicted in Figure 2.9, has been built for the purpose of this thesis, around a switching matrix which allows the connection of the voltage meter and the controllable current source to appropriate sample corners according to 8 configurations needed to calculate R_A and R_B. The switching matrix, current source and voltage meter are controlled by software to set the correct switching sequence, apply the predefined current and measure the voltages.

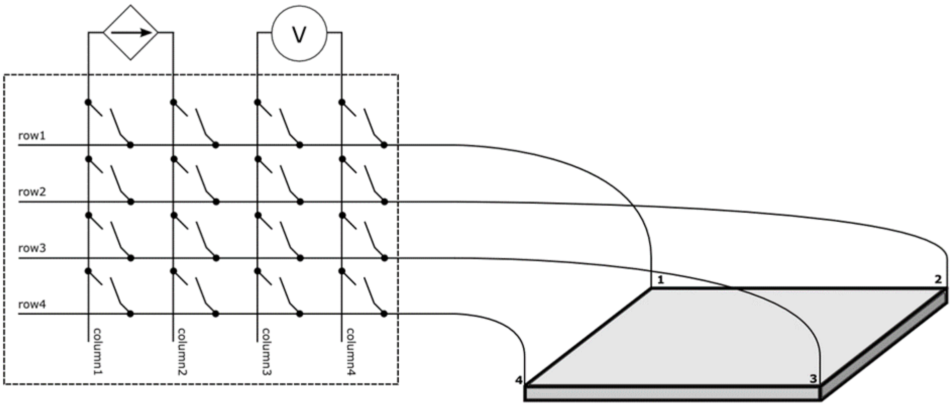

Figure 2.9: The Van Der Pauw measurement setup.

From the applied current and measured voltages, the values of R_A and R_B are calculated. From the calculated R_A and R_B values the sheet resistance is determined according to the ASTM F76 - 08 standard. This standard suggests the use of the Newton-Raphson (NR) numerical method to calculate the value of the sheet resistance (R_S). The Newton-Raphson method is an iterative algorithm that finishes when the convergence criterion (δ) is met. The first step in this process is to calculate an initial value for R_S denoted as Z_0.

$$Z_0 = \frac{2\ln(2)}{\pi(R_A + R_B)} \tag{2.15}$$

The second step is to calculate:

$$Z_n = Z_{n-1} - \frac{1 - y_n}{\frac{d(1 - y_n)}{dZ_{n-1}}} \tag{2.16}$$

$$y_n = \frac{1}{e^{(\pi . Z_{n-1} . R_A)}} + \frac{1}{e^{(\pi . Z_{n-1} . R_B)}} \tag{2.17}$$

$$\text{With: } n = 1,2,3,4, \ldots$$

The second step is repeated (n times) until:

$$\frac{Z_n - Z_{n-1}}{Z_n} < \delta \tag{2.18}$$

The sheet resistance R_S can be calculated by:

$$R_s = \frac{1}{Z_n} \tag{2.19}$$

In terms of the numerical model, the root of the equation $f(R_s)=0$ is computed by setting $f(R_S) = 1 - y_n$ and Z_0 as the first approximation of the root.

2.4 Atomic Force Microscopy

Atomic force microscopy (AFM) is a surface imaging technique to visualize a surface in 3D at the nanometer (10^{-9} m) scale. It was invented in 1986 by G. Bigging and co-workers and the technique combines the principles of the scanning tunneling microscopy (STM) and the stylus profilometer [9]. AFM can image all materials irrespective of their transparency or conductivity and can be applied in almost any environment e.g.: air, inert atmosphere, liquid and vacuum. Each pixel in the 2D array of the image is a measure of the surface height thus obtaining an image of the surface topography, as exemplified in Figure 2.10.

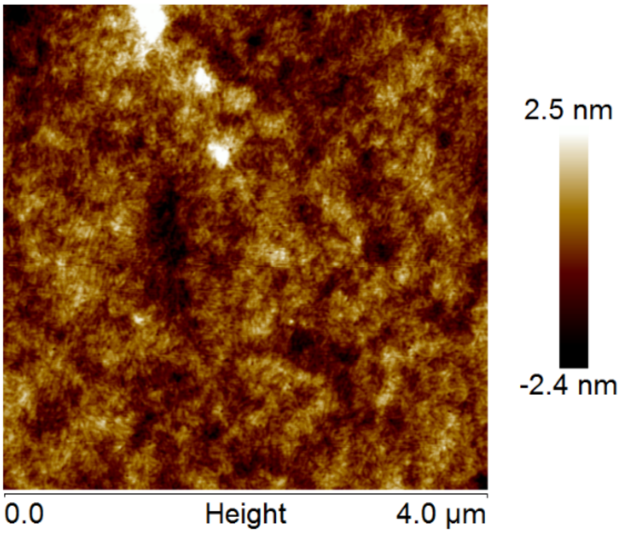

Figure 2.10: An inert-atmosphere topography image of a spin coated thin film of a phenyl-substituted poly(para- phenylene vinylene) co-polymer termed Super Yellow (SY).

The AFM tip, which is mounted at the end of a cantilever is the most essential part of the measurement system, it gives rise to the image, through its interaction force with the sample's surface. When the tip is brought close to the surface, forces between the surface and the tip lead to deflection of the cantilever. The three most common AFM modes together with the force regimes are shown in Figure 2.11.

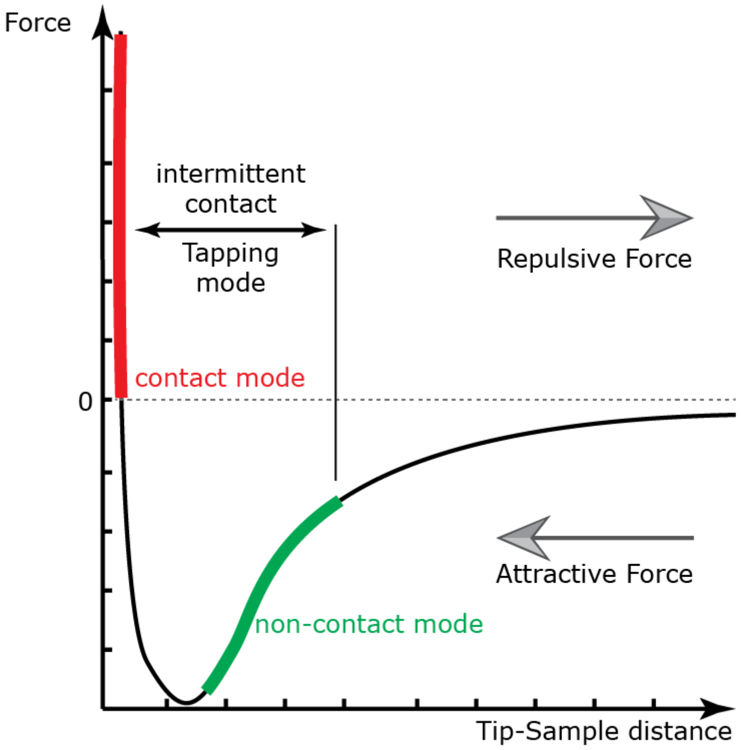

Figure 2.11: Graph illustrating the force regimes under which the AFM imaging modes, contact mode, intermittent contact or tapping mode and non-contact mode, are most commonly operated.

A multitude of forces do work on the cantilever but the most dominant one is the Van der Waals force [10]. The core components of the AFM are illustrated in Figure 2.12. As the tip of the AFM is moved closer to the surface of the sample the cantilever will deflect towards the surface by the attractive force between the surface and cantilever. As the cantilever is brought even closer towards the surface, in contact mode, repulsion forces will cause the cantilever to deflect away from the surface. This deflection of the cantilever is mostly tracked by optical techniques. A laser beam is focussed on the cantilever and used to detect deflections towards or away from the samples surface. This is achieved by a position-sensitive photodiode (PSPD) which is placed in the reflection path of the laser beam on the cantilever. Therefore any deflection of the cantilever will subsequently change the position of the laser beam spot on the PSPD.

Piezoelectric ceramic transducers are used to accurately position the tip (z-piezo) and the position of the sample (xy-stage). Making use of a feedback loop to accurately control the height of the AFM tip above the surface of the sample, while scanning, will reveal any topographical features as the position of the laser beam spot is maintained at the centre of the PSPD. The recorded movement of the cantilever is then translated in a spatially resolved topographic map of the surface of the sample.

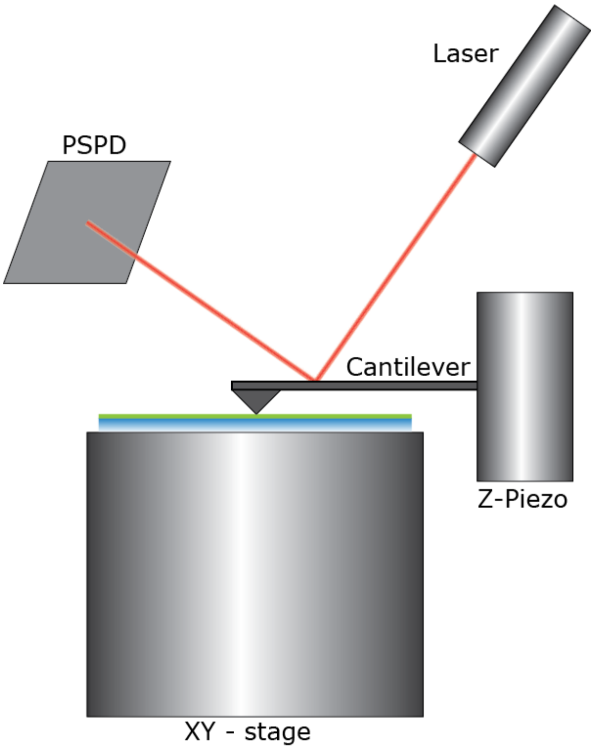

Figure 2.12: Illustration of the core components of the AFM: the cantilever and tip, the sample stage, the Z-piezo, the laser and the position sensitive photodiode (PSPD).

As already depicted in Figure 2.11, there are three different modes in which samples can be measured [11]. In contact mode the tip makes soft contact with the sample and the image contrast depends on the applied force of the cantilever, ranging from µN to nN. Due the contact of the tip with the surface while scanning, shear forces can be generated, causing damage to both the tip and the sample. In non-contact mode the tip-to-surface distance is in the order of 1 nm to 10 nm. This is the most suitable mode for measuring soft and elastic materials. In tapping (intermittent) mode the tip is oscillated with a frequency which is a bit lower than the resonance frequency of the cantilever. Because this mode extends from the repulsive regime into the attraction regime the tip intermittently taps the surface.

2.5 Scanning Electron Microscopy

Scanning electron microscopy (SEM) allows the observation and characterisation of organic and inorganic materials on a nanometre scale [12]. With SEM microscopy it is possible to obtain three-dimensional images of the surfaces of a wide variety of materials. This is achieved by irradiation of the sample with a finely focussed electron beam, with an energy ranging from 1 keV to 40 keV which is swept in a matrix across the surface [13]. As the electron beam hits the surface of the sample several processes occur: backscattering electron, secondary electron, auger electron, x-ray and light emission. Secondary electron and backscattered electron emission are the most useful to form the SEM images as they vary primarily due to differences in the surface topography. By correlation of the intensity of the emissions and the position of the scanner an image of the surface can be formed. These measurements are conducted in vacuum conditions. Therefore, the sample must be conductive enough to exclude surface charging and drift of the electron beam.

2.6 OLED preparation

2.6.1 Solution preparation

All OLEDs emissive layers prepared within this thesis are based on the, commercially available, phenyl-substituted poly(para- phenylene vinylene) co-polymer termed Super Yellow (SY). Its molecular structure is depicted in Figure 2.13 [14]. A certain mass (x mg) of SY is dissolved in a certain volume (y ml) and type of organic solvent, dependent on the deposition technique used and the required final film thickness. All concentrations are expressed as a mass volume ratio, e.g.: 5 mg/ml SY in chlorobenzene. The mass of the polymer was weighted on a microbalance and the volume of organic solvent was accurately controlled by a micropipette. The organic solvent was added to the polymer, contained in a darkened glass flask, and stirred overnight at 50 °C in an inert atmosphere (N_2) glovebox.

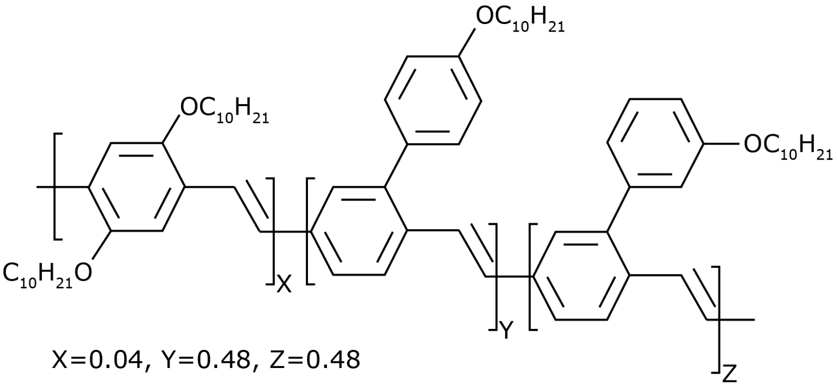

Figure 2.13: Molecular structure of Super Yellow [14].

2.6.2 Substrate preparation

The glass substrates are as purchased, from Kintec, pre-patterned with a 100 nm layer of ITO with a sheet resistance of 20 Ω/sq. A digital photograph and the substrate dimensions are shown in Figure 2.14. The substrate has 4 distinct islands of ITO to yield four OLEDs per substrate.

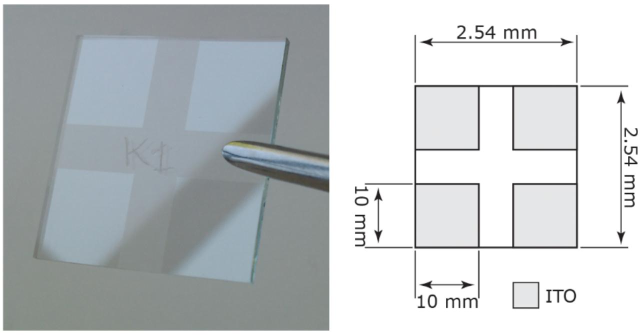

Figure 2.14: (left) Digital photo of ITO coated glass substrate. (right) Substrate dimensions.

The substrates are, before the OLED preparation starts, always exposed to a thorough cleaning procedure, which consists out of several sequential steps:

- Manually rinsing the substrate using a soap solution,
- 30 min in an ultrasonic bath submerged in this soap solution,
- 2 x 10 min in an ultrasonic bath submerged in demineralized water,
- 10 min in an ultrasonic bath submerged in acetone,
- 10 min submerged in boiling isopropanol,
- Drying in a high pressure N_2 flow,
- 15 min of UV/O_3 treatment.

2.6.3 Device construction

Spin coating is a process where a solution is applied to a horizontal rotating substrate, leaving a solid or wet planar film as a result of ejection of the solution and evaporation of the solvent. The substrate is held in place by the vacuum orifice, which is located in centre of the substrate holder. The acceleration and the end velocity are user adjustable as well as the spin time and are important parameters for the layer thickness. Depending on the spin coating parameters and the material solution used a post deposition thermal treatment is needed. An alternative thermal treatment is investigated in chapter 4 and an alternative thin film deposition technique is evaluated in chapter 5.

On top of cleaned ITO substrates a thin layer of PEDOT:PSS (30 nm) deposited by spin coating in ambient conditions is prepared using the following parameters:

Table 2.2: Spin coating parameters of a PEDOT:PSS film.

Speed (RPM)	3500
Acceleration (RPM/s)	1100
Time (s)	40

After the deposition, the samples are annealed in inert atmosphere using a hotplate at 120 °C for 10 min. After the samples have cooled down to room temperature the SY layer (80 nm) is deposited by spin coating in inert atmosphere using the following parameters:

Table 2.3: Spin coating parameters of a SY film.

Speed (RPM)	1000
Acceleration (RPM/s)	500
Time (s)	60

Hereafter, the metal cathodes are deposited, Ca (30 nm) and Al (80 nm), by thermal evaporation at a pressure of $1x10^{-7}$ mbar in the same inert atmosphere glovebox. In the thermal evaporation process, the metal, supplied in the form pellets, is heated through joule heating in a high vacuum to temperatures at which strong evaporation occurs. The samples are placed in a rotating sample holder above the evaporating metal so that it is distributed uniformly. On collision of the evaporating beam with the surface of the samples, the atoms condense on the surface to from a film. The speed of evaporation is dependent on the temperature of the system, which in turn is dependent on the joule heating of a direct current (DC) flowing through the metal and its metal container inside the vacuum. The mean free path (λ_m) of the evaporated metal atoms dependents on the vacuum strength, the lower the pressure the larger the λ_m [15].

2.7 References

[1] M. Bukshtab, *Applied Photometry, Radiometry and Measurements of Optical Losses*, 1st ed. Springer Science, 2012.

[2] M. D. Fairchild, "The Cie 1931 Standard Colorimetric Observer - Mandatory Retirement at Age 65," *Color Res. Appl.*, vol. 18, no. 2, pp. 129–134, 1993.

[3] S. R. Forrest, D. D. C. Bradley, and M. E. Thompson, "Measuring the Efficiency of Organic Light-Emitting Devices**," *Adv. Mater.*, vol. 15, no. 13, pp. 1043–1048, Jul. 2003.

[4] V. Bulović, V. Khalfin, G. Gu, P. Burrows, D. Garbuzov, and S. Forrest, "Weak microcavity effects in organic light-emitting devices," *Phys. Rev. B*, vol. 58, no. 7, pp. 3730–3740, 1998.

[5] O. W. Members, "OLLA White Paper on the Necessity of Luminous Efficacy Measurement Standardisation of OLED Light Sources," *OLLA open access*, no. IST-004607, p. 10, 2007.

[6] B. Riedel, J. Hauss, U. Geyer, J. Guetlein, U. Lemmer, and M. Gerken, "Enhancing outcoupling efficiency of indium-tin-oxide-free organic light-emitting diodes via nanostructured high index layers," *Appl. Phys. Lett.*, vol. 96, no. 24, p. 243302, 2010.

[7] L. J. Van Der Pauw, "A method of measuring specific resistivity and hall effect of discs of arbitrary shape," *Philips Res. Reports*, vol. 13, no. 1, pp. 1–9, 1958.

[8] H. Czichos, T. Saito, and L. E. Smith, "Electrical Properties," in *SPRINGER HANDBOOK OF MATERIALS MEASUREMENT METHODS*, Springer US, 2006, pp. 431–484.

[9] G. Binnig and C. F. Quate, "Atomic Force Microscope," *Phys. Rev. Lett.*, vol. 56, no. 9, pp. 930–933, 1986.

[10] G. Haugstad, *Atomic Force Microscopy: Understanding Basic Modes and Advanced Applications*. Wiley Publishing, Inc., 2012.

[11] a Karbach and D. Drechsler, "Atomic force microscopy - A powerful tool for industrial applications," *Surf. Interface Anal.*, vol. 27, no. 5–6, pp. 401–409, 1999.

[12] A. Khursheed, *Scanning Electron Microscope Optics and Spectrometers*. World Scientific, 2010.

[13] D. C. Joy, "The theory and practice of high-resolution scanning electron microscopy," *Ultramicroscopy*, vol. 37, no. 1–4, pp. 216–233, 1991.

[14] M. a. Summers, S. K. Buratto, and L. Edman, "Morphology and environment-dependent fluorescence in blends containing a phenylenevinylene-conjugated polymer," *Thin Solid Films*, vol. 515, no. 23, pp. 8412–8418, Sep. 2007.

[15] Z. Guo and L. Tan, *Fundamentals and Applications of Nanomaterials*. Artech House, 2009.

Chapter 3 Build-in metal grid structures in Boron-doped Nano Crystalline Diamond as transparent anode for OLEDs

In this chapter we introduce and evaluate the use of transparent conductive boron-doped nano crystalline diamond (BNCD) thin films as alternative to indium tin oxide (ITO). An overview of transparent conductors is presented with emphasis on ITO and other alternative transparent anodes in OLEDs. The BNCD layer is embedded with a gold (Au) grid to tune the transparency and sheet resistance. These BNCD:Au-grid layers are used to fabricate highly functional OLEDs. These OLEDs constructed on BNCD:Au-grid layers, show higher hole-currents and enhanced luminance flux compared to the ITO reference device attributed to the better charge injection in the light-emitting layer by the anode. The BNCD is integrated with an embedded gold grid that allows efficient charge collections and scaling up strategies for large area electronics.

3.1 Transparent semiconductors

Transparent semiconductors, which have a high optical transparency for wavelengths from 390 nm to 700 nm and a high conductivity, are in high demand for many modern electronic applications. These applications include flat-screen displays based on liquid crystal display (LCD), plasma and OLED technology, photovoltaics, electrochromic windows, anti-static coatings, light filters, sensors, low-emissive windows and large-area solid state lighting (SSL).

Materials exhibiting both high optical transparency and high conductivity are however not common when considering conventional materials, such as metals, polymers and ceramics. The conductivity of materials is determined by the charge carrier density and the charge mobility. The transparency on the other hand is determined by the band gap of the material and the charge carrier density. The only way this has been achieved is by introducing the appropriate dopants in a wide band gap (> 3 eV) oxide [1]. The wide band gap makes them transparent for visible light, since the photon energy (1.8 eV – 3.0 eV) is less than the band gap. The heavily doping turns the transparent conducting oxide into a degenerate semiconductor [2].

The first thin film transparent semiconductor was discovered in 1907 by K. Bädeker. The thermally oxidized Cadmium (CdO) thin film, with a thickness of 106 nm, sputtered on glass had a conductivity (σ) of 870 S/cm and had a translucent orange colour [3]. Today however, the use of CdO is avoided due its toxicity. In the following decades, tin oxide (SnO_2) and Indium oxide (In_2O_3) were discovered and employed as transparent heating elements for aircraft windscreens [4]. Shortly thereafter, in 1951, the most important and widely used transparent conductor for optoelectronic applications was discovered, In_2O_3:Sn commonly known as indium-tin-oxide (ITO). Since their discovery, OLEDs based on small molecules [5] or conjugated polymers [6] have been using ITO as transparent anode. The use of ITO as transparent anode in OLEDs and alternative transparent anodes will be discussed in the next sections of this chapter. An extensive overview of transparent conductors can be found in [7], [8].

3.2 Indium Tin Oxide as anode in OLEDs

As anode, ITO is the most commonly used transparent conducting oxide for optoelectronic applications. It owes its wide applicability in state-of-art applications and research domains to its excellent physical properties. For OLEDs, its high work function of 4.7 eV [9] facilitates hole-injection and its good conductivity ($\sigma = 1 \times 10^4$ S/cm) allows a good charge distribution over a large area [10]. It combines these good electrical properties with a high optical transparency ($T > 85$ %) in the visible spectrum [10] and high morphological uniformity (low roughness, very thin layer and large area). The high transmission is needed to minimize losses due to internal photon absorption or reflection. The high morphological uniformity reduces the electrode resistance, avoids device short-circuits and reduces leakage currents. The high conductivity, transparency and uniform morphology of ITO films are conventionally achieved by physical vapour deposition (PVD) [7]. This deposition process, unfortunately, requires sophisticated vacuum equipment, which in turn increases the production cost. Therefore, in recent years, the development of a more cost-effective, low temperature, solution deposition process has been subject of intense research activities [10]–[13] . The advantage of solution processing is the ability to utilize large area printing techniques for the deposition of ITO. Currently, there are two solution processing methods for ITO thin film deposition, one based on a dispersion of nanoparticles [14] and the other based on the sol-gel process [15]. Current state-of-art ITO films deposited via solution processing of nanoparticles yields high transparent ($T = 93$ %) uniform thin films with a sheet resistance of 356 Ω/Square which is unfortunately too high to be used as anode for optoelectronics applications e.g.: OLEDs, but meets the requirement for touch screens [11]. The sol-gel solution deposition process however have recently yielded highly transparent ($T = 90.2$ %), highly conductive ($\sigma = 1.39 \times 10^3$ S/cm) uniform ITO film with a sheet resistance of 30 Ω/Square [10]. These properties achieved via the solution processing sol-gel deposition technique are within the same order of magnitude as for ITO films produced by the PVD technique and makes the sol-gel deposition technique a worthy competitor.

The use of ITO in OLEDs and more general in organic optoelectronics devices also has some deficiencies. Indium and tin diffuse into the organic layer [16] and cause sever luminance degradation and eventually cause device failure [17]. The poor mechanical stability of the ITO film limits the use of ITO in flexible devices [18]. Furthermore, the onset of thermal degradation is observed at a temperature of 250 °C, at which the in-plane resistivity starts to increase rapidly

[19]. The poor thermal conductivity of ITO, 10.2 W/m·K [20], will limit the lifetime of OLEDs as they are exposed to Joule heating [21][22].

Due to its wide applicability, more than 80 % of the indium demand worldwide ends up as a transparent ITO electrode in optoelectronic devices [23]. Indium is a scarce resource and is solely a by-product of conventional base metal mining like zinc, copper and tin. Indium is the most abundantly available in zinc deposits, the average indium content in one zinc deposit is 1/50 ppm [23]. Therefore, it is estimated that the average continental crustal abundance of indium is 50 mg/Ton rock. Between 2002 and 2008 the indium price increased an impressive 800 % from 85 $/Kg to 685 $/Kg and peaked in 2006 to almost 1000 $/Kg [24]. Currently, a great portion of the global indium demand is supplied from secondary recycled sources [23]. In addition, all indium compounds should be regarded as highly toxic as they are carcinogenic and damage the heart, kidneys and liver [25].

To address the above mentioned deficiencies with ITO as anode in OLEDs, its poor chemical stability, its low thermal stability and conductivity and the scarcity of indium, we investigate the feasibility of using boron doped nanocrystalline diamond infused with a metal grid as alternative anode in OLEDs. However, before discussing this, firstly an overview on alternative transparent anodes is given in the next section.

3.3 Alternative transparent anodes in OLEDs

The search for ITO alternatives for OLEDs increased parallel to the exponential growth of the flat-panel display industry, which started around 2005 [7]. However, at that point, ITO was still the best anode for OLEDs producible on a commercial scale and still is nowadays. Since 1907 a lot of new TCOs have been introduced, each with its specific advantages, physical properties and niche applications, as listed in Table 3.1.

Table 3.1: A selection of TCOs developed since 1907 [8]. The prefix 'a-' denotes the amorphous characteristic.

a-CdSnO	In_2O_3:Mo	SnO_2:F	ZnO:In
a-InGaZnO	In_2O_3:Sn	SnO_2:Sb	ZnO:Al
a-ZnSnO	In_2O_3:Ti	TiO_2:Nb	ZnO:F
Cd_2SnO_4	InGaZnO	$Zn_2In_2O_5$	ZnO:Ga
CdO	SnO_2:Cl	Zn_2SnO_4	$ZnSnO_3$

In the last decade, the amorphous TCOs gained more and more attention in the scientific and industrial community [26]. They have comparable electrical and optical properties to crystalline TCOs while being high temperature stable, mechanically flexible and solution processable at room temperature [8]. These properties are most favourable towards flexible applications on plastic substrates.

Due to the ever-increasing demand and price of indium a multitude of ITO-free alternative anodes have been developed over the past years. In the subcategory of metal grid alternatives such as, a micro-meter metal grid [27], a nanoimprinted metal grid [28] and even a solution processable irregular network of metal nano-wires [29] have been demonstrated as alternative anode in OLEDs. These metal grids generally improve the charge distribution throughout the device resulting in a more uniform light emission. This effect becomes more predominant as the active area of the OLED increases. Furthermore, the transmission and conductivity can easily be tuned by varying the line width and thickness of the metal grid as required by any specific application. The work function can also be changed, to some extent, by choosing a different metal to improve the compatibility with the active material. Apart from the metal-nanowire network most metal grids require additional processing steps such as lithography. Another subcategory of alternative anodes is that of carbon based materials. Here ITO replacements include carbon nanotube anodes [30], single and multi-layered graphene based anodes [31][32], conjugated polymers [33] and diamond [34]. The main advantage of carbon nanotube based anodes is their mechanical flexibility but they suffer from intrinsic problems as percolation, high contact resistance between the tubes and poor film uniformity [35]. Although graphene looks very promising as ITO replacement in OLEDs due to its excellent transmittance and low sheet resistance, the biggest disadvantage is that it has to be grown by chemical vapour deposition (CVD), delaminated and layer-transferred to the substrate of choice [36]. Conjugated polymers have been used in polymer OLEDs since their discovery. Only recent, the polymer PEDOT:PSS has been used as anode, as previously it was already used as hole-injection layer. Although, OLEDs with high-conductive PEDOT:PSS anodes show similar efficacies compared to ITO anode reference devices, its hygroscopic nature leads to long-term stability issues [37].

As these alternative anodes have been developed over the past decades, new advantages have unfolded e.g.: solution and room temperature processing, low material cost, mechanical flexibility, indium free. And even as some alternatives match or even surpass ITO in terms of higher transmittance and lower sheet resistance, they still have to demonstrate their applicability in a large scale and cost effective production process.

In this chapter, the use of BNCD as alternative anode in OLEDs is explored. It has some superior properties over other anode materials: its high thermal stability and thermal conductivity and last but not least its high chemical stability [38] [39]. Furthermore, it has a wide optical transparency from UV to IR [40] and large area deposition is also possible by the microwave plasma enhanced CVD process [41] allowing upscaling of our organic optoelectronic devices.

3.4 Anode preparation

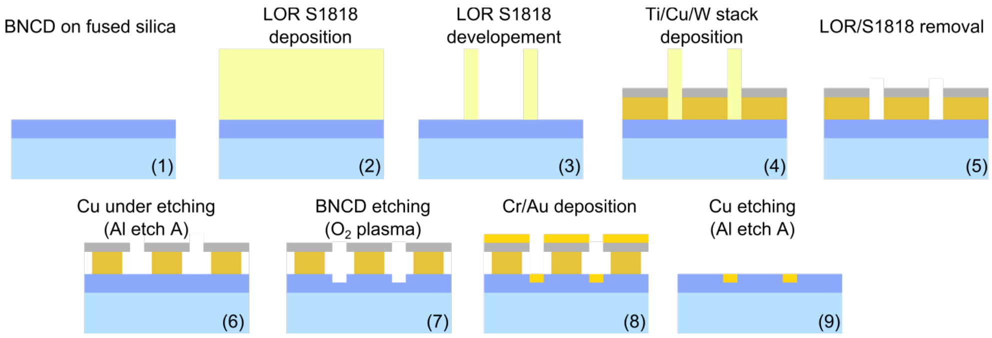

Figure 3.1: BNCD:au grid anode fabrication process.

First, a BNCD layer, 80 nm, is grown on a cleaned fused silica substrate (Figure 3.1 (1)) using a microwave plasma enhanced CVD system. The typical growth time was 2 hours. To embed the Cr/Au grid in the diamond, the grid pattern should be etched in the solid BNCD layer. In a first step, a polymer stencil of the grid structure was patterned by photolithography using LOR3B-S1818 photoresist (Figure 3.1 (2-3)). Next, a sputtered metal stack, consisting out of a carbide forming titanium (Ti) adhesion layer (20 nm), a sacrificial copper (Cu) layer (400 nm) and an oxygen-plasma protecting Tungsten (W) layer (100 nm) (Figure 3.1(4)), was deposited on the patterned BNCD surface. The adhesion-, sacrificial- and oxygen-plasma protection materials were chosen in such a way that the wet etching of the sacrificial layer does not influence the morphology of the oxygen-plasma protection layer. After removal of the photoresist (Figure 3.1(5)), the sacrificial Cu-layer was etched in order to increase the aspect ratio, use of Al etch A, in order to create a lift-off structure (Figure 3.1(6)). The final grid pattern was etched in the BNCD layer by the use of an oxygen plasma (Figure 3.1(7)). After these two etching steps, the etched grid pattern was filled with Cr/Au by thermal evaporation (Figure 3.1(8)). The protective metal stack Ti/Cu/W with Cr/Au on top was removed by etching away the Ti/Cu/W layers leaving the chromium/gold layer embedded in the BNCD layer as the end result (Figure 3.1(9)). The resulting fused silica substrate with BNCD:Au-grid anode on top is highly transparent as shown in Figure 3.2(a). The embedded Cr/Au grid-lines have a thickness of 50 nm and are 4 µm in width. The grid-line space optimum is 36 µm as will be discussed below. For easy comparison, the layout of these BNCD:Au-grid samples is exactly the same as our ITO anode reference devices, as shown in section 6.3 of chapter 2.

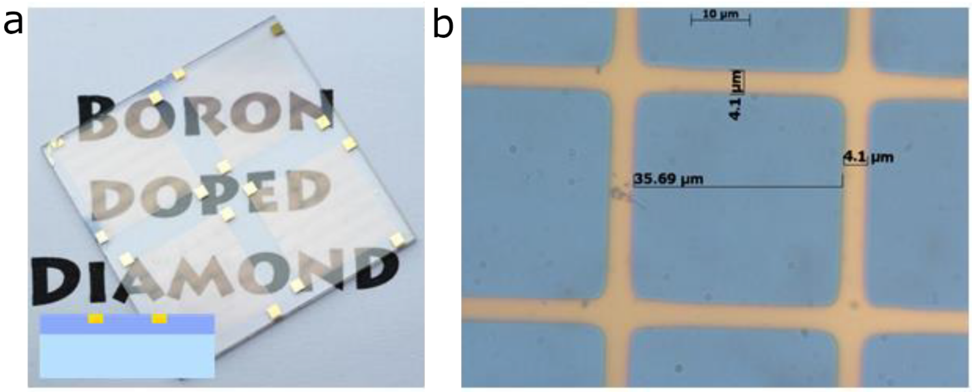

Figure 3.2: Photograph of the Cr/Au grid imbedded in the BNCD layer. The inset shows the schematic cross section of the electrode with the fused silica substrate (light blue), BNCD layer (dark blue) and integrated gold grid (orange). b) Optical microscopy picture

3.5 Transmission and conductivity

The transmission of the BNCD:Au-grid anode depends on both, the transparency of the BNCD and the relative line thickness of the Cr/Au grid. Transmission measurements have been performed in function of relative line thickness as can be seen in Figure 3.3. The relative line thickness is the ratio of the grid line width to the sum of the grid spacing and grid line width.

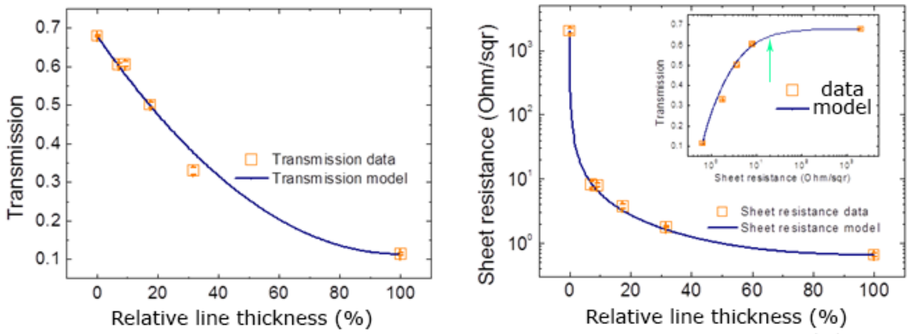

Figure 3.3: (left) Transmission in function of relative line thickness. (right) The sheet resistance in function of relative line thickness. Inset shows transmission in function of sheet resistance, the green arrow denotes the optimum.

For a squared grid the relation between the transparency of the grid and the line width is given by equation:

$$T(d) = \frac{T_{BNCD}(b-d)^2}{b^2} + \frac{T_{Au}(b^2-(b-d)^2)}{b^2} \tag{3.1}$$

Where b is the size of the unit cell and d is the size of the BNCD square in the gold square, T_{BNCD} is the transmission of a BNCD layer on top of a fused silica substrate and T_{Au} is the transmission of a Cr/Au layer on top of the fused silica substrate. The transparency of the BNCD is around 70% and that of the Cr/Au layer is around 10%. Increasing the grid-line thickness will evidently decrease the overall transmission.

Besides the transparency, also the resistivity of the anode material is a crucial parameter. A BNCD layer of 80nm, without an embedded grid, having a boron concentration of 5×10^{20} cm^{-3}, has a transparency of 80 % and a sheet resistance of 2000 Ω/Square. The sheet resistance (R_S) of the sample was obtained by using the Van Der Pauw method. The sheet resistance was modelled based on Ohm law:

$$\mathrm{R_s(d)} = \frac{\mathrm{R_S^{Au}(d^2.R_S^{BNCD} + d.b.R_S^{Au} - d^2.R_S^{BNCD} - d.b.R_S^{Au})}}{\mathrm{b(d.R_S^{BNCD} + b.R_S^{Au} - d.R_S^{Au})}} \qquad (3.2)$$

The value of R_s^{Au} and R_s^{BNCD} are the sheet resistances of, resp., the gold layer and the BNCD layer. Here, the size of the BNCD square (d) is used as fitting parameter. The calculated sheet resistance is a reasonably good fit of the measurement data.

From these measurements and taking the finite resolution of the mask aligner the into account, we determined the grid dimensions: a grid-line width of 4 µm and a grid spacing of 36 µm, as depicted in Figure 3.2. The resulting BNCD:Au-grid anode has a sheet resistance as low as 20 Ω/Square with a transmission of up to 70 %.

The transmission spectra of the transparent electrodes are given in Figure 3.4. For the ITO-electrode, 10 % of the transmitted light is lost. The transmission is diminished at energies above 3.5 eV, which corresponds to the UV-region of the spectrum. For the BNCD-layers on top of fused silica substrates, the transmission is comparable with that of ITO, although 30 % transmission loss in observed. However, at higher energies above 3.5 eV, there is no drop in transmission.

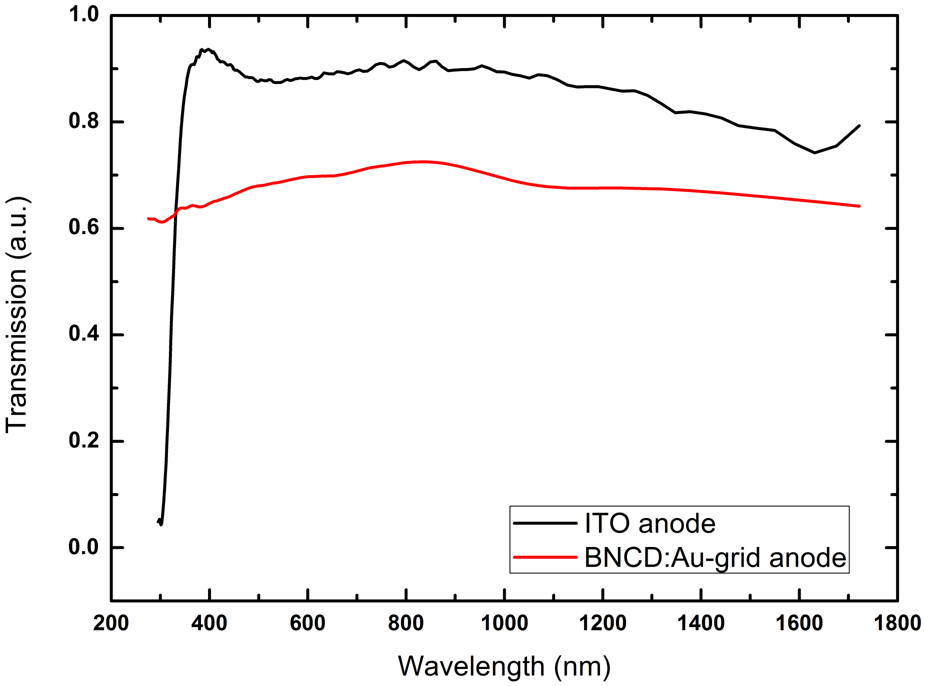

Figure 3.4: Transmission spectra of the transparent anodes.

At this stage in the anode development, a rectangular grid was chosen as proof-of-concept. Further improvements towards higher transmission can be obtained by optimizing the grid goniometry. Other grid goniometry's e.g.: hexagonal, spiral or leaf-like grids can improve the anodes transmission significantly [42].

Internal reflection and absorption of light in OLED devices is one of the most significant loss channels, about 82 % of the light gets trapped by induced surface plasmons and a mismatch between the refractive index of the different layers in the device [43]. The refractive index of a material has a real part, n and an imaginary part, k as shown for both anodes in Figure 3.5. The most significant difference, observed between the two electrodes, is in the real part (n) of the refractive index. For ITO, this part of the refractive index is low compared to BNCD layers. This part of the refractive index is responsible for the reflection of light at the interface between two substances according to Snell's law:

$$\frac{\sin(\theta_1)}{\sin(\theta_2)} = \frac{n_2}{n_1} \tag{3.3}$$

Here, n_1 and n_2 are the real parts of the refractive index of the material and the incident and refracted angles are denoted resp. θ_1, θ_2. Total internal reflection at the interface between two materials occur when the incident angle (θ_1) is greater than the critical angle (θ_c). The critical angle is found by setting the refracted angle θ_2 = 90° (parallel to the interface) and is given by the following equation:

$$\theta_c = \sin^{-1}\left(\frac{n_2}{n_1}\right) \tag{3.4}$$

Total internal reflection can therefore only occur when $n_1>n_2$, i.e. when light in material 1 encounters the interface with material 2 that has a lower index of refraction.

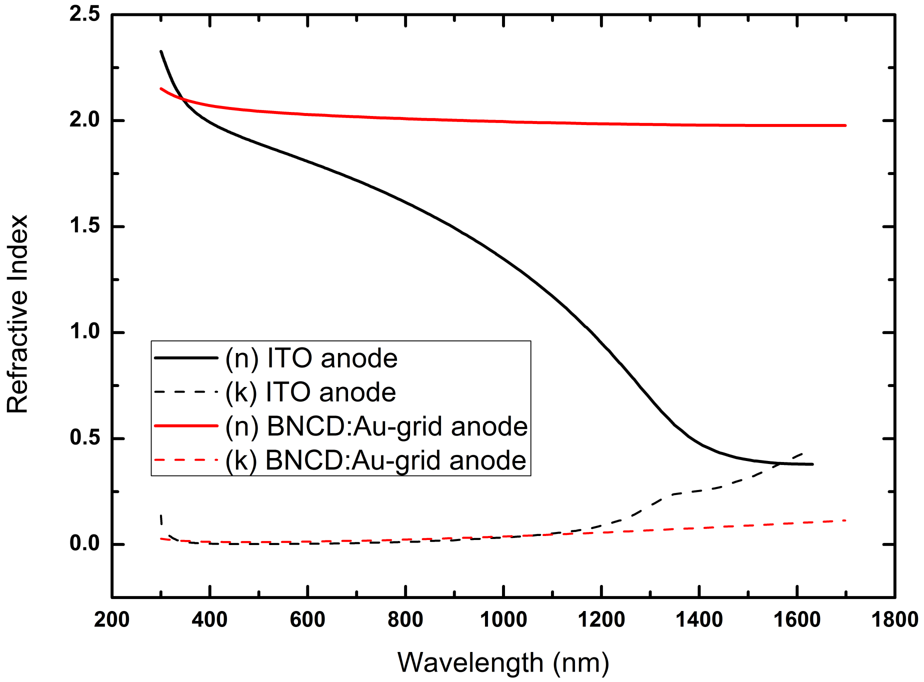

Figure 3.5: Real (n) and imaginary (k) part of the refractive index of both anodes.

The refraction n+ik is derived from the optical transmittance, reflectance and absorption measurements by photothermal deflection spectroscopy (PDS). For ITO, the real part of the refractive index at 2.25eV (550 nm) is around 1.84 and for BNCD deposited on fused silica the real part of the refractive index is 2.03. Due to the large difference of refractive indices of both anode and glass substrate combination with the refractive index of air (n_{AIR} = 1) both anodes will have comparable critical angles and light out-coupling efficiencies. The light out-coupling efficiency η for a point source is calculated as:

$$\eta = \frac{2\pi I_0 \int_0^{\theta_c} \sin\theta d\theta}{2\pi I_0 \int_0^{\frac{\pi}{2}} \sin\theta d\theta} = \frac{\cos\theta|_0^{\theta_c}}{1} \tag{3.5}$$

$$\eta = 1 - cos\theta_C = 1 - \sqrt{1 - sin^2\theta_C} \tag{3.6}$$

$$\eta = 1 - \sqrt{1 - \left(\frac{n_{air}}{n_{anode}}\right)^2} \tag{3.7}$$

$$\eta = 1 - \sqrt{1 - \frac{1}{{n_{anode}}^2}} \tag{3.8}$$

3.6 Morphology

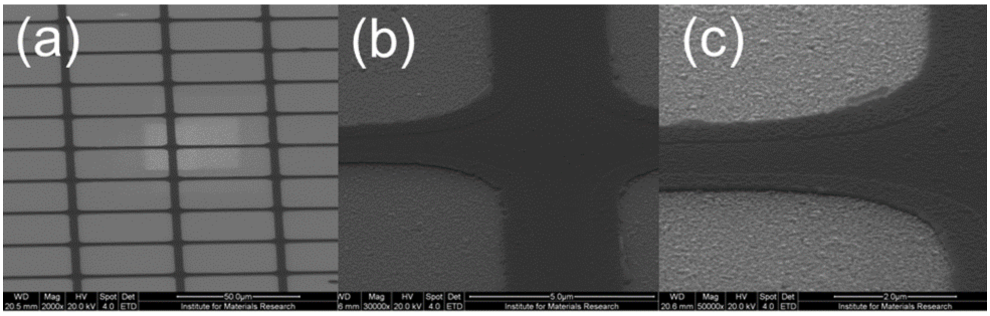

Figure 3.6: SEM images of the BNCD:Au-grid anode at different zoom levels (a) 50 µm, (b) 5 µm and (c) 2 µm.

SEM images in Figure 3.6 (a-c) show an image of the gold grid in the BNCD diamond. The gold grid, electron dense, is shown in black while the less electron dense BNCD layer is grey as is clearly seen in Figure 3.6 (a). The gold grid is homogeneously spread over the surface indicating the absence of cracks or line discontinuations. A zoom of this picture shows a small overlap between the diamond grid and the BNCD Figure 3.6 (b,c). This is necessary to get a good charge distribution (holes) throughout the anode.

3.7 BNCD:Au-grid anode OLEDs

Polymer OLEDs are constructed on the BNCD:Au-Grid anode, as shown in Figure 3.7, and compared to ITO anode reference devices. Both devices are identically constructed for accurate comparison, the processing parameters are outlined in detail in section 6 of chapter 2. Figure 3.7 also shows an optical microscopy image of a BNCD:Au-grid anode OLED at 3 V forward bias. The vertical and horizontal lines are the Cr/Au grid and the luminous squares are the BNCD layer. Here homogenous light distribution over the BNCD:Au-grid anode is observed.

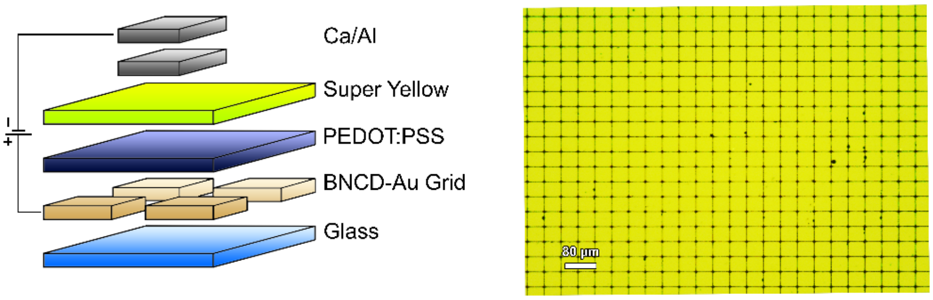

Figure 3.7: (left) The schematic layout of the OLEDs. (right) Optical microscope image of a BNCD:Au-grid anode device under operation.

The J-V characteristics of the OLEDs fabricated with an ITO and BNCD:Au-grid anode are shown in Figure 3.8. From linear fitting of the J-V characteristics the built-in potential (V_{BI}) values were determined, resulting in 1.76V for the BNCD:Au-grid PLEDs and 1.80V for the ITO PLEDs. A comparison of the J-V characteristics reveals that the BNCD:Au-grid anode OLEDs exhibit a leakage current density of ten times higher than the reference ITO anode OLEDs. Beyond the turn-on voltage, in the diffusion-dominated and drift-dominated regimes, the current density for the BNCD:Au-grid anode OLEDs is a factor two higher than for the ITO anode OLEDs.

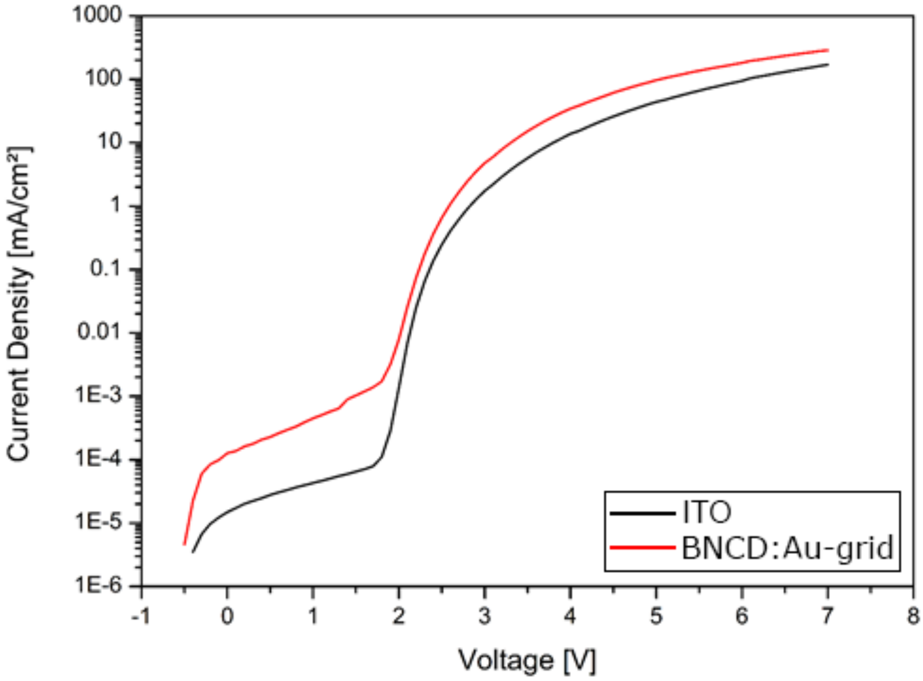

Figure 3.8: The current density vs voltage (J-V) characteristics, in semi-log plot, of ITO and BNCD:Au-grid anode OLEDs, with identical device structures PEDOT:PSS (35 nm)/ Super Yellow (80 nm)/ Ca (30 nm)/ Al (80 nm).

Apart from the hole-injecting anode, both device architectures remain identical. The hole-injection in OLEDs is not only dependent on the anode work function but also on the surface morphology and interfacial chemistry of the anode [44]. The work functions of the BNCD and Au-grid are resp. 4.96 eV and 4.92 eV, which is slightly higher than the work function of ITO, being 4.7 eV. However, the anodes are spatially and electrically separated from the active layer by a 35 nm PEDOT:PSS interlayer, which smoothens the anode/organic interface and facilitates hole injection. The turn-on voltage, as predicted by the Fowler-Nordheim tunnelling model [45], is very sensitive to the charge injection barrier height. The turn-on voltage shift of the BNCD:Au-grid anode OLEDs therefore suggest a lower injection barrier at the anode/interlayer interface. The electronic processes at the anode/interlayer and interlayer/active layer interface are currently still heavily debated [44].

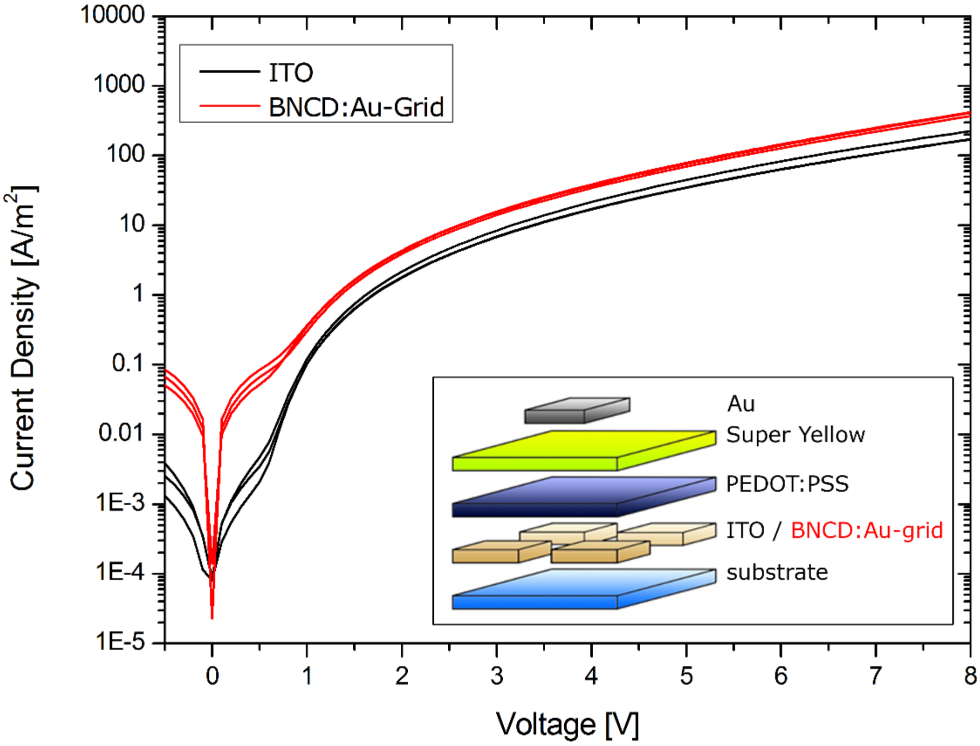

Figure 3.9: J-V characteristics, in semi-log plot, of ITO and BNCD:Au-grid anode hole-only OLEDs. The inset illustrates the (identical) device structures PEDOT:PSS (35 nm)/ Super Yellow (80 nm)/ Au (100 nm).

To further investigate the hole-injection properties of the BNCD:Au-grid anode, hole-only devices were constructed, as shown in the inset of Figure 3.9. Due to the high-energy barrier (ΔE = 1.9 eV) between the Au cathode (5.1 eV) and the LUMO of the Super Yellow (3.2 eV), any observed current could be exclusively attributed to holes flowing through the device, as electron injection is highly unlikely. From the JV characteristic, shown in Figure 3.9, it is clear that, for both devices, V_{BI} has shifted to around 0.5 V, which is closely related to the hole-injection barrier. Furthermore, at the same bias voltage, the current density is higher for the BNCD:Au-grid anode devices than for the ITO anode devices. At bias voltages below V_{BI}, J_{hole} of the BNCD:Au-grid is one order of magnitude higher than J_{hole} of the ITO. At bias voltages above V_{BI}, J_{hole} of the BNCD:Au-grid is twofold compared to the ITO one. A part of the overall higher current density of the BNCD:Au-grid OLED could be attributed to a higher series resistance (R_S). This, taking into consideration, the higher sheet resistance of 20 Ω/Square of the BNCD:Au-grid anode compared to the ITO anode with a sheet resistance of 12 Ω/Square. Additional measurements by impedance spectroscopy are needed to confirm this presumption. The Figure 3.10 shows the measured total luminance flux (Φ) as function of the applied voltage (V) for both light-emitting devices. Since both devices consist out of the same electron-injecting contact, electron-injection into the lowest unoccupied molecular orbital (LUMO) of the polymer is equally efficient. The total light flux emitted by the OLEDs surface is a sensitive measure of the recombination of electrons and holes that decay radiatively and produce a photon which is not absorbed or internally reflected by the substrate. Despite the 20 % lower transmission and higher refractive index of the BNCD:Au-grid anode compared to the ITO anode, the BNCD:Au-grid anode has a higher total luminance flux.

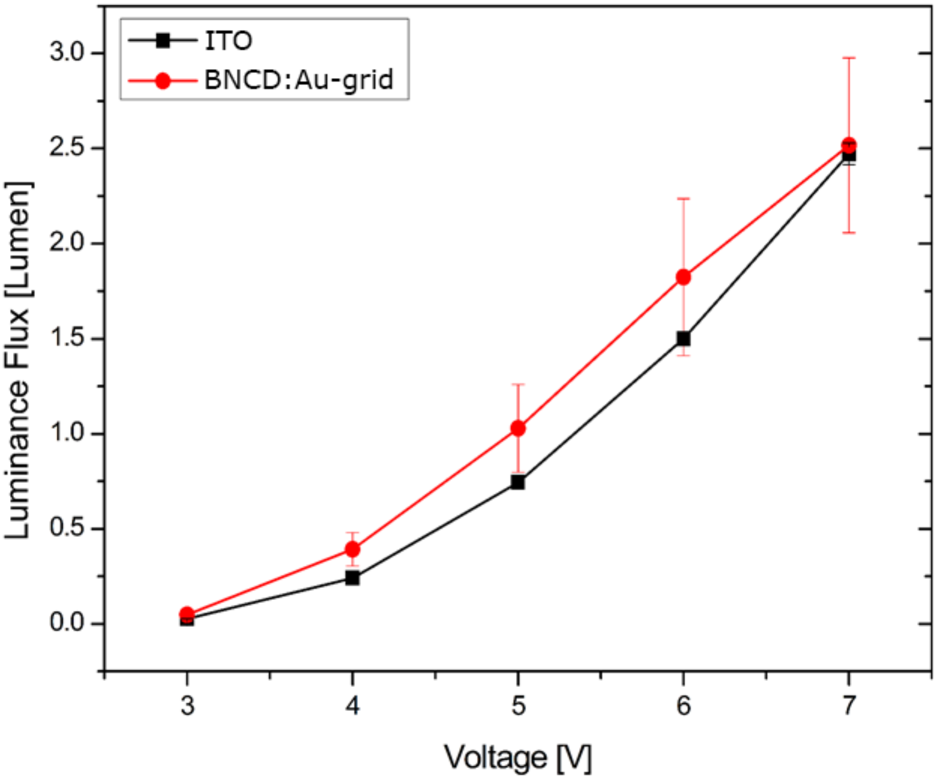

Figure 3.10: The total luminance flux (Φ) as function of the applied voltage on the ITO and BNCD:Au-grid anode OLEDs.

As depicted in Figure 3.11, the luminous power efficacies of the BNCD:Au-grid anode OLEDs are lower compared to the reference ITO anode OLEDs. Despite higher total luminance flux of the BNCD:Au-grid anode devices their luminous power efficacies are slightly lower than the ITO electrode reference devices. This is a direct consequence of the higher current density in the diffusion-dominated and drift-dominated regimes and the unequal increase of the total luminance flux.

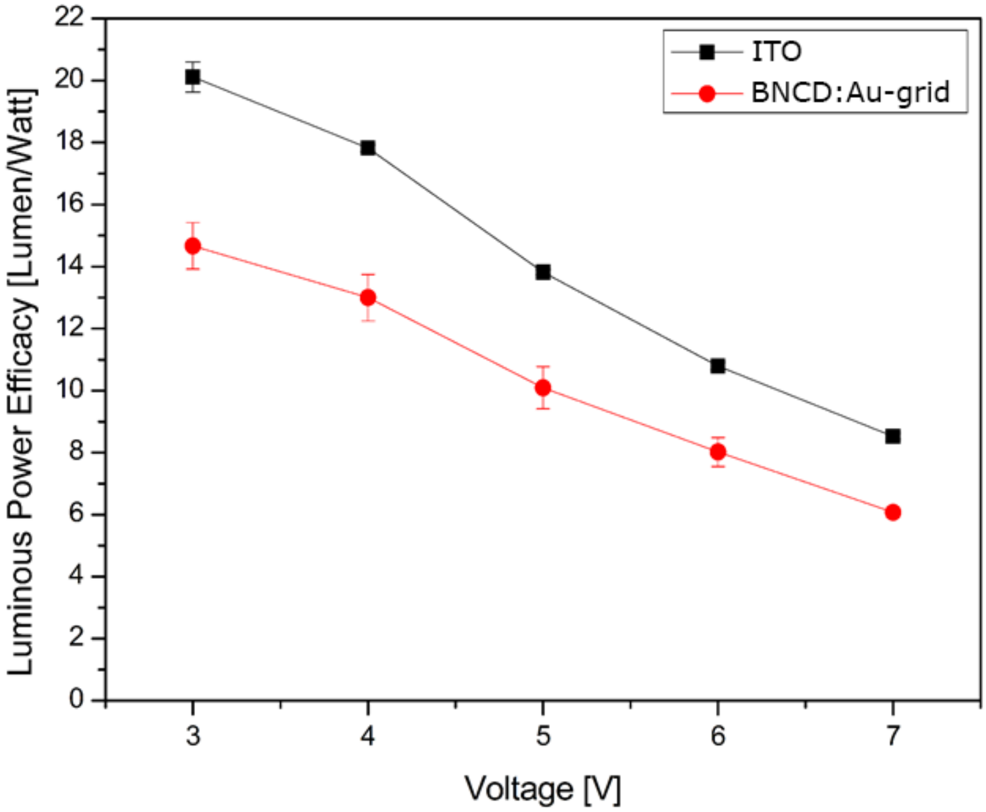

Figure 3.11: The Luminous Power Efficacy of PLEDs with ITO and BNCD-Au Grid electrodes.

3.8 Conclusion

In conclusion, we demonstrate that boron-doped nanocrystalline diamond (BNCD) can be used as a viable alternative to ITO for application as transparent conductive anode in OLEDs. We establish a fabrication methodology for BNCD films on glass with metal (Cr/Au) grids embedded in the BNCD layer. The BNCD:Au-grid anode is prepared by the use of solution processing, vacuum deposition and photolithography steps. The final electrodes have a transparency of ~70 % and a sheet resistance of 20 Ω/Square. The BNCD:Au-grid anode transparency can be further increased by optimizing the grid layout. OLEDs, constructed on BNCD, demonstrate enhanced luminance flux compared to the reference ITO based device. This enhanced luminance flux is attributed to the overall better hole injection from the BNCD anode as expected for a p-type semiconductor. Furthermore, BNCD has the possibility to outperform other thin film transparent electrodes and TCOs in terms of thermal conductivity and chemical stability and can provide p-type conductive inorganic thin films as alternative to n-type ITO.

3.9 References

[1] K. L. Chopra, S. Major, and D. K. Pandya, "Transparent conductors—A status review," *Thin Solid Films*, vol. 102, no. 1, pp. 1–46, 1983.

[2] I. Hamberg and C. G. Granqvist, "Evaporated Sn-doped In2O3 films: Basic optical properties and applications to energy-efficient windows," *J. Appl. Phys.*, vol. 60, no. 11, pp. 123–159, 1986.

[3] K. Bädeker, "über die elektrische leitfähigkeit und die thermoelektrische kraft einiger schwermetallverbindungen," *Ann. Phys.*, vol. 22, pp. 749 – 766, 1907.

[4] C. I. Bright, "Review of Transparent Conductive Oxides (TCO)," in *50 Years of Vacuum Coating Technology and the Growth of the Society of Vacuum Coaters*, D. M. Mattox and V. H. Mattox, Eds. Society of Vacuum Coaters, 2007, pp. 38–45.

[5] C. W. Tang and S. A. VanSlyke, "Organic electroluminescent diodes," *Appl. Phys. Lett.*, vol. 51, no. 12, pp. 913 – 915, 1987.

[6] J. H. Burroughes, D. D. C. Bradley, A. R. Brown, R. N. Marks, K. Mackay, R. H. Friend, P. L. Burns, and A. B. Holmes, "Light-emitting diodes based on conjugated polymers," *Nature*, vol. 347, no. 6293, pp. 539–541, 1990.

[7] K. Ellmer, "Past achievements and future challenges in the development of optically transparent electrodes," *Nat. Photonics*, vol. 6, no. 12, pp. 808–816, 2012.

[8] R. M. Pasquarelli, D. S. Ginley, and R. O'Hayre, "Solution processing of transparent conductors: from flask to film," *Chem. Soc. Rev.*, vol. 40, no. 11, p. 5406, 2011.

[9] R. H. Friend, R. W. Gymer, A. B. Holmes, J. H. Burroughes, R. N. Marks, C. Taliani, D. D. C. Bradley, M. Lo, W. R. Salaneck, D. A. Dos Santos, and J. L. Bre, "Electroluminescence in conjugated polymers," *Nature*, vol. 397, pp. 121–128, 1999.

[10] Z. Chen, W. Li, R. Li, Y. Zhang, G. Xu, and H. Cheng, "Fabrication of highly transparent and conductive indium-tin oxide thin films with a high figure of merit via solution processing," *Langmuir*, vol. 29, no. 45, pp. 13836–42, 2013.

[11] J. Lee, S. Lee, G. Li, M. a. Petruska, D. C. Paine, and S. Sun, "A facile solution-phase approach to transparent and conducting ITO nanocrystal

assemblies," *J. Am. Chem. Soc.*, vol. 134, no. 32, pp. 13410–13414, 2012.

[12] D. S. Hecht and R. B. Kaner, "Solution-processed transparent electrodes," *MRS Bull.*, vol. 36, no. 10, pp. 749–755, Oct. 2011.

[13] S. Hong, S. Kim, and J. I. Han, "Solution-processed indium–tin-oxide nanoparticle transparent conductors on flexible glass substrate with high optical transmittance and high thermal stability," *Jpn. J. Appl. Phys.*, vol. 53, pp. 1–5, 2014.

[14] J. Puetz and M. a. Aegerter, "Direct gravure printing of indium tin oxide nanoparticle patterns on polymer foils," *Thin Solid Films*, vol. 516, no. 14, pp. 4495–4501, May 2008.

[15] C. Hyun and Y. Young-Hoon, "Characterization of indium tin oxide (ITO) thin films prepared by a sol–gel spin coating process." Ceramics International, pp. 615–619, 2011.

[16] M. . de Jong, D. P. . Simons, M. . Reijme, L. . van IJzendoorn, a. . Denier van der Gon, M. J. . de Voigt, H. . Brongersma, and R. . Gymer, "Indium diffusion in model polymer light-emitting diodes," *Synth. Met.*, vol. 110, no. 1, pp. 1–6, Mar. 2000.

[17] F. So and D. Kondakov, "Degradation mechanisms in small-molecule and polymer organic light-emitting diodes," *Adv. Mater.*, vol. 22, no. 34, pp. 3762–3777, 2010.

[18] S. K. Park, J. I. Han, D. G. Moon, and W. K. Kim, "Mechanical stability of externally deformed indium-tin-oxide films on polymer substrates," *Jpn. J. Appl. Phys.*, vol. 42, no. 2 A, pp. 623–629, 2003.

[19] Y.-N. Kim, H.-G. Shin, J.-K. Song, D.-H. Cho, H.-S. Lee, and Y.-G. Jung, "Thermal Degradation Behavior of Indium Tin Oxide Thin Films Deposited by Radio Frequency Magnetron Sputtering," *J. Mater. Res.*, vol. 20, no. 06, pp. 1574–1579, 2005.

[20] D. Thuau, I. Koymen, and R. Cheung, "A microstructure for thermal conductivity measurement of conductive thin films," *Microelectron. Eng.*, vol. 88, no. 8, pp. 2408–2412, 2011.

[21] T. Ashida, A. Miyamura, N. Oka, Y. Sato, T. Yagi, N. Taketoshi, T. Baba, and Y. Shigesato, "Thermal transport properties of polycrystalline tin-doped indium oxide films," *J. Appl. Phys.*, vol. 105, no. 7, p. 073709, 2009.

[22] S. Chung, J. H. Lee, J. Jeong, J. J. Kim, and Y. Hong, "Substrate thermal conductivity effect on heat dissipation and lifetime improvement of organic light-emitting diodes," *Appl. Phys. Lett.*, vol. 94, no. 25, pp. 1–4, 2009.

[23] Polinares EU Policy on Natural Resources, "Fact Sheet: Indium," *Polinares Consort. 2012*, 2012.

[24] J. R. Dodson, a. J. Hunt, H. L. Parker, Y. Yang, and J. H. Clark, "Elemental sustainability: Towards the total recovery of scarce metals," *Chem. Eng. Process. Process Intensif.*, vol. 51, pp. 69–78, 2012.

[25] K. Nagano, T. Nishizawa, Y. Umeda, T. Kasai, T. Noguchi, K. Gotoh, N. Ikawa, Y. Eitaki, Y. Kawasumi, T. Yamauchi, H. Arito, and S. Fukushima, "Inhalation carcinogenicity and chronic toxicity of indium-tin oxide in rats and mice," *J. Occup. Health*, vol. 53, no. 3, pp. 175–187, 2011.

[26] S. Narushima, M. Orita, M. Hirano, and H. Hosono, "Electronic structure and transport properties in the transparent amorphous oxide semiconductor 2 CdO · GeO2," *Phys. Rev. B*, vol. 66, no. 3, pp. 1–8, 2002.

[27] S. Choi, S.-J. Kim, C. Fuentes-Hernandez, and B. Kippelen, "ITO-free large-area organic light-emitting diodes with an integrated metal grid.," *Opt. Express*, vol. 19 Suppl 4, no. July, pp. A793–803, Jul. 2011.

[28] M.-G. Kang and L. J. Guo, "Nanoimprinted Semitransparent Metal Electrodes and Their Application in Organic Light-Emitting Diodes," *Adv. Mater.*, vol. 19, no. 10, pp. 1391–1396, May 2007.

[29] J. Y. Lee, S. T. Connor, Y. Cui, and P. Peumans, "Solution-processed metal nanowire mesh transparent electrodes," *Nano Lett.*, vol. 8, no. 2, pp. 689–692, 2008.

[30] L. Hu, J. Li, J. Liu, G. Grüner, and T. Marks, "Flexible organic light-emitting diodes with transparent carbon nanotube electrodes: problems and solutions.," *Nanotechnology*, vol. 21, no. 15, p. 155202, Apr. 2010.

[31] J. Wu, M. Agrawal, A. Becerril, Z. Bao, Z. Liu, Ḱ. Y. Chen, and P. Peumans, "Organic Light-Emitting Diodes on Solution-Processed Graphene Transparent Electrodes," *ACS Nano*, vol. 4, no. 1, pp. 43–48, 2010.

[32] N. Li, S. Oida, G. S. Tulevski, S.-J. Han, J. B. Hannon, D. K. Sadana, and T.-C. Chen, "Efficient and bright organic light-emitting diodes on single-layer graphene electrodes.," *Nat. Commun.*, vol. 4, p. 2294, Jan. 2013.

[33] K. Fehse, K. Walzer, K. Leo, W. Lövenich, and a. Elschner, "Highly Conductive Polymer Anodes as Replacements for Inorganic Materials in High-Efficiency Organic Light-Emitting Diodes," *Adv. Mater.*, vol. 19, no. 3, pp. 441–444, Feb. 2007.

[34] Y. L. Zhong, A. Midya, Z. Ng, Z.-K. Chen, M. Daenen, M. Nesladek, and K. P. Loh, "Diamond-based molecular platform for photoelectrochemistry.," *J. Am. Chem. Soc.*, vol. 130, no. 51, pp. 17218–9, Dec. 2008.

[35] S. De, P. J. King, P. E. Lyons, U. Khan, and J. N. Coleman, "Size effects and the problem with percolation in nanostructured transparent conductors," *ACS Nano*, vol. 4, no. 12, pp. 7064–7072, 2010.

[36] J. Moon, J.-W. Shin, H. Cho, J.-H. Han, N. S. Cho, J. T. Lim, S. K. Park, H. K. Choi, S.-Y. Choi, J.-H. Kim, M.-J. Maeng, J. Seo, Y. Park, and J.-I. Lee, "Technical issues in graphene anode organic light emitting diodes," *Diam. Relat. Mater.*, vol. 57, no. August, pp. 68–73, 2015.

[37] J. Huang, P. F. Miller, J. S. Wilson, a. J. de Mello, J. C. de Mello, and D. D. C. Bradley, "Investigation of the Effects of Doping and Post-Deposition Treatments on the Conductivity, Morphology, and Work Function of Poly(3,4-ethylenedioxythiophene)/Poly(styrene sulfonate) Films," *Adv. Funct. Mater.*, vol. 15, no. 2, pp. 290–296, Feb. 2005.

[38] D. R. Tallant, J. E. Parmeter, M. P. Siegal, and R. L. Simpson, "The thermal stability of diamond-like carbon," *Diam. Relat. Mater.*, vol. 4, no. 3, pp. 191–199, Apr. 1995.

[39] S. Rossi, M. Alomari, Y. Zhang, S. Bychikhin, D. Pogany, J. M. R. Weaver, and E. Kohn, "Thermal analysis of submicron nanocrystalline diamond films," *Diam. Relat. Mater.*, vol. 40, pp. 69–74, Nov. 2013.

[40] D. Hill, "The Optical Outcoupling of Organic Light Emitting Diodes," University Dresden, 2008.

[41] A. Taylor, L. Fekete, P. Hubík, A. Jäger, P. Janíček, V. Mortet, J. Mistrík, and J. Vacík, "Large area deposition of boron doped nano-crystalline diamond films at low temperatures using microwave plasma enhanced chemical vapour deposition with linear antenna delivery," *Diam. Relat. Mater.*, vol. 47, pp. 27–34, Aug. 2014.

[42] F. L. M. Sam, M. A. Razali, K. D. G. I. Jayawardena, C. a. Mills, L. J. Rozanski, M. J. Beliatis, and S. R. P. Silva, "Silver grid transparent conducting electrodes for organic light emitting diodes," *Org. Electron.*, vol. 15, no. 12, pp. 3492–3500, 2014.

[43] W. C. H. Choy, W. K. Chan, and Y. Yuan, "Recent advances in transition metal complexes and light-management engineering in organic optoelectronic devices," *Adv. Mater.*, pp. 1–32, 2014.

[44] S. Braun, W. R. Salaneck, and M. Fahlman, "Energy-level alignment at organic/metal and organic/organic interfaces," *Adv. Mater.*, vol. 21, no. 14–15, pp. 1450–1472, 2009.

[45] I. D. Parker, "Carrier tunneling and device characteristics in polymer light-emitting diodes," *J. Appl. Phys.*, vol. 75, no. 3, pp. 1656–1666, 1994.

Chapter 4 Microwave Annealing of Poly (3,4-ethylenedioxythiophene):Poly(styrenesulfonate)

In this chapter we investigate the applicability of microwave annealing as post-deposition treatment for Poly(3,4-thylenedioxythiophene):Poly(styrenesulfonate) (PEDOT:PSS) thin films. PEDOT:PSS is typically the second layer in the OLED stack, the layer on top of the transparent anode and functions as electron blocking layer. Like all organic layers in an organic optoelectronic device, PEDOT:PSS can deposited by a variety of printing and coating techniques e.g.: spin-coating, screen printing, ultrasonic spray coating. After solution deposition of these organic layers a thermal treatment is needed to remove solvents and other additives. This thermal treatment is typically performed by a conventional hotplate or oven. Just as in typical household cooking or industrial microwave processing of e.g.: ceramics, minerals, wood and rubbers, the use of microwave thermal annealing in the OLED production process could yield faster processing times and energy savings.

4.1 Introduction

The conjugated polymer PEDOT:PSS has been around for more than two decades [1]. Although its electronic properties are still under investigation [2] PEDOT:PSS is already used in a variety of organic optoelectronic applications, e.g.: Organic Photovoltaics (OPV)[3], Organic Light-Emitting Devices (OLEDs) [4], and other applications, e.g.: antistatic coatings [5], anode material for capacitors [6]. PEDOT:PSS has interesting properties as compared to other polythiophenes as it exhibits a relatively good electrochemical, ambient and thermal stability of its electrical properties [7]. PEDOT is a concatenation of ethylenedioxythiophene (EDOT) monomers, is insoluble in most organic solvents and oxidizes in ambient atmosphere. To overcome these deficiencies, poly (styrenesulfonate) (PSS) is added resulting in an aqueous dispersion. The chemical structure of PEDOT:PSS is shown in Figure 4.1.

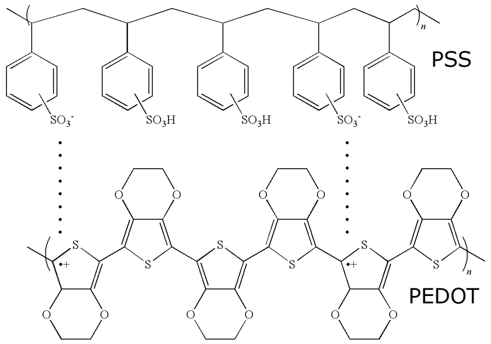

Figure 4.1: The chemical structure of PEDOT:PSS.

Its wide applicability is thanks to its high optical transparency and low resistivity and its ability to be processed from solution. A thin film of PEDOT:PSS is an integral part of an OLED device stack [8] and has several purposes. It is deposited on top of a transparent electrode, most commonly an indium tin oxide (ITO) thin film. The PEDOT:PSS layer slows down the diffusion of oxygen and indium originating from the ITO layer [9], [10] and modifies the surface wetting properties [11]. Furthermore, it lowers the energy barrier for the injection of holes and blocks electrons from reaching the hole-injecting contact preventing surface recombination [9][12]. OLED device studies have shown that the incorporation of a PEDOT:PSS layer increases the external quantum efficiency and increase the lifetime [13]. As aqueous dispersion, PEDOT:PSS can be processed from solution by either spin-coating or other printing or coating techniques. To remove solvents, a thermal post treatment is needed [14]. In a laboratory environment, this thermal post-deposition treatment is performed via conventional thermal conduction methods; e.g.: hotplate or oven. These conventional methods, however, do not scale to industrial sized, high throughput production processes. The annealing time is limited due to the onset of thermal degradation at temperatures above 200 °C [12][15]. In this chapter we investigate the microwave annealing of PEDOT:PSS thin films to overcome these limitations. Furthermore a comparison is made between hotplate annealing and microwave annealing of thin PEDOT:PSS films coated with the screen printing technique. Based on our results, a significant reduction in annealing time is achieved using a microwave annealing system.

4.2 The microwave system

Conventional heat transfer modes, conduction, convection and radiation, transfer energy from the surface of the heat-source to the surface of the material. In contrast, microwave energy is delivered directly throughout the material due to molecular interactions with the electromagnetic field. In the material, an electromagnetic energy conversion occurs instead of a thermal energy transfer due to a thermal gradient. Because microwave radiation penetrates the material and is converted within the material to kinetic energy (heat) a uniform heating is achieved. The most dominant mechanisms that are responsible for the electromagnetic energy conversion are ionic conduction and dipolar rotation [16].

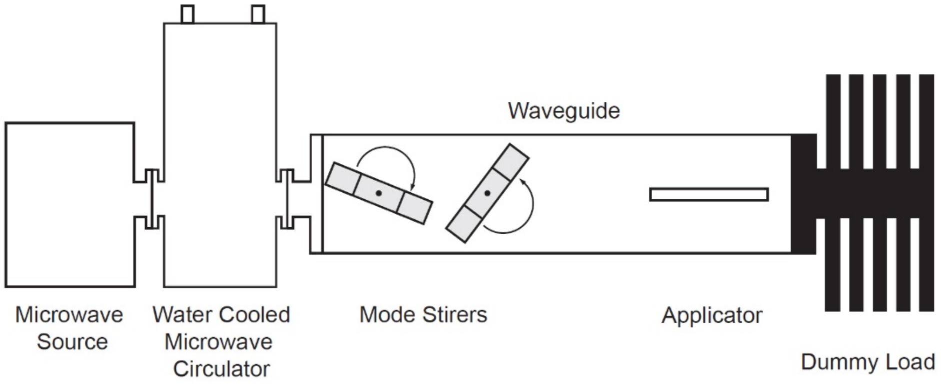

Figure 4.2: Schematic overview of the microwave annealing system. The sample are placed in the applicator.

Figure 4.2 illustrates the configuration of the microwave annealing system developed in collaboration with Lumoza (n.v.). The electromagnetic waves (2.45GHz) are generated by the microwave source, which is powered by an adjustable microwave power generator. The microwave power generator enables the system to vary the generated electromagnetic power from 50 to 1000 Watt. As the generated electromagnetic waves are coupled into the waveguide they pass the water cooled microwave circulator, i.e. reflection load, which protects the microwave source from being damaged by reflected electromagnetic waves. The electromagnetic waves propagating through the waveguide are stirred to a multimode electromagnetic field to prevent standing waves. By preventing standing (electromagnetic) waves in the waveguide and in the applicator area, which is located at the end of the waveguide, the probability of local hotspots is drastically reduced. The formation of local hotspots in the applicator area could potentially damage the samples as a result of non-uniform heating of the samples present in the applicator. Part of the electromagnetic energy that is not absorbed by the samples is absorbed by the dummy load or reflected back towards the start of the waveguide. In order to meet the requirement of a multimode uniform electromagnetic field, rotating mode stirrers where placed inside the waveguide. To insure the isolated effect of both mode stirrers, the physical orientation of each mode stirrer is shifted at least 90° with respect to each other. Furthermore, the rotation speed of each mode stirrer is chosen as a prime number to insure that the rotation speeds are not a multiple of each other and the direction of their rotation is opposite. To obtain the correct behaviour of the mode stirrers, the shape and material were experimentally determined. The selected group of materials was limited to dielectrics to prevent reflections from the mode stirrers. To further determine the mode stirrer material, a systematic variation of the stirrer materials and careful measurement of the attenuation and phase shift caused by each material at 3 different orientations in the wave guide is performed. The test samples, with equal dimensions, were placed at the entrance of the waveguide, inline centred, inline against the waveguide wall and transversal centred. From these measurements, it was found that the material

Macor, a glass ceramic, caused an adequate differential phase shift of 26.8°. To further optimize the stirrer design different shapes, e.g.: cylindrical, square, and mutual configurations, e.g.: spacing between stirrer blocks, were systematically varied. From these results it was found that a square shaped stirrer designed, as shown in Figure 4.3, is the most optimal. When the stirrer is inline (0°) it introduces a phase shift of 168°, when the stirrer is rotated by 45° it introduces a phase shift of 197° and when it is transversal positioned in the waveguide (90°) it introduces a phase shift of 271°. By introducing 2 stirrers in the waveguide, a uniform multimode electromagnetic field is obtained, ideal to test microwave annealing as alternative for hotplate annealing.

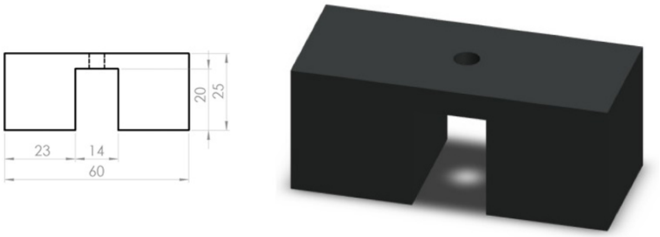

Figure 4.3: (left) 2D CAD drawing of the stirrer design, units: mm (right) 3D render of the stirrer design.

4.3 Annealing time

The annealing time of a PEDOT:PSS film is mainly dependent on the amount of PEDOT:PSS wet solution, the specific heat of the solution and the annealing temperature. To gain insight into the annealing time of these PEDOT:PSS films, in-situ current measurements were performed. These measurements were performed by applying a 10 V bias on the screen printed PEDOT:PSS thin films while annealing the samples on a conventional hotplate. As shown in Figure 4.4 a clear distinction is observed when annealing the samples at different temperatures on a hotplate. While the solvents and additives evaporate, the current increases rapidly and then stabilizes in an asymptotic manner. The maximum value of the current varies slightly with the annealing temperature. A clear distinction can be observed for the time to reach this maximum current based on the annealing temperature and is inverse proportional this temperature. The time to reach the maximum current will serve as a reference to compare the annealing time of hotplate and microwave annealed samples.

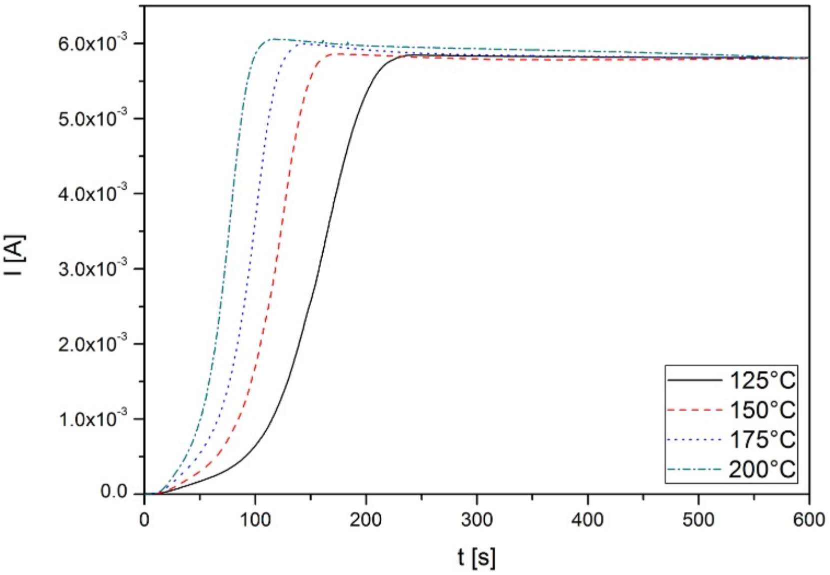

Figure 4.4: In-situ current measurement while annealing of screen printed PEDOT:PSS film on a hotplate at various temperatures.

Figure 4.5 shows the average time to reach the stable current on a conventional hotplate. As the temperature increases, the time to reach a stable current decreases and gets less disperse. When repeating this experiment in our microwave annealing system, as depicted in Figure 4.6, a similar trend is observed when varying the power of the microwave. It is also clear that the stable current is reached much faster than in the hotplate experiment. These results suggest that the microwave could potentially be a much faster technique than the hotplate for annealing. However, in the following sections, a morphological and electrical investigation of the annealed PEDOT:PSS films is performed to verify their integrity.

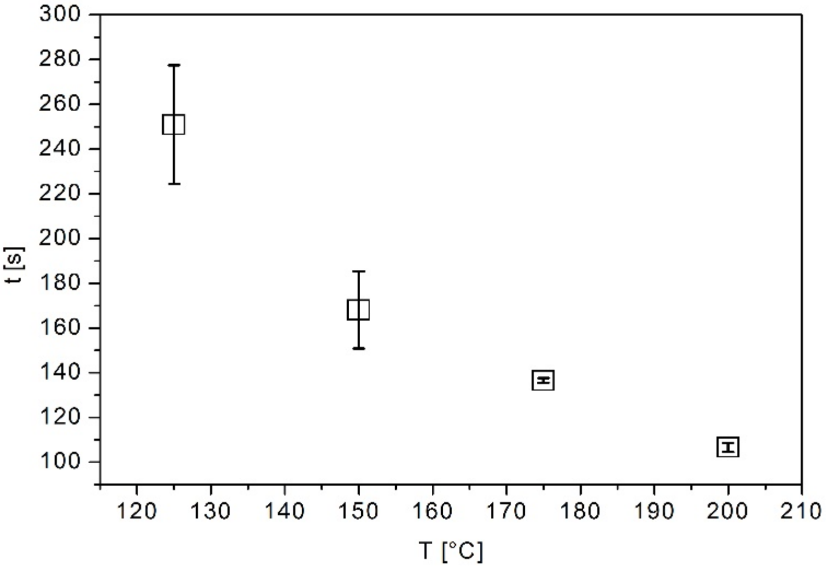

Figure 4.5: Average times to reach a stable current of PEDOT:PSS films on a hotplate.

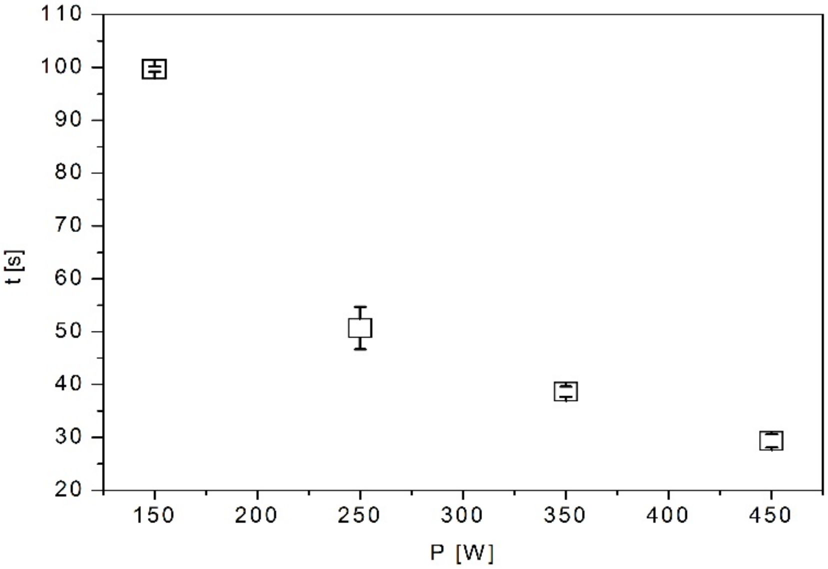

Figure 4.6: Average times to reach a stable current of PEDOT:PSS films on our microwave annealing system.

4.4 Morphological characterisation

The morphology of the annealed PEDOT:PSS films is compared by SEM, as shown in Figure 4.7. From these SEM images it is clear that there is no distinct structural or morphological difference between the reference hotplate annealed samples at 130°C and hotplate annealed samples at the onset of thermal degradation of 200°C [15], column a and b. More importantly there is also no evidence of a change in morphology between the hotplate annealed samples and the microwave annealed samples, column a/b and column c resp.

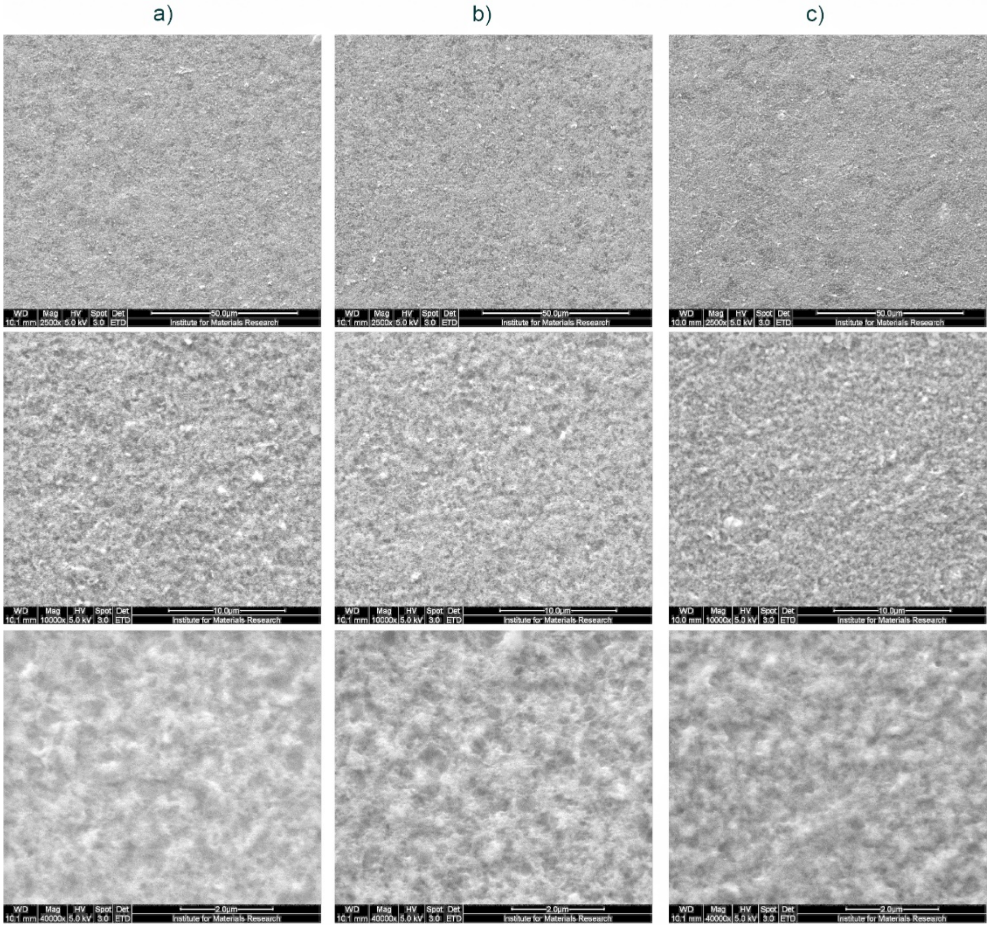

Figure 4.7: SEM images of annealed PEDOT:PSS films. Column a: hotplate annealed at 130 °C for 600 s. Column b: hotplate annealed at 200 °C for 600 s. Column c: Microwave annealed at 200 W for 70 s. The magnification increases from the top to the bottom row, 50 µm, 10 µm and 2 µm respectively.

4.5 Electrical characterisation

The electronic properties of both hotplate and microwave annealed films were evaluated by measuring the in-plane sheet resistance using the Van der Pauw method [17]. Figure 4.8 shows the in-plane sheet resistance of the hotplate annealed PEDOT:PSS films. These films were annealed in ambient conditions for 600 s and cooled down to room temperature before measuring the sheet resistance. The results show the increasing sheet resistance with increasing annealing temperature. This effect can be attributed to the hygroscopic nature of PEDOT:PSS films, as these films are annealed in atmospheric conditions, they take up oxygen and water vapour from their surroundings [12] [15].

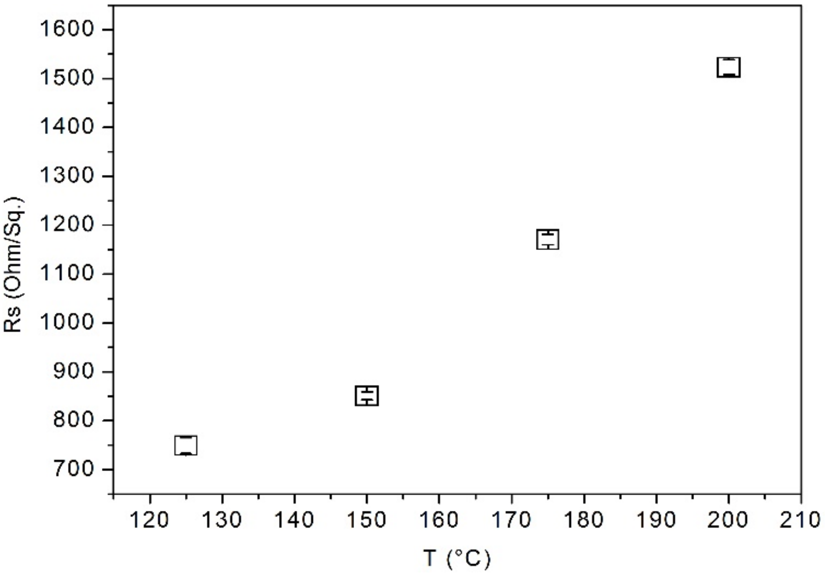

Figure 4.8: The in-plane sheet resistance as function of hotplate annealing temperature.

Figure 4.9 shows the in-plane sheet resistance of the microwave annealed films at various microwave powers. These measurements were performed after the films cooled down to room temperature and the annealing time was based on the time to reach a stable current. A similar trend is observed as with the hotplate annealed films, with increasing microwave power the in-plane sheet resistance increases. It is shown that the annealed PEDOT:PSS films in our microwave system at 150 W for 100 s reached a similar sheet resistance as the hotplate annealed samples at 125 °C for 251 s. The microwave annealing step is 2.5 times faster than the conventional hotplate annealing step without interfering with the electronic properties of PEDOT:PSS.

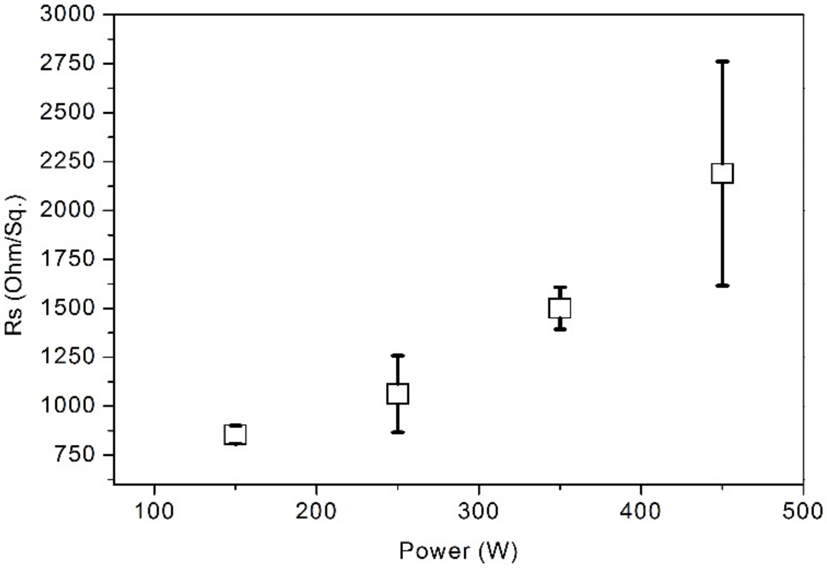

Figure 4.9: The in-plane sheet resistance as function of the microwave power.

4.6 Conclusion

We studied the effects of microwave annealing as post-deposition treatment on organic semiconducting thin films, PEDOT:PSS, in comparison to a conventional hotplate annealing treatment. We investigated effects of these treatments on the morphological and electrical properties of these organic thin films to determine the applicability of the microwave technique. In–situ current measurements suggest that the microwave annealing technique is 2.5 times faster than the hotplate technique. Morphological investigations show no difference in morphology between hotplate annealed and microwave annealed samples. From the investigation of the electronic properties of these annealed organic films, we have observed that the sheet resistance increases rapidly when the power of the microwave is increased above 150W. Using powers lower or equal to 150 W will yield comparable results in terms of sheet resistance for both techniques. Furthermore, the measured annealing time decreases by a factor of 2.5 times, showing that microwave annealing is a feasible thermal post-deposition treatment for organic semiconducting thin films.

4.7 References

[1] F. Jonas and L. Schrader, "Conductive Modifications of Polymers with Polypyrroles and Polythiophenes," *Synth. Met.*, vol. 43, pp. 831–836, 1991.

[2] K. van de Ruit, I. Katsouras, D. Bollen, T. van Mol, R. a. J. Janssen, D. M. de Leeuw, and M. Kemerink, "The Curious Out-of-Plane Conductivity of PEDOT:PSS," *Adv. Funct. Mater.*, vol. 23, no. 46, pp. 5787–5793, Dec. 2013.

[3] G. Dennler, M. C. Scharber, and C. J. Brabec, "Polymer-Fullerene Bulk-Heterojunction Solar Cells," *Adv. Mater.*, vol. 21, no. 13, pp. 1323–1338, Apr. 2009.

[4] M. T. Bernius, M. Inbasekaran, J. O'Brien, and W. Wu, "Progress with Light-Emitting Polymers," *Adv. Mater.*, vol. 12, no. 23, pp. 1737–1750, Dec. 2000.

[5] F. Jonas and J. T. Morrison, "3,4-Polyethylenedioxythiophene (PEDOT): Conductive Coatings Technical Applications and Properties," *Synth. Met.*, vol. 85, pp. 1397–1398, 1997.

[6] B. L. Groenendaal, F. Jonas, D. Freitag, H. Pielartzik, and J. R. Reynolds, "Poly(3,4-ethylenedioxythiophene) and Its Derivatives : Past , Present , and Future," *Adv. Mater.*, vol. 12, no. 7, pp. 481–494, 2000.

[7] A. M. Nardes, "On the conductivity of PEDOT:PSS thin films," TU Eindhoven, 2007.

[8] J. H. Cook, H. a. Al-Attar, and A. P. Monkman, "Effect of PEDOT–PSS resistivity and work function on PLED performance," *Org. Electron.*, vol. 15, no. 1, pp. 245–250, Jan. 2014.

[9] G. Greczynski, T. Kugler, M. Keil, W. Osikowicz, M. Fahlman, and W. . Salaneck, "Photoelectron spectroscopy of thin films of PEDOT–PSS conjugated polymer blend: a mini-review and some new results," *J. Electron Spectros. Relat. Phenomena*, vol. 121, no. 1–3, pp. 1–17, Dec. 2001.

[10] T. P. Nguyen, P. Le Rendu, P. D. Long, and S. a. De Vos, "Chemical and thermal treatment of PEDOT:PSS thin films for use in organic light emitting diodes," *Surf. Coatings Technol.*, vol. 180–181, pp. 646–649, Mar. 2004.

[11] J. Huang, P. F. Miller, J. C. de Mello, a. J. de Mello, and D. D. C. Bradley, "Influence of thermal treatment on the conductivity and morphology of PEDOT/PSS films," *Synth. Met.*, vol. 139, no. 3, pp. 569–572, Oct. 2003.

[12] Y. Kim, a Ballantyne, J. Nelson, and D. Bradley, "Effects of thickness and thermal annealing of the PEDOT:PSS layer on the performance of polymer solar cells," *Org. Electron.*, vol. 10, no. 1, pp. 205–209, Feb. 2009.

[13] G. Greczynski, T. Kugler, and W. . Salaneck, "Characterization of the PEDOT-PSS system by means of X-ray and ultraviolet photoelectron spectroscopy," *Thin Solid Films*, vol. 354, no. 1–2, pp. 129–135, Oct. 1999.

[14] J. Huang, P. F. Miller, J. S. Wilson, a. J. de Mello, J. C. de Mello, and D. D. C. Bradley, "Investigation of the Effects of Doping and Post-Deposition Treatments on the Conductivity, Morphology, and Work Function of Poly(3,4-ethylenedioxythiophene)/Poly(styrene sulfonate) Films," *Adv. Funct. Mater.*, vol. 15, no. 2, pp. 290–296, Feb. 2005.

[15] E. Vitoratos, S. Sakkopoulos, E. Dalas, N. Paliatsas, D. Karageorgopoulos, F. Petraki, S. Kennou, and S. Choulis, "Thermal degradation mechanisms of PEDOT:PSS," *Org. Electron.*, vol. 10, no. 1, pp. 61–66, Feb. 2009.

[16] E. T. Thostenson and T.-W. Chou, "Microwave processing: fundamentals and applications," *Compos. Part A Appl. Sci. Manuf.*, vol. 30, no. 9, pp. 1055–1071, Sep. 1999.

[17] L. J. Van Der Pauw, "A method of measuring specific resistivity and hall effect of discs of arbitrary shape," *Philips Res. Reports*, vol. 13, no. 1, pp. 1–9, 1958.

Chapter 5 Ultrasonic spray coating as deposition technique for the light-emitting layer in polymer LEDs

In this chapter the ultrasonic spray coating technique is introduced as an alternative wet solution process for the deposition of the emissive layer for polymer OLEDs. Ultrasonic spray coating is a non-contact coating technique capable of coating complex three-dimensional substrates. Furthermore, because of its low solution waste and independence of substrate size it is an ideal candidate for a high throughput large-scale production process. An investigation on the use of this coating technique in ambient conditions is performed and a comparison with spin coated OLEDs in inert atmosphere are made. Uniform low roughness thin films with a typical thickness of 80 nm are obtained by varying the polymer-solvent mixture and spray coater parameters. Furthermore, it is shown that the final deposited layer thickness can easily be tuned by varying the flow rate and nozzle speed. OLEDs are produced and reach a luminous power efficacy in the order of 10 Lumen/Watt. Through the use of various optical and analytical techniques it is demonstrated that the applied ultrasonic atomization has no noteworthy influence on the original properties of the polymer and on the resulting OLED’s efficacy. Ultrasonic spray coating is therefore a viable deposition technique for the production of OLEDs.

5.1 Introduction

Solution processing of organic optoelectronics holds the promise of cost efficient, high throughput production of large area devices. In contrast to vacuum deposition, solution processing techniques are more conveniently upscalable and more advanced printing techniques allow thin film patterning during the deposition. *However, if large-scale solution processing proves to be problematic or impossible, the concept of organic optoelectronic devices would become a scientific curiosity with little consequence to mankind* [1]. At the present time, all the layers of a typical OLED device can be deposited via a solution processing thin film deposition technique [2]. The transparent electrode, typically ITO, has been spin-cast from a monodisperse ITO nanocrystal solution [3] and spin-coated from solution prepared by means of sol-gel chemistry [4]. The polymer interlayers and active materials have been deposited by a multitude of coating and printing techniques [5] but also recently small-molecule based thin films have been deposited from solution whereas previously this was done via thermal evaporation [6]. Metallic electrodes have been fabricated via the deposition of a nano-particle solution [7].

We are, however, not quite there yet as a large research effort is needed before these proof-of-concept laboratory solution processing techniques can be transferred to industrial scale. Replacement of physical vapour deposition (PVD) processes of thin-film electrodes, e.g.: thermal evaporation, sputtering, by solution deposition processes has commenced. However, their optoelectronic properties are still not as good as their PVD processed counterparts, e.g.: ITO [3]. Furthermore, the most widely used solution deposition technique for all organic layers in the OLED device is spin coating because of its excellent thin film forming property with a wide variety of solution and substrate properties. With more roll-to-roll compatible, scalable coating and printing techniques the substrate surface properties and ink formulations are, however, highly critical [1].

In the next section of this chapter an overview of the most relevant printing and coating techniques in the field of OLEDs is given.

5.2 Solution deposition techniques

Solution deposition techniques, depicted Figure 5.1, allow the deposition of thin organic films at atmospheric pressure and ambient temperatures. A direct advantage of this is the absence of high temperatures and near vacuum pressures that allow the use of flexible substrates such as polyethylene terephthalate (PET). However, liquid deposition requires an additional processing step to remove additives and solvents to obtain the final solid film.

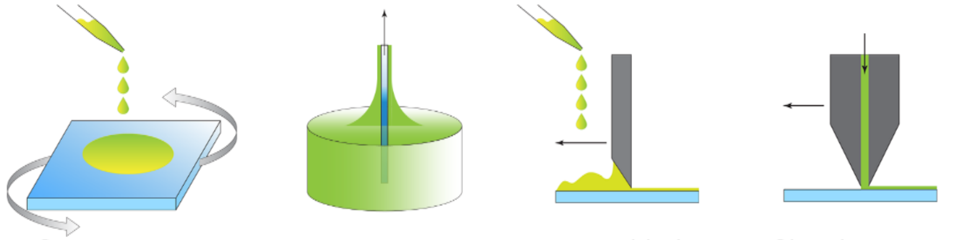

Spin coating

Dip coating

Doctor blading

Slot-die coating

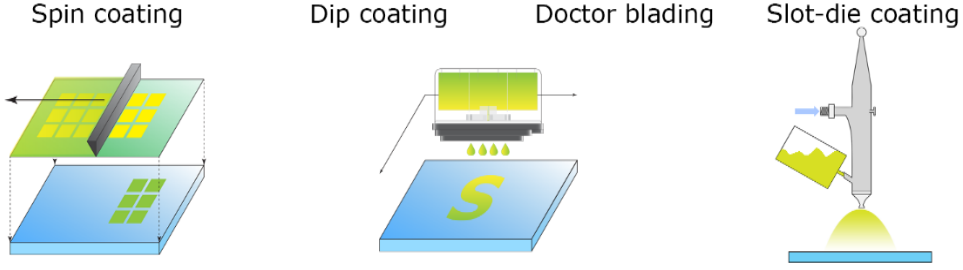

Screen printing

Ink-jet Printing

Spray coating

Figure 5.1: Coating and printing techniques.

The spin coating technique is the laboratory standard when producing polymer films, typically ~100 nm, for organic light-emitting diodes. This coating technique has been used in the semiconductor industry for over 30 years to spread photoresist on silicon wafers and is involved in crucial steps for the production of DVDs and CDs. Spin coating is a planar coating technique which yields highly reproducible films with high structural uniformity [8]. Spin coating is a process where an excess of solution is applied to a horizontal rotating substrate, leaving a solid or wet planar film as a result of ejection and evaporation of the solvent. The substrate is held in place by the vacuum chuck which is located in centre of the substrate holder. The acceleration and the end velocity are user adjustable as well as the spin time and are important parameters for the layer thickness. The solution which is flung off during the spin coating process is captured by the fluid recipient. A uniform thin film is obtained after spin-off and solvent evaporation. By adjusting the polymer weight fraction of the solution and spin-coating parameters, e.g.: the acceleration and rotation speed, the final film thickness can easily be tuned. Despite its ease-of-use, the spin coating process does not comply well with large-area production where typically substrates sizes go up to 30 cm in diameter [8]. Nor is the process compatible with high throughput roll-to-roll production and it does not allow patterning. Furthermore, spin-coating is a wasteful process, less than 5 % of the initial dispensed solution is utilised and reusing the wasted solution will certainly not be unproblematic [9]. Alternatively, a more roll-to-roll compatible coating technique is dip-coating. Here, a thin (wet) layer is formed by dipping the substrate in the solution reservoir. While retracting the substrate from the solution a thin film is formed. The excess solution drains back into the solution reservoir. To prevent a gradient in the formed film, the choice of solvent and the retraction speed is of high importance. However, dip-coating does not allow patterning and covers both sides of the substrate. A detailed study of spin and dip coating of light-emitting polymers can be found in [10]. A simple, roll-to-roll compatible method of coating substrates, single sided and accurately controlling the final film thickness is doctor-blading also referred to as blade or knife coating. In contrast to spin coating, the loss of solution is minimized to less than 5 % [1]. A thin, wet film is distributed over the substrate as a blade passes in a linearly fashion at some distance over the substrate. The final film thickness can be controlled accurately by tuning the substrate-blade distance, solution concentration and final solid film density [1]. This technique is very well suited for thin film, large-area deposition without any pattern. An example of a doctor-bladed polymer OLED can be found in [11]. In contrast to the doctor-blade deposition technique where the solution is supplied in front of the blade, with slot-die coating the solution is pumped through a coating head. With the appropriate coating head it is possible to coat one-dimensional (1D) patterns (lines). Opposed to the 1D coating techniques discussed above, screen-printing allows the deposition of two-dimensional (2D) thin film patterns. As the name implies, the pattern is transferred from a screen to the substrate. The screen consists of a synthetic or metal wire mesh framed under tension and is coated with a negative of the patterned to be printed. The print solution is applied on top of the screen while the screen is in close proximity of the substrate. The print solution is forced through the screen onto the substrate be a so-called squeegee. The squeegee pushes a segment of the screen on to the substrate and moves in linear motion over the screen transferring the pattern to substrate. A consequence of this method is the requirement of high viscous and low volatile printing solutions. An example of screen-printed OLEDs can be found in the work of Birnstock, et. al. [12]. As spin-coating the following deposition techniques, ink-jet printing and spray coating, are also non-contact techniques but allow sub-centimetre patterning. Ink-jet technology is a common printing technique used for transferring digital information from a computer to paper and can be found in nearly every office and home today. The first practical example of the ink-jet printing technology was patented by R. Elmqvist of Siemens in Sweden in 1948 [13]. From the 1970s and the decades thereafter major companies like IBM, Siemens, Canon and Hewlett-Packard started massive development programs to commercialize ink-jet printing technologies, i.e.: continuous ink-jet technology and Drop-On-Demand (DOD) ink-jet technology. In the last decade, a large research effort has been put in the accurate deposition of functional materials, including polymers for organic electronics [14]–[16]. Ink-jet printing is a contactless printing technique for the precise deposition of droplets using small amounts of material and enables digital patterning without the use of costly patterning masks. DOD is the technology of choice for the deposition of thin organic films due to its smaller drop size and higher placement accuracy [17]. As the name implies, drops are supplied on request. The basic principle relies on a volume reduction in the ink reservoir adjacent to the nozzle. This sudden reduction results in a pressure wave causing the droplet to eject the nozzle. The droplet falls toward the substrate under the influence of gravity and atmospheric resistance. Due to a mismatch between ink and ink-jet waveform settings, an ink-jetted droplet can be followed by a tail, which turns in to many droplets and diffuses uncontrollably into smaller droplets causing defects in the film. The length of the tail can be minimized by adjusting the driving waveform, the viscosity, the surface tension and concentration of the solution. By changing the dot spacing, the film thickness can be controlled.

Finally, spray coating is a large-surface high-throughput technique used in a variety of sectors, e.g.: medical, automotive, electronics, food processing. The deposition of thin polymer films has been demonstrated by a commercially available hand held airbrush [18]–[22]. Although, the use of airbrushes is a cost-effective, high-throughput method, ultrasonic spray nozzles offer more precise control of the spray deposition [23]. It is a contactless deposition technique capable of creating sub-millimetre patterns and of coating non-conformal 3D substrates.

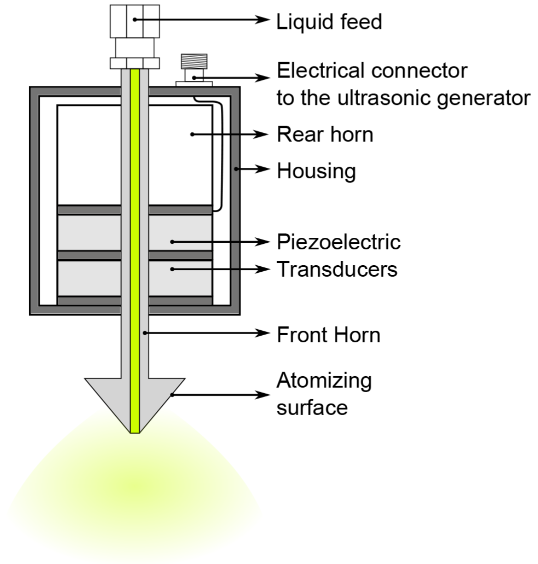

Figure 5.2: Illustration of an ultrasonic nozzle.

An ultrasonic nozzle, as depicted in Figure 5.2, employs standing waves to atomize the solution. Ultrasonic nozzles employ standing waves to atomize the liquid. These standing waves are a result of the mechanical vibrations produced by the (ceramic) piezoelectric transducers inside the ultrasonic nozzle. The ultrasonic generator which is connected to the ultrasonic nozzle supplies an electrical signal, with amplitude A_e and frequency f_e, to the transducers. This results in a mechanical vibration with an amplitude $A_m \propto A_e$ and a frequency $f_m = f_e$. The frequencies typically used for ultrasonic nozzle are situated in the Low Frequency band (LF) and range from 20kHz up to 150 kHz. The produced standing waves along the length of the nozzle form an anti-node at the atomizing surface, here the amplitude is maximum. Nozzle dimensions are governed by the operating frequency (i.e.: resonance frequency), in multiples of 1/2 the wavelength. In general higher frequency nozzles produce smaller droplets. Through the length of the nozzle runs the liquid feed orifice. As the liquid emerges onto the atomizing surface, the kinetic energy is dissipated causing atomization of the liquid. The atomization process relies on liquid being introduced onto the atomizing surface and the correct vibrational amplitude of the atomizing surface. When the vibrational amplitude is below the critical amplitude the liquid will not have sufficient energy to atomize. If the vibrational amplitude is too high the liquid is literally ripped apart, and large “chunks” of fluid are ejected. The rate of atomization only relies on the rate at which the liquid is delivered. The formed low velocity spray is hereafter directed toward the substrate by a nitrogen carrier gas (nitrogen shroud). The micrometre droplet size is governed by the vibrational frequency and solution properties e.g.: surface tension and density. Hereby a high uniform droplet size spray is obtained. In recent years, organic solar cells (OSCs) were successfully (ultrasonically) spray coated [19], [23]–[26]. Furthermore, transparent electrode materials with high conductive PEDOT:PSS [27], zinc oxide (ZnO) [28] and nanoparticle-based silver top contacts [7] were ultrasonically spray coated to produce efficient OSCs. In this chapter we explore ultrasonic spray coating as deposition technique for the emissive layer in OLEDs.

5.3 Effect of ultrasonic atomisation

Ultrasonic mechanic vibration applied to the polymer-solvent mixtures has been known to potentially cause polymer backbone scission (cleavage), reducing the average polymer chain length [29]. Scission of the conjugated polymer backbone can cause an increase in the ionization potential of the polymer and increase the HOMO-LUMO energy gap, directly affecting the photoluminescence efficacy and emission spectrum of the OLED [30].

To allow proper comparison of the ultrasonic spray coating technique and the spin coating technique, the effect of ultrasonic atomization in ambient conditions were analysed first. The pristine polymer solution, stored in a inert atmosphere glove box, was ultrasonically atomized at the nozzle of the spray coater system in ambient conditions, collected and brought back into the inert atmosphere glove box system (‘labelled ultrasonically atomized solution’), as illustrated in Figure 5.3.

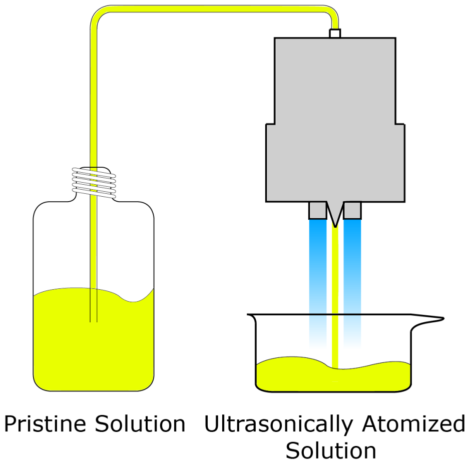

Figure 5.3: Graphical illustration of pristine and ultrasonically atomized solution.

To explore the effects of ultrasonication of the Super Yellow polymer in solution, GPC was performed to determine the (average) molar mass distribution for a pristine and an ultrasonically atomized solution. No evidence of polymer scission of the conjugated backbone was however found (Figure 5.4).

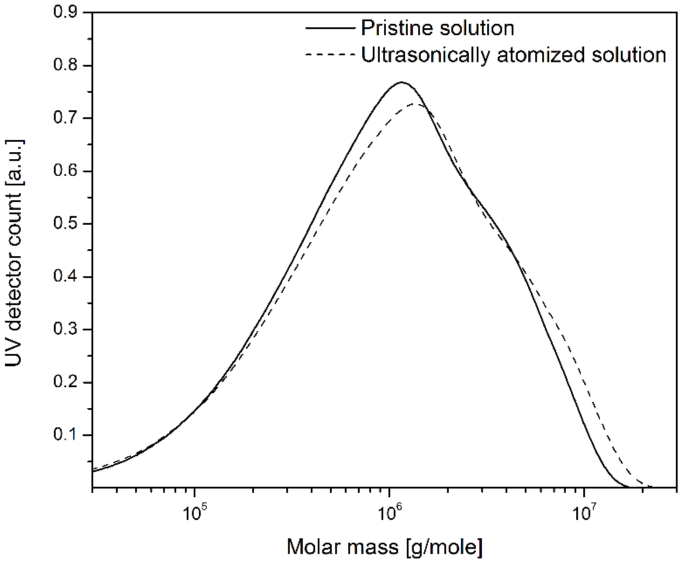

Figure 5.4: Gel permeation chromatography (GPC) results for pristine and ultrasonically atomized Super Yellow samples.

Extensive cleavage of the conjugated polymer backbone would also become apparent in the absorption spectrum. A significant reduction in the length of the Super Yellow polymer chains would cause a blue shift in the thin film absorption spectrum [30]. However, there is no evidence of such a shift after ultrasonic atomization of the Super Yellow solution, as shown in Figure 5.5.

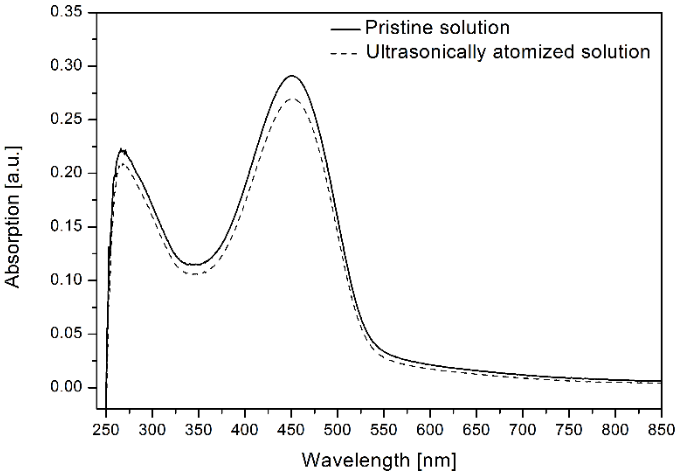

Figure 5.5: UV-Vis absorption spectra of pristine and ultrasonically atomized Super Yellow solutions spin coated on glass substrates.

The side-chain integrity of the ultrasonically atomized Super Yellow polymer was further investigated by FTIR and ^{1}H NMR spectroscopy. Comparison of the FTIR spectra obtained from the ultrasonically atomized and pristine Super Yellow polymer shows near-identical vibrational bands (Figure 5.6), indicating that the chemical structure of the Super Yellow polymer after ultrasonic atomization remains unaffected (i.e. no new functional groups are created).

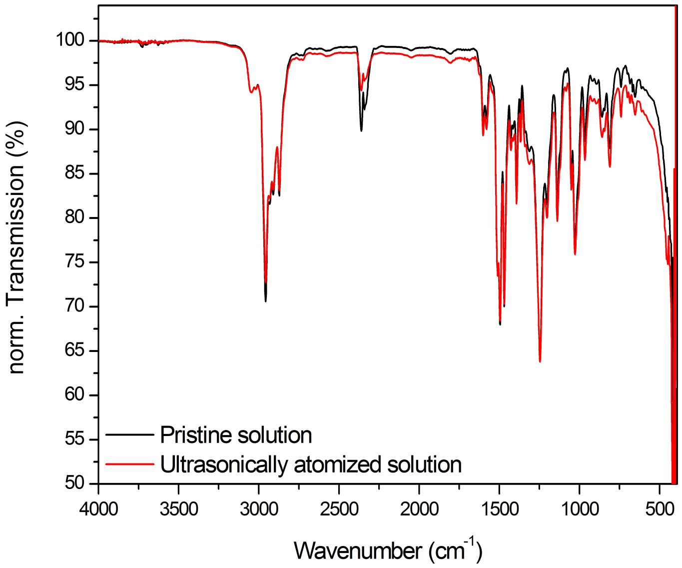

Figure 5.6: Normalized FTIR transmission spectra of films obtained from pristine and ultrasonically atomized Super Yellow solutions.

Extensive side-chain cleavage would be visible by a decrease in the C-H stretching vibration intensity. The ^{1}H NMR spectra, recorded for the pristine and ultrasonically atomized solutions, confirm these results (see Figure 5.7). The small spikes, observable in the ^{1}H NMR spectrum of the pristine solution (blue), can be attributed to remnants of solvents after drying the solution prior to the measurement. These solvent spikes are typically narrow, have a low intensity and can be found at their characteristic chemical shift value e.g.: 3.5 ppm corresponds to diethyl ether, 1.85 ppm corresponds to tetrahydrofuran and 1.5 ppm corresponds to water.

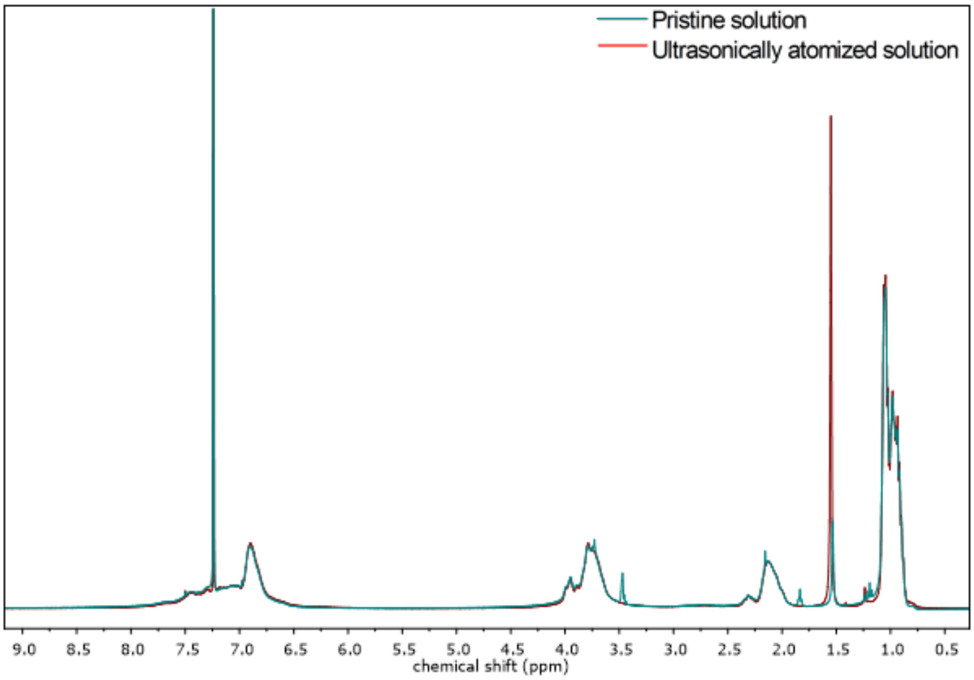

Figure 5.7: ^1H NMR spectra recorded for solutions (in CDCl3) of the pristine (blue) and ultrasonically atomized (red) Super Yellow polymer. The overlap of both spectra indicates that there is no change in the chemical structure of the polymer after ultrasonic atomization in ambient conditions.

A series of Super Yellow OLEDs were prepared via spin coating using either the pristine solution or the ultrasonically atomized Super Yellow solution. The active layers of the devices prepared from both solutions were spin coated inside the glove box. Figure 5.8 shows the luminous power efficacies of both sets of devices as a function of the applied bias voltages. The overall low efficacies can be related to the active layer thickness (~ 25 nm), resulting from the low concentration used to prepare both solutions, 2.5 mg/mL, which was a precondition for a good ultrasonic atomization. Over the whole bias voltage range, both sets of devices showed comparable luminous power efficacies. These results suggest that ultrasonic atomization in ambient conditions has little (or no) influence on the device performance.

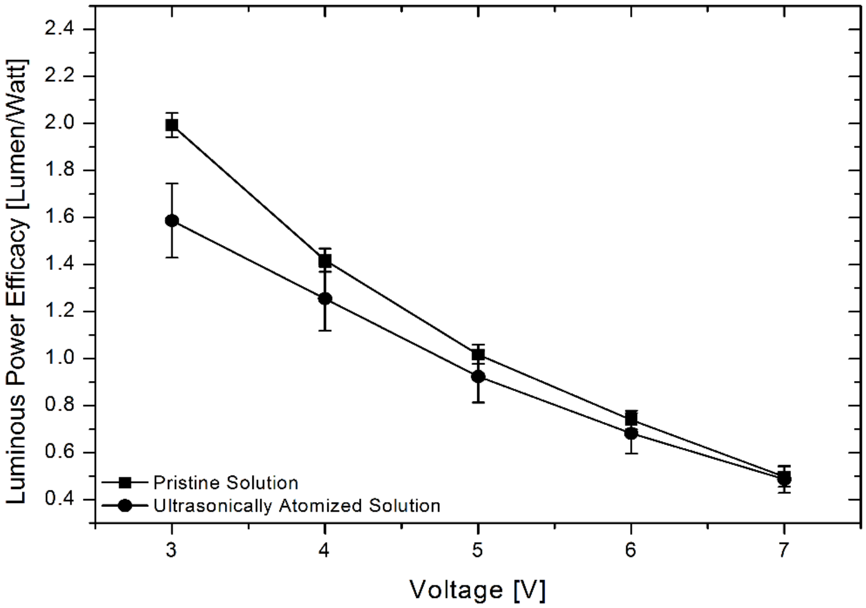

Figure 5.8: Experimental luminous power efficacies of the spin coated OLEDs from pristine and ultrasonically atomized Super Yellow solutions.

5.4 Ultrasonically sprayed thin film deposition

As shown in the previous section, the ultrasonic atomisation has no effect on the molecular structure of the dissolved conjugated polymers. This is the most crucial precondition of this deposition technique to be a viable alternative. In this section, the film forming properties of ultrasonic spray coating is treated.

The first step in the investigation of the film forming techniques is to select a solvent or multiple solvent mixture and polymer concentration, which allow good ultrasonic atomisation. Furthermore, the selected solvent(s) – polymer mixture should also be compatible with the substrate or the previously deposited layer.

Table 5.1 shows multiple ultrasonic spray coating experiments of the deposition of Super Yellow on top of a previously spin coated and annealed PEDOT:PSS layer. Beyond the film forming properties, the drying behaviour of the deposited films is also of key importance, as they require a post-deposition annealing step in an inert atmosphere. Therefore, solvent evaporation should be avoided during and after deposition.

Table 5.1: Overview of multiple ultrasonic spray coating experiments of the active layer, Super Yellow (SY) and their film forming properties. Abbreviations: Tetrahydrofuran (THF); 1,2-dichloorbenzene (oDCB); Mesitylene (Mes.); chloorbenzene (CB); toluene (Tol.).

Solvent(s)	**[SY] (mg/ml)**	**film properties**
THF	1	Coffee ring effect
oDCB	1	Terassed Hill effect
oDCB + Mes. 10 v/v%	2.5	smooth film
oDCB + Mes. 20 v/v%	2.5	smooth film
oDCB + Mes. 30 v/v%	2.5	smooth film
oDCB + Mes. 40 v/v%	2.5	smooth film
oDCB	1.5-3	smooth film
CB	2.5	smooth film
CB + Tol.10 v/v%	2.5	smooth film
CB + Tol.20 v/v%	2.5	smooth film
CB + Tol.30 v/v%	2.5	smooth film

After systematic variation of different Super Yellow solvent mixtures, as listed in Table 5.1, it was observed that a Super Yellow solution in 1,2-dichlorobenzene with a concentration of 2.5 mg/mL yielded an excellent combination of both aerosol formation properties and spreading, wetting and drying behaviour of the mixture on the substrate. Uniform substrate coverage was obtained by tuning the ultrasonic spray coater parameters. The nano-scale morphology of spin coated and ultrasonically spray coated Super Yellow films, prepared from the same solution, were investigated by AFM as can be seen in Figure 5.9. The ultrasonically spray coated film has a similar topography and root mean square (rms) surface roughness as the spin coated film, 2.8 nm and 1.2 nm, respectively, determined by a scan length of 10 µm.

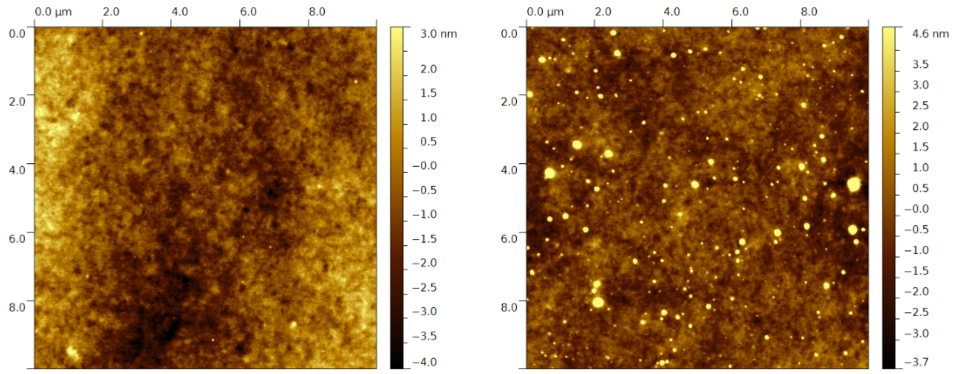

Figure 5.9: AFM topography image (10 µm by 10 µm) of (left) spin coated Super Yellow film (right) ultrasonically spray coated Super Yellow film.

The overall film thickness can vary by the concentration of the solution, the solution flow rate and the nozzle speed. To achieve the optimal Super Yellow layer thickness of 80 nm [2] and find a relation between the final film thickness and solution concentration, the concentration of the solution was varied from 1 mg/ml to 3 mg/ml with increments of 0.5 mg/ml. Figure 5.10 shows the Super Yellow layer thickness as function of the solution concentration. All the Super Yellow films were ultrasonically spray coated from their specific Super Yellow – oDCB concentration with their individual spray coating parameters, e.g.: flow rate, nozzle speed, to yield full substrate coverage and uniform low roughness films.

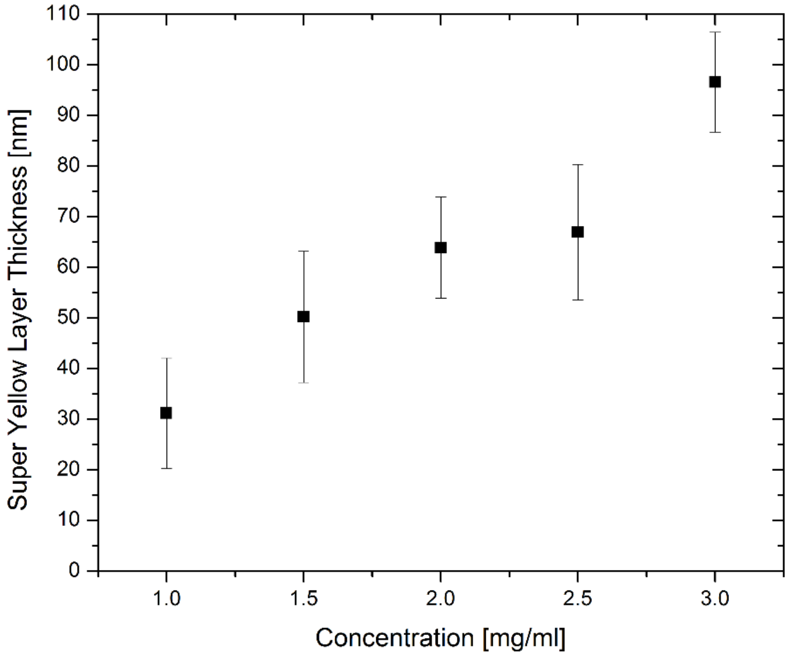

Figure 5.10: Super Yellow layer thickness as function of Super Yellow - pure oDCB solution concentration.

The solution concentration is not the most practical parameter to vary when optimizing the active layer thickness of an OLED. For each variation of the solution concentration a new solution batch has to be made using relative expensive conjugated polymers and organic solvents. However the ultrasonic spray deposition technique also allows deposition control by varying the solution flow rate and nozzle speed at constant solution concentration. By varying the solution flow rate, the amount of solution that emerges at the atomizing surface of the nozzle is changed per unit of time and thus the spray density is varied. Figure 5.11 shows the resulting Super Yellow film thickness as function of the flow rate at a constant nozzle speed of 15 mm/s, using a 2.5 mg/ml Super Yellow - oDCB solution. At flow rates lower than 0.4 ml/min non-uniform and partially covered films were observed. At flow rates higher than 2.0 ml/min atomization at the ultrasonic nozzle was hindered.

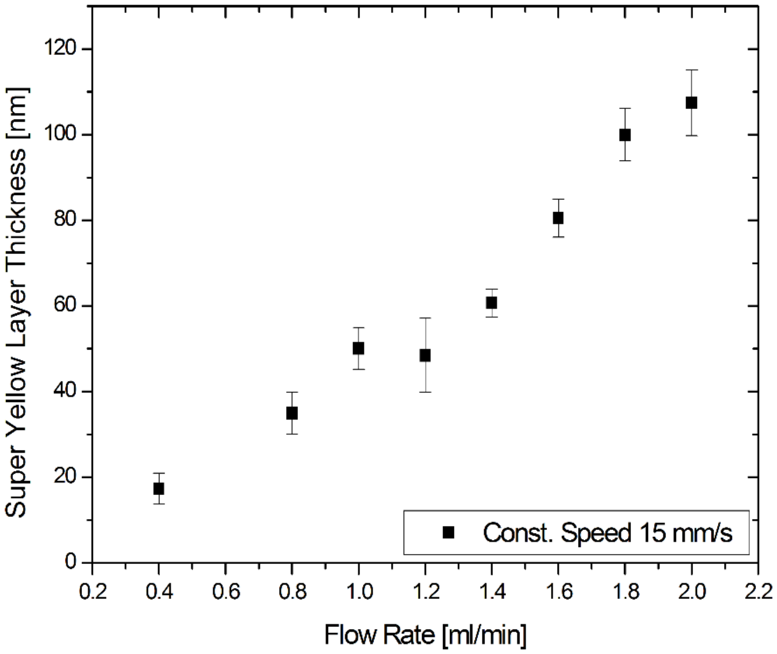

Figure 5.11: Super Yellow layer thickness as function of solution flow rate at constant nozzle speed and constant concentration.

By varying the nozzle speed at a constant flow rate the final film thickness can also be tuned as depicted in Figure 5.12. The solution, 2.5 mg/ml Super Yellow – oDCB, was supplied to the ultrasonic nozzle at a constant flow rate of 1.5 ml/min.

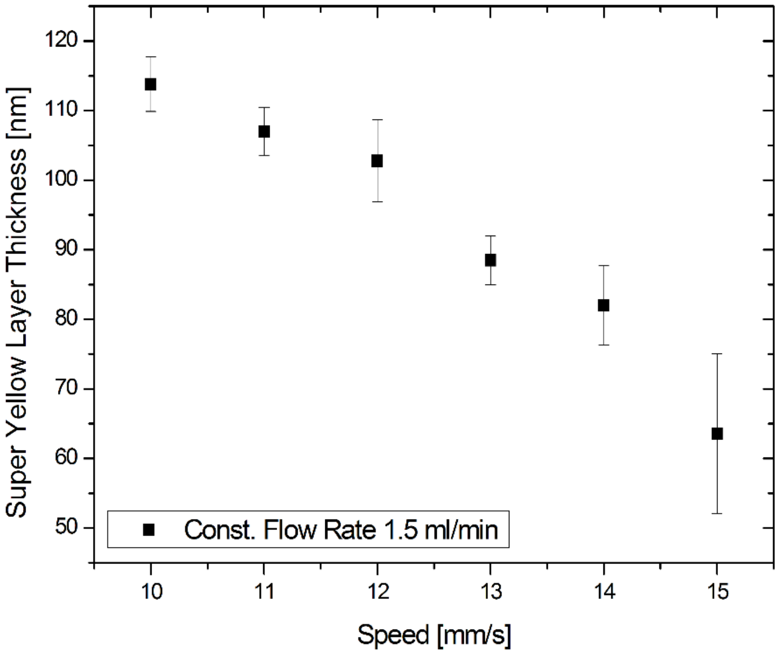

Figure 5.12: Super Yellow layer thickness as function of nozzle speed at constant solution flow rate and constant concentration.

These results show that for a single solution concentration a wide range of film thicknesses can be deposited. The thickness of the emissive layer is of crucial importance for the charge transport in the OLED [31]. The ability of this deposition technique makes it an ideal candidate for solution processing of OLEDs on an industrial scale as well as on laboratory scale.

5.5 Ultrasonically sprayed OLEDs

Complete devices, as illustrated in Figure 5.13, with ultrasonically spray coated Super Yellow layers of ~80 nm, were then produced using 2.5 mg/ml of Super Yellow in oDCB. The substrate was cleaned and the remaining layers were deposited via spin coating and thermal evaporation as discussed in section 6 of chapter 2.

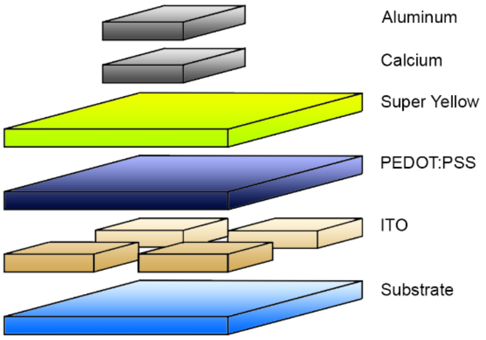

Figure 5.13: OLED device structure.

Figure 5.14 shows the current density-voltage (J-V) and total luminous flux-voltage (Φ-V) characteristics (Figure 5.14a) as well as the luminous power efficacy in function of the applied voltage (Figure 5.14b). When the devices were electrically connected to a voltage source, an intense homogenous yellow light output was observed (Figure 5.14c). The luminous power efficacies of the ultrasonically spray coated device, up to 9.71 Lumen/Watt, approach the luminous power efficacies of 12 Lumen/Watt of the spin coated reference device [32]. An important point to be emphasized is that the active layers of the ultrasonically spray coated devices are deposited in ambient conditions. The thin film morphology has an important effect on the optoelectronic properties of the OLEDs. Two of the main parameters to control the final film morphology are the processing technique and the solvent system used [33]. To investigate the influence of the solvent oDCB, spin coated devices prepared from an optimized Super Yellow-oDCB mixture were compared to spin coated devices prepared from an optimized Super Yellow-chlorobenzene (CB) mixture. Both sets of spin coated devices, from oDCB and CB, reached efficacies of 12 Lumen/Watt. These results suggest that the solvent (oDCB) is not responsible for the relative lower device efficacies of the ultrasonically spray coated OLEDs. The origin of the difference in device efficacies needs to be further investigated.

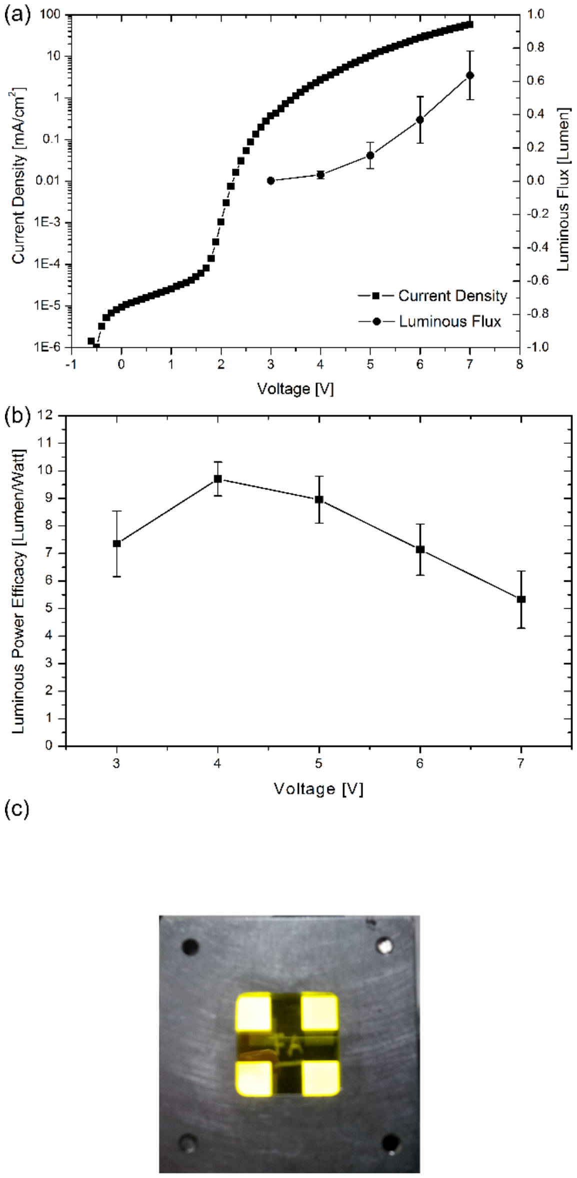

Figure 5.14: (a) Experimental current density-voltage characteristics and total luminous flux of the spray coated OLED. (b) Experimental luminous power efficacy of the spray coated OLED. (c) Digital photograph of the operated device with ultrasonically spray coated active layer (each device has a physical dimension of 5 mm by 5 mm).

5.6 Conclusion

We have investigated ultrasonically spray coated Super Yellow thin films for utilization in polymer LEDs. We have investigated the effect of the ultrasonic atomization in ambient conditions on the optoelectronic properties of the Super Yellow polymer. To exclude (extensive) polymer backbone scission as a result of the ultrasonic vibration of the nozzle, the average molar mass (distribution) and thin film UV-VIS absorption spectrum were investigated, showing minimal (if any) polymer backbone cleavage. A major side chain cleavage is excluded by comparing the IR and ^{1}H NMR spectra of the pristine and ultrasonically atomised solutions. Systematic variation of the polymer-solvent mixture and spray coater system settings yielded uniform, fully covered and low roughness thin films. Furthermore it is shown that the final deposited layer thickness can easily be tuned by varying the flow rate and nozzle speed making it a versatile and ideal candidate for the roll-to-roll production of polymer based light emitting diodes. Devices based on these films were characterized quantifying their operating parameters, i.e. current density, bias voltage, luminance flux and luminous power efficacy. We achieved a promising luminous power efficacy of 9.71 Lumen/Watt for single layer (Super Yellow) ultrasonically spray coated OLEDs. It is reasoned that the resulting slightly lower device efficacy is not related to reasons such as polymer scission, ultrasonic atomization in ambient conditions or the particular solvent (oDCB) used. However, a detailed investigation of the nano-scale active layer morphology is needed to understand the efficacy difference between spin coated and ultrasonically spray coated devices. Based on the presented results, it is clear that ultrasonic spray coating is a promising technique towards the upscaling and roll-to-roll processing of OLEDs.

5.7 References

[1] F. C. Krebs, “Fabrication and processing of polymer solar cells: A review of printing and coating techniques,” *Sol. Energy Mater. Sol. Cells*, vol. 93, no. 4, pp. 394–412, Apr. 2009.

[2] P. de Bruyn, D. J. D. Moet, and P. W. M. Blom, “All-solution processed polymer light-emitting diodes with air stable metal-oxide electrodes,” *Org. Electron.*, vol. 13, no. 6, pp. 1023–1030, Jun. 2012.

[3] J. Lee, S. Lee, G. Li, M. a. Petruska, D. C. Paine, and S. Sun, “A facile solution-phase approach to transparent and conducting ITO nanocrystal assemblies,” *J. Am. Chem. Soc.*, vol. 134, no. 32, pp. 13410–13414, 2012.

[4] Z. Chen, W. Li, R. Li, Y. Zhang, G. Xu, and H. Cheng, “Fabrication of highly transparent and conductive indium-tin oxide thin films with a high figure of merit via solution processing.,” *Langmuir*, vol. 29, no. 45, pp. 13836–42, 2013.

[5] R. R. Søndergaard, M. Hösel, and F. C. Krebs, “Roll-to-Roll fabrication of large area functional organic materials,” *J. Polym. Sci. Part B Polym. Phys.*, vol. 51, no. 1, pp. 16–34, Jan. 2013.

[6] L. Hou, L. Duan, J. Qiao, D. Zhang, G. Dong, L. Wang, and Y. Qiu, “Efficient solution-processed small-molecule single emitting layer electrophosphorescent white light-emitting diodes,” *Org. Electron.*, vol. 11, no. 8, pp. 1344–1350, Aug. 2010.

[7] C. Girotto, B. P. Rand, S. Steudel, J. Genoe, and P. Heremans, “Nanoparticle-based, spray-coated silver top contacts for efficient polymer solar cells,” *Org. Electron.*, vol. 10, no. 4, pp. 735–740, Jul. 2009.

[8] K. Norrman, a. Ghanbari-Siahkali, and N. B. Larsen, “6 Studies of spin-coated polymer films,” *Annu. Reports Sect. “C” (Physical Chem.*, vol. 101, p. 174, 2005.

[9] N. Sahu, B. Parija, and S. Panigrahi, “Fundamental understanding and modeling of spin coating process: A review,” *Indian J. Phys.*, vol. 83, no. 4, pp. 493–502, Aug. 2009.

[10] P. Yimsiri and M. R. Mackley, “Spin and dip coating of light-emitting polymer solutions: Matching experiment with modelling,” *Chem. Eng. Sci.*, vol. 61, no. 11, pp. 3496–3505, Jun. 2006.

[11] S.-R. Tseng, H.-F. Meng, K.-C. Lee, and S.-F. Horng, "Multilayer polymer light-emitting diodes by blade coating method," *Appl. Phys. Lett.*, vol. 93, no. 15, p. 153308, 2008.

[12] J. Birnstock, J. Blässing, a. Hunze, M. Scheffel, M. Stößel, K. Heuser, G. Wittmann, J. Wörle, and a. Winnacker, "Screen-printed passive matrix displays based on light-emitting polymers," *Appl. Phys. Lett.*, vol. 78, no. 24, p. 3905, 2001.

[13] J. Brünahl and A. M. Grishin, "Piezoelectric shear mode drop-on-demand inkjet actuator," *Sensors Actuators A Phys.*, vol. 101, no. 3, pp. 371–382, Oct. 2002.

[14] F. Villani, P. Vacca, R. Miscioscia, G. Nenna, G. Burrasca, T. Fasolino, C. Minarini, and D. Della Sala, "OLED with Hole-Transporting Layer Fabricated by Ink-Jet Printing," *Macromol. Symp.*, vol. 286, no. 1, pp. 101–106, Nov. 2009.

[15] M. Singh, H. M. Haverinen, P. Dhagat, and G. E. Jabbour, "Inkjet printing-process and its applications.," *Adv. Mater.*, vol. 22, no. 6, pp. 673–85, Mar. 2010.

[16] C. N. Hoth, S. a. Choulis, P. Schilinsky, and C. J. Brabec, "High Photovoltaic Performance of Inkjet Printed Polymer:Fullerene Blends," *Adv. Mater.*, vol. 19, no. 22, pp. 3973–3978, Nov. 2007.

[17] B.-J. de Gans, P. C. Duineveld, and U. S. Schubert, "Inkjet Printing of Polymers: State of the Art and Future Developments," *Adv. Mater.*, vol. 16, no. 3, pp. 203–213, Feb. 2004.

[18] D. Vak, S.-S. Kim, J. Jo, S.-H. Oh, S.-I. Na, J. Kim, and D.-Y. Kim, "Fabrication of organic bulk heterojunction solar cells by a spray deposition method for low-cost power generation," *Appl. Phys. Lett.*, vol. 91, no. 8, p. 081102, 2007.

[19] S.-I. Na, B.-K. Yu, S.-S. Kim, D. Vak, T.-S. Kim, J.-S. Yeo, and D.-Y. Kim, "Fully spray-coated ITO-free organic solar cells for low-cost power generation," *Sol. Energy Mater. Sol. Cells*, vol. 94, no. 8, pp. 1333–1337, Aug. 2010.

[20] C. Girotto, B. P. Rand, J. Genoe, and P. Heremans, "Exploring spray coating as a deposition technique for the fabrication of solution-processed solar cells," *Sol. Energy Mater. Sol. Cells*, vol. 93, no. 4, pp. 454–458, Apr. 2009.

[21] M. P. Aleksandrova, "Improvement of the electrical characteristics of polymer electroluminescent structures by using spray-coating

technology," *J. Coatings Technol. Res.*, vol. 9, no. 2, pp. 157–161, Oct. 2009.

[22] E. Treossi, A. Liscio, X. Feng, V. Palermo, K. Müllen, and P. Samorì, "Large-area bi-component processing of organic semiconductors by spray deposition and spin coating with orthogonal solvents," *Appl. Phys. A*, vol. 95, no. 1, pp. 15–20, Feb. 2009.

[23] K. X. Steirer, M. O. Reese, B. L. Rupert, N. Kopidakis, D. C. Olson, R. T. Collins, and D. S. Ginley, "Ultrasonic spray deposition for production of organic solar cells," *Sol. Energy Mater. Sol. Cells*, vol. 93, no. 4, pp. 447–453, Apr. 2009.

[24] K. X. Steirer, J. J. Berry, M. O. Reese, M. F. A. M. Van Hest, A. Miedaner, M. W. Liberatore, R. T. Collins, and D. S. Ginley, "Ultrasonically sprayed and inkjet printed thin film electrodes for organic solar cells," *Thin Solid Films*, vol. 517, no. 8, pp. 2781–2786, 2009.

[25] K. X. Steirer, M. O. Reese, B. L. Rupert, N. Kopidakis, D. C. Olson, D. S. Ginley, and R. T. Collins, "Advancing spray deposition for low-cost solar cell production," *SPIE Newsroom*, pp. 1–3, 2009.

[26] Y.-C. Huang, F.-H. Hsu, H.-C. Cha, C.-M. Chuang, C.-S. Tsao, and C.-Y. Chen, "High-performance ITO-free spray-processed polymer solar cells with incorporating ink-jet printed grid," *Org. Electron.*, vol. 14, no. 11, pp. 2809–2817, Nov. 2013.

[27] J. G. Tait, B. J. Worfolk, S. a. Maloney, T. C. Hauger, A. L. Elias, J. M. Buriak, and K. D. Harris, "Spray coated high-conductivity PEDOT:PSS transparent electrodes for stretchable and mechanically-robust organic solar cells," *Sol. Energy Mater. Sol. Cells*, vol. 110, pp. 98–106, Mar. 2013.

[28] Y. L. Ee, H. K. Im, and Y. R. Oh, "Deposition of ZnO Thin Films by the Ultrasonic Spray Pyrolysis Technique," *Jpn. J. Appl. Phys.*, vol. 40, no. 4, pp. 2423–2428, 2001.

[29] M. M. Caruso, D. a Davis, Q. Shen, S. a Odom, N. R. Sottos, S. R. White, and J. S. Moore, "Mechanically-induced chemical changes in polymeric materials.," *Chem. Rev.*, vol. 109, no. 11, pp. 5755–98, Nov. 2009.

[30] E. Peeters, A. M. Ramos, and S. C. J. Meskers, "Singlet and triplet excitations of chiral dialkoxy-p -phenylene vinylene oligomers," *J. Chem. Phys.*, vol. 112, no. 21, pp. 9445–9454, 2000.

[31] P. W. M. Blom, C. Tanase, D. M. de Leeuw, and R. Coehoorn, "Thickness scaling of the space-charge-limited current in poly(p-phenylene vinylene)," *Appl. Phys. Lett.*, vol. 86, no. 9, p. 092105, 2005.

[32] B. H. Spreitzer, H. Becker, E. Kluge, W. Kreuder, H. Schenk, and R. Demandt, “Soluble Phenyl-Substituted PPVs New Materials for Highly Efficient Polymer LEDs **,” *Adv. Mater.*, vol. 10, no. 16, pp. 1340–1343, 1998.

[33] Y. Shi, J. Liu, and Y. Yang, “Device performance and polymer morphology in polymer light emitting diodes: The control of thin film morphology and device quantum efficiency,” *J. Appl. Phys.*, vol. 87, no. 9, p. 4254, 2000.

Chapter 6 Conclusions and outlook

The most widely adopted fabrication steps for OLEDs reported in literature include physical vapour deposition of the transparent and metal electrodes, spin coating of the organic layers and thermal annealing by a conventional hotplate. These processes are very effective for research purposes in a laboratory environment. On the other hand, these processing steps do not scale conveniently to high throughput and large scale production processes. The ideal production process [1] for OLEDs, as described in section 1.6, should involve an indium free electrode. Additionally, the deposition of the OLED structure should comprise out of as few deposition techniques as possible and the deposition technique should be easy scalable and allow patterning. Within this thesis, as summarised in Figure 6.1, in line with the ideal processes, an indium free BNCD:Au-grid electrode has been explored as anode for OLEDs. Moreover, a alternative and faster post-deposition treatment, employing microwaves, has been demonstrated. Finally, ultrasonic spray coating has been investigated on its viability as deposition technique for the emissive layer in OLEDs.

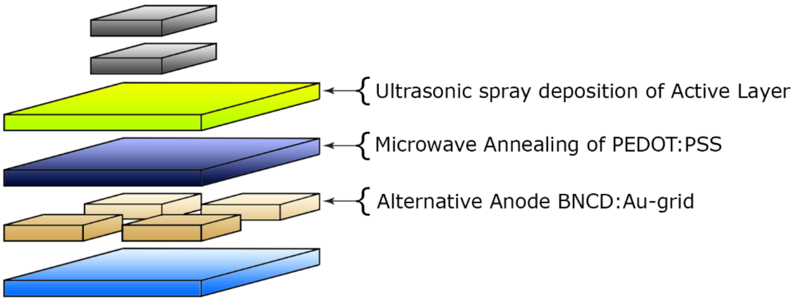

Figure 6.1: Graphical illustration of the work presented in this thesis.

The BNCD:Au-grid anode with a transparency of ~70 % and a sheet resistance of 20 Ω/square shows a great promise as a transparent electrode for OLEDs and other organic electronic devices owing its high thermal and chemical stability. Compared to ITO anode reference devices an enhanced luminous flux is observed and is currently attributed to an overall better hole-injection. Further improvements concerning its optical transparency and sheet resistance can be accomplished by adapting the rectangular grid layout to a hexagonal, spiral or leaf-like grid [2]. To further investigate the enhanced luminance flux, additional optical characterizations of the BNCD:Au-grid and ITO reference OLEDs are needed. With these additional characterizations the emission profiles i.e.: spectrally integrated emitted power per unit solid angle and different optical modes, e.g.: unbound air modes, substrate trapped modes, waveguided modes and surface plasmon polariton modes can be determined and could potentially reveal the origin of the enhanced luminous flux. A further electrical investigation is necessary as the enhanced luminous flux could be a result of a better hole injection by the BNCD:Au-grid anode. A work function investigation by ultraviolet photoemission spectroscopy (UPS) can provide a better insight into the hole injection barrier. The enhanced hole-injection could potentially improve the recombination efficiency as a result of multiple effects such as a better charge balance and, extension of the recombination zone.

Microwave annealing as post-deposition treatment of PEDOT:PSS has been explored. A thermal post-deposition treatment is an essential step in the fabrication process of solution processed OLEDs, to remove solvents and additives from the as-deposited wet thin-films. In a laboratory environment this is done by means of a conventional hotplate and is a time consuming process [3], [4]. From in-situ current measurement it is shown that the post deposition thermal treatment employing microwaves is 2.5 times faster than the conventional hotplate system. Furthermore, through carefully controlling the emitted microwave power and maintaining a multimode uniform electromagnetic field, the electronic properties of these thin film organic semiconductors are retained. A further investigation should focus other post-deposition techniques such as light-induced flash sintering and their influence on these thin film organic semiconductors. Hereby, classical thermal processes, e.g.: conduction and radiation, can be replaced by these new, more scalable and faster techniques.

Ultrasonic spray coating is a relative new solution processing technique in the field of organic electronics [5]. It has many advantages over conventional solution processing techniques. It is a non-contact roll-to-roll compatible technique capable of sub-millimeter patterning and large uniform thin film deposition. In this work, ultrasonic spray coating is investigated as deposition technique for the emissive layer in OLEDs. Ultrasonic nozzles utilize ultrasonic standing waves to produce a uniform pico-liter droplet size spray. It is shown that these mechanical, ultrasonic oscillations of the ultrasonic nozzle tip do not modify the molecular structure of the polymers in solution. The nano-scale morphology of ultrasonically spray coated thin films have a similar topography compared to spin coated films. Moreover, the film forming properties of this deposition technique is characterized. Systematic variation of solution concentration and spray coating parameters e.g.: flow rate and nozzle speed shows the wide applicability of ultrasonic spray coating as thin film deposition technique. Additionally, OLEDs with ultrasonically spray coated emissive layers are fabricated in ambient conditions. A small reduction in the luminous power efficacy of the OLEDs with ultrasonically spray coated emissive layers, compared to spin coated reference devices, is observed. To rule out degradation of the emissive layer from exposure to ambient conditions the ultrasonic spray deposition should be repeated in inert atmosphere. The molecular orientation and intermolecular interaction in the organic layers have a significant effect on the electrical and optical properties of OLEDs [6]. This structural disorder in the organic thin film semiconducting layer is governed by the molecular structure of the organic material, the deposition technique and post deposition treatment. Further research is needed to explore the possible lower structural disorder in ultrasonically spray coated organic layers as compared to spin coated layers.

6.1 References

[1] F. C. Krebs, “Fabrication and processing of polymer solar cells: A review of printing and coating techniques,” *Sol. Energy Mater. Sol. Cells*, vol. 93, no. 4, pp. 394–412, Apr. 2009.

[2] F. L. M. Sam, C. a. Mills, L. J. Rozanski, and S. R. P. Silva, “Thin film hexagonal gold grids as transparent conducting electrodes in organic light emitting diodes,” *Laser Photonics Rev.*, vol. 8, no. 1, pp. 172–179, 2014.

[3] J. Huang, P. F. Miller, J. C. de Mello, a. J. de Mello, and D. D. C. Bradley, “Influence of thermal treatment on the conductivity and morphology of PEDOT/PSS films,” *Synth. Met.*, vol. 139, no. 3, pp. 569–572, Oct. 2003.

[4] T. P. Nguyen, P. Le Rendu, P. D. Long, and S. a. De Vos, “Chemical and thermal treatment of PEDOT:PSS thin films for use in organic light emitting diodes,” *Surf. Coatings Technol.*, vol. 180–181, pp. 646–649, Mar. 2004.

[5] R. G. Gordon, X. Liu, D. Pang, and J. Barton, “Transparent Conductors and Barrier Layers for Thin Film Solar Cells,” *NREL Final Tech. Rep.*, 2001.

[6] D. Yokoyama, “Molecular orientation in small-molecule organic light-emitting diodes,” *J. Mater. Chem.*, vol. 21, no. 48, p. 19187, 2011.